Fakultät für
Mathematik und Naturwissenschaften
Astroteilchenphysik

**BERGISCHE
UNIVERSITÄT
WUPPERTAL**

Search for mildly relativistic Magnetic Monopoles with IceCube

DISSERTATION
zur Erlangung des Doktorgrades
doctor rerum naturalium
(Dr. rer. nat.)

Der Fachgruppe Physik vorgelegt von

Anna Maria Pollmann

geb. Obertacke

im November 2015

Die Dissertation kann wie folgt zitiert werden:

urn:nbn:de:hbz:468-20160824-113132-8

[http://nbn-resolving.de/urn/resolver.pl?urn=urn%3Anbn%3Ade%3Ahbz%3A468-20160824-113132-8]

Abstract

The existence of magnetic monopoles is motivated by various theories which extend the Standard Model of particles. Monopoles could have been created in an early epoch of the Universe as stable particles carrying magnetic charge. Cosmic magnetic fields would accelerate them to relativistic velocities. Due to these high kinetic energies monopoles can pass through massive objects, such as the Earth, and remain relativistic despite their huge energy loss in matter.

Equivalently to electrically charged particles, magnetic monopoles produce direct Cherenkov light while traversing through ice with a velocity of $> 0.76\,c$. Below this threshold monopoles are energetic enough to ionize the surrounding matter by knocking electrons off their atoms. If these δ-electrons are accelerated to velocities above $0.76\,c$, they produce Cherenkov light. This indirect Cherenkov light induced by a monopole occurs down to a velocity of about $0.45\,c$.

The IceCube neutrino telescope is a Cherenkov detector which is suitable for monopole searches. Previous searches in IceCube data focused on highly relativistic ($> 0.76\,c$) and non-relativistic ($< 0.1\,c$) monopole signatures.

The analysis presented in this work is distinct from previous analyses in IceCube as it extends the search range to intermediate velocities by using indirect Cherenkov light as a detection signature. This work describes the search for mildly relativistic monopoles using one year of IceCube data taken in the 2011/2012 season. No monopole candidate was detected and the flux is constrained down to a level of $1.55 \cdot 10^{-18}\,\mathrm{cm}^{-2}\mathrm{s}^{-1}\mathrm{sr}^{-1}$. This is an improvement of almost two orders of magnitude over previous limits.

Zusammenfassung

Magnetische Monopole sind definiert als als magnetische Punktquelle die nur *eine* magnetische Ladung umfasst. Im klassischen Sinne können magnetische Monopole als Teilchen bezeichnet werden. In moderneren Theorien werden sie als topologische Defekte des Vakuums vorhergesagt, in dessen Inneren die Vereinheitlichung von elektromagnetischer, schwacher und starker Kraft bewahrt wird, die kurz nach dem Urknall im Universum geherrscht haben könnte. Die Theorien stützen sich auf relativ fundamentale und weithin akzeptierte Annahmen. Magnetische Monopole sind einer der vielversprechendsten Vorhersagen von unbekannter Physik außerhalb des Standardmodells der Teilchenphysik, obwohl es bisher keinen bestätigten experimentellen Nachweis der Existenz von magnetischen Monopolen gibt.

Magnetische Monopole können im Universum durch Magnetfelder auf hohe Geschwindigkeiten beschleunigt werden. Wenn sie durch Materie fliegen, bewirken sie bei entsprechend hohen Geschwindigkeiten direkt oder indirekt die Erzeugung von Cherenkov Licht. Dies ist polarisiertes Licht mit kontinuierlichem Spektrum, dass einen dominierendem blauen/ultraviolettem Anteil hat.

Das Neutrinoteleskop IceCube ist ein Cherenkov-Licht-Detektor, der aufgrund seines großen Volumens besonders für die Suche nach sehr seltenen Teilchen geeignet ist und deshalb in dieser Arbeit für die Suche nach magnetischen Monopolen verwendet wird. IceCube wurde bis Dezember 2010 in der Nähe des geographischen Südpols in der Antarktis gebaut. Diese Arbeit verwendet die Daten, die vom Detektor in der Saison April 2011 bis April 2012 aufgezeichnet wurden.

In dieser Arbeit werden magnetische Monopole gesucht, die bei Erreichen des IceCube Detektors eine Geschwindigkeit unterhalb der Cherenkov-Schwelle haben, also weniger als 76 % der Lichtgeschwindigkeit im Vakuum. Die theoretischen Grundlagen der entsprechenden Detektionsmethode, basierend auf indirektem Cherenkov-Licht, werden in dieser Arbeit ausführlich hergeleitet und entsprechen nicht bisherigen Interpretationen anderer Experimentatoren.

Die technische Umsetzung der Analyse umfasst unter anderem die Implementierung der theoretischen Überlegungen in eine Simulation der hypothetischen Signale von magnetischen Monopolen im IceCube Detektor. Diese werden mit den Untergrund-Ereignissen erzeugt von Teilchen des Standardmodells verglichen, vor allem Myonen und atmosphärisch erzeugten Myon-Neutrinos. Hierzu wird die Palette der Variablen, die standardmäßig in IceCube Analysen rekonstruiert wird, durch weitere zeit- und helligkeitsabhängige Parameter ergänzt. Unter Verwendung dieser Variablen kann die Signatur von Monopolen mit einfachen Algorithmen von sonstigen Signalen separiert werden.

In der IceCube Kollaboration werden derartige Analysen *blind* durchgeführt, also ohne Einsicht in die Daten, da experimentelle Suchen nach besonders seltenen Teilchen durch die Erwartung des Experimentators unbewusst beeinflusst werden könnten und dadurch ihre Aussagekraft verlieren. Jedoch steht, wegen des großen Zeitaufwandes für ihre Erzeugung,

nicht ausreichend Statistik an simulierten Untergrund-Ereignissen zur Verfügung. Um dennoch eine statistisch signifikante Analyse durchführen zu können, wird eine Resampling-Methode verwendet, die nur einmal zuvor verwendet wurde. Ihre Zuverlässigkeit und Aussagekraft wird in dieser Arbeit ausführlich getestet.

Nach dem Festsetzen aller Selektionskriterien für Monopole und Berechnung der statistischen Erwartung bezüglich des Ausgangs des Experiments wurde die Analyse auf die Ice-Cube Daten angewendet. Bei einer Erwartung von maximal 3,6 Untergrund-Ereignissen, berechnet mit der Resampling-Methode, wurden 3 Signale beobachtet. Auch die Visualisierung der entsprechenden Ereignisse bestätigt die untergrundartige Signatur. Die verwendete Resampling-Methode erwies sich aufgrund der korrekten Vorhersage des Untergrundes als erfolgreich. Zudem können obere Grenzen auf den Fluss von magnetischen Monopolen für einen unerwartet großen Parameterbereich gesetzt werden, die vorherige Grenzen um fast zwei Größenordnungen unterbieten.

Contents

CONTENTS

Introduction

In 1931 Paul Dirac derived the first theoretical model of magnetic monopoles which are defined as particles carrying only one magnetic pole. This initiated a series of experimental searches lasting more than 80 years until today. Although a confirmed candidate has never been found, theorists have built steadily improved models of magnetic monopoles so that their existence is one of the most promising prospects of physics beyond the current standard model of particles.

IceCube is a neutrino detector which is well suited for the detection of such *exotic particles*[1]. This aspect will be presented in **Chapter 1** of this work. Subsequently, magnetic monopoles are introduced in **Chapter 2** where a summary of monopole properties, which are important for experimental detection, is given in the context of different theoretical eras.

Previous searches for monopoles in IceCube data focused on the search for magnetic monopoles with either highly relativistic (above $0.76\,c$ where c is the velocity of light in vacuum) or non-relativistic (below $0.1\,c$) velocities inside the detector. The parameter range over intermediate monopole velocities (below $0.76\,c$), denoted as *mildly relativistic* in this work, has not been utilized in these analyses. However it was shown that IceCube is capable of detecting these signatures [Obe12].

The standard detection signature of IceCube is Cherenkov light which is produced by electrically charged particles when their velocity exceeds the Cherenkov threshold at $0.76\,c$ in ice. Analogous mechanisms lead to Cherenkov light production from magnetically charged particles. Additionally, magnetic monopoles knock electrons off their atomic bindings and accelerate them above the Cherenkov threshold. These electrons in turn radiate Cherenkov light. Due to this indirect light production a monopole could be detected by IceCube below the Cherenkov threshold. Few experiments suggested or performed monopole searches using this detection mechanism. Furthermore these experiments contradicted each other in the interpretation of the theoretical works needed to apply this mechanism. Consequently **Chapter 3** comprises a detailed paper study and discusses all aspects required to calculate indirect Cherenkov light from monopoles. For this purpose equations and methods are traced back to their very first description to interpret them correctly.

In doing so, another mechanism was found in literature by which monopoles could produce detectable light. Particles depositing large amounts of energies in ice produce luminescence light. The investigation of luminescence to be used as a detection signature for magnetic monopoles is promising but beyond the scope of this work. Therefore it is presented in the **Appendix** for the interested reader.

Due to the above arguments, further elaborated in the first three chapters, the aim of this work is a search for mildly relativistic magnetic monopoles in IceCube data. For this purpose, a simulation of magnetic monopole signatures in IceCube was developed based on the technical aspects of IceCube and the theoretical considerations from monopole models. This is presented in **Chapter 4** of this work.

---

[1]The term exotic particles refers to predicted but not yet detected particles which are not part of the standard model of particles.

The simulated monopole signatures are compared with background signatures in IceCube which originate from standard model particles. The differences between monopole and background event signatures are distinguished by identifying and developing according variables. This is the preparation for the event selection.

However there was not sufficient background statistics available to build an efficient and significant analysis. A re-sampling method proposed by another IceCube analysis was developed further. It is subsequently used by several other analyses. The method is described in detail in **Chapter 5**. Eventually it was used for the event selection and the estimation of final signal and background rates.

The achieved sensitivity of this analysis exceeds limits from other experiments by almost two orders of magnitude. This large improvement implies a large detection possibility. The result is shown in **Chapter 6**.

This work was composed in a way that longer chapters reflect innovations of the interpretation of theoretical foundation, software and methods, such as chapters 3, 4.2, and 5.2. Summaries of established topics focus on aspects, which are important for this work or place this work into context. For further reading, references to comprehensive sources are given.

As a guidance for the reader there is an **Index** at the end of this work comprising abbreviations, nomenclature, and mathematical symbols which references important occurrences giving the definition and context of an expression.

1 IceCube

The IceCube Neutrino Telescope is a particle detector situated near the South Pole in Antarctica [Ach06]. It consists of two components: the surface array, IceTop, which is designed to record cosmic ray air shower events, and the in-ice array at a depth of over 1.5 km, which is set up to detect neutrino interactions. The technique which achieves these main physics goals can also be used for searches of physics beyond the standard model.

This chapter gives a short overview of IceCube's physics purposes and the technical outline to achieve those. Based on this description the conditions for exotic searches with IceCube are discussed.

1.1 Cosmic rays

Cosmic rays are radiation of particles which originate from outside the Earth's atmosphere, for example the Sun, other galactic or extra-galactic objects, and which are accelerated to high energies (up to 10^{11} GeV). The first hint for their existence was given by the measurements of Victor Franz Hess in 1912 who observed increasing radiation at high altitudes during his balloon flights [Hes12]. At first the expression "cosmic rays" referred only to the radiation of atomic nuclei which is dominated by protons (87 %) and helium nuclei (12 %) [Gai92]. However, today it also covers in a broader sense the cosmic neutrino and electromagnetic radiation, which are called X-rays for intermediate and γ-rays for higher energies. As the experimental field of astroparticle physics developed fast in the last 20 years there are currently many different methods to detect cosmic rays. IceCube focuses on the detection of neutrino interactions with ice and air shower events which can be produced by all kinds of cosmic ray primaries.

1.1.1 Air showers

An air shower is produced when a particle of cosmic rays interacts with a particle of the Earth's atmosphere. Highly energetic daughter particles are produced which are origin of new interactions in return. In this *particle cascade*, the particle multiplicity increases with every interaction. Three different shower components have been identified [Tho15]. Firstly, highly energetic electrons (including positrons) radiate bremsstrahlung photons when de-accelerated in the field of a nucleus. These highly energetic photons in turn produce e^+e^- pairs in the vicinity of a nucleus. The repetition of these steps is referred to as the electromagnetic component of a shower. Secondly, charged hadrons ionize atmospheric particles and interact strongly with atmospheric nuclei. The secondaries of these interactions repeat this process which builds up the hadronic shower component. Since there are many different final states in a hadronic interaction a hadronic shower is more variable than an electromagnetic shower. For example, the decay of neutral pions via $\pi^0 \to \gamma + \gamma$ with a probability of more than 98.8 % induces an electromagnetic sub-shower whereas the decay of charged pions via $\pi^\pm \to \mu^\pm + \nu_\mu/\bar{\nu}_\mu$ with a probability of more than 99.9 % gives a muon and a neutrino [Oli14]. These comparably long living and deeply penetrating muons are the third component of air shower particles.

The hadronic interactions in air showers are not fully modeled in theories and simulations because these high energies cannot be produced in particle accelerators for thorough studies. Therefore, the study of cosmic rays with IceTop and other air shower detectors aims for a better understanding of high energy hadronic physics as well as the measurement of the composition, primary energy, and origin of cosmic rays.

The muon component of air showers can penetrate far into matter and is also detected by deep underground detectors such as the in-ice component of IceCube. The models to describe cosmic ray air showers are introduced in Ch. 4.1.1. The principles of air showers also apply for high energetic particle interactions in other mediums, such as ice.

1.1.2   Neutrinos

Neutrinos are neutral leptons which participate only in weak interactions. Accordingly, the neutrino cross section with matter is very small but increases with energy. For example, the mean free path length of a neutrino of $1\,\mathrm{PeV}$ energy is approximately equal to the Earth's diameter. The neutrino mass is so low that it still has to be measured. There are three neutrino flavors $l = \{e, \mu, \tau\}$ which correspond to the charged leptons's flavors. In matter neutrino interactions with nuclei is dominant which can be divided into two types[2] [Gan98]

- neutral current interaction: a neutrino ν of flavor l couples to a nucleus N via a neutral Z^0-boson

$$\nu_l + N \xrightarrow{Z^0} \nu_l' + N^*\tag{1.1}$$

  Some of the neutrino energy and momentum is transferred to the constituents of the nucleus. The subsequent de-excitation causes a particle cascade in the medium.

- charged current interaction: a neutrino couples to a nucleus via an electrically charged $W^{\pm}$-boson

$$\nu_l + N \xrightarrow{W^-} l^- + X\tag{1.2}$$

  The final state particles comprise a lepton and changed target X which may produce a particle cascade. Additionally,

  - an electron in the final state produces an electromagnetic cascade at the interaction position (also called vertex)
  - a tau lepton has a short lifetime and decays into leptons or hadrons producing an according cascade at a distance from the vertex which varies with energy
  - a muon in the final state will travel a long distance from the vertex until it decays or stops

---

[2]The interactions of anti-neutrinos run analogously and are not treated for simplicity.
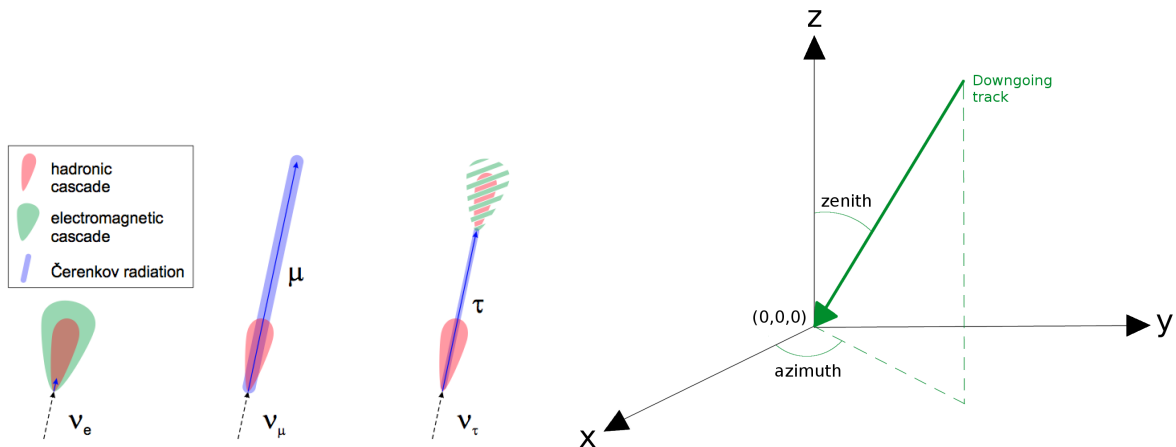
Figure 1.1: Illustration of the signatures of charged current neutrino interactions in IceCube. A neutral current interaction could result in a hadronic cascade for every neutrino flavor. Every hadronic cascade has electromagnetic sub-showers which are not illustrated here. Further cascades originating from stochastical energy losses might occur along the charged lepton path. Taken from [Wal10].

Figure 1.2: The coordinate system of IceCube is aligned to the geographic coordinate system as the y axis points towards Greenwich (UK). A particle track with zenith angle below 90° points downwards from the surface to the inner Earth. Taken from [Obe12].

Figure 1.1 displays the different neutrino event types in IceCube. Neutrinos originating from nuclear reactors, nuclear fusion in the Sun, and air showers (increasing energy with order) have already been measured for decades. Only recently astrophysical neutrinos have been detected with IceCube [Aar13a].

## 1.2   Detector design

The low interaction cross section of neutrinos implies that a large detector volume is required to achieve reasonable detection rates. The costs and technical challenges can be reduced by choosing a detection signature which does not require a dense instrumentation or an artificial detection medium. In the case of IceCube, the detection signature is Cherenkov light produced by charged particles at high velocities in transparent matter (the leptons and particle showers described in the two previous sections). The exact conditions for the production of Cherenkov light are explained in Ch. 3.3. The Cherenkov spectrum extends to all wavelengths with a maximum intensity at ultraviolet wavelengths.

The abundant background due to muons from air showers can be reduced by situating the detector deep underground. In addition the surface component IceTop can be used as a veto for air showers. IceCube's position is even deeper than required for background reduction since the properties (scattering and absorption lengths) of the natural ice match requirements at even larger depths.
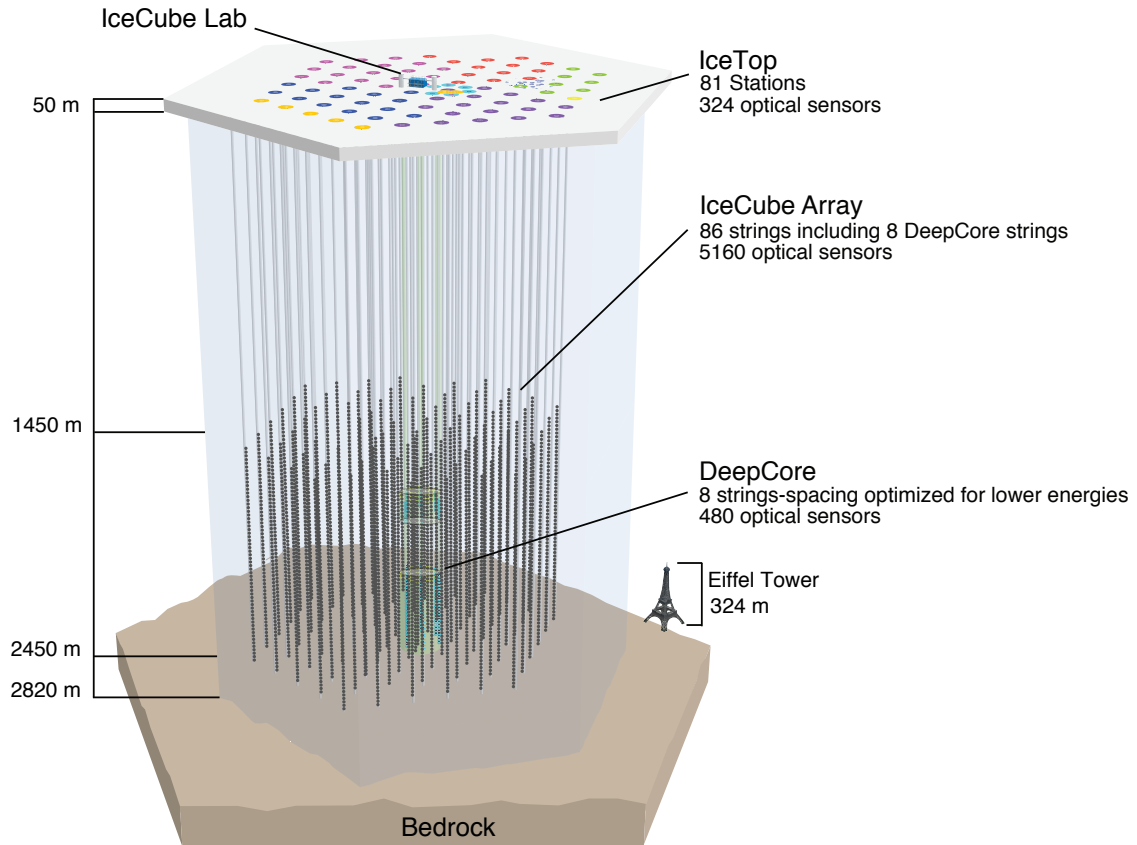
Figure 1.3: Geometry of the IceCube detector from the side. The colors show the deployment seasons during detector construction. The deployment of IceCube started in the 2004/05 season with one string of DOMs (yellow). In the following seasons 8 strings (green), 13 strings (red), 18 strings (pink), 19 strings (violet), 20 strings (blue), and 7 strings (orange) were deployed. The seasons are named after the number of strings in the regarding configuration. From here on, the configurations of further seasons differ in software only, denoted by adding the year since completion to the hardware configuration. Thus, the first season in *IC86* configuration is called *IC86-1* and the data of this season is used in this analysis. Taken from [Ice15].

1.2.1   Geometry

The IceCube detector uses the almost transparent Antarctic ice near the South Pole as detection medium [Ach06]. 4680 digital optical modules (DOMs) instrument a volume of $1\,km^3$ at depths between 1.5 to 2.5 km. 60 DOMs each are set up on 78 cable strings with a vertical spacing of 17 m and a horizontal distance of about 125 m. Another 480 DOMs are positioned more densely on eight strings in the inner core of IceCube, called DeepCore. At the top of most strings two tanks, each containing two DOMs, are deployed at the surface, building up the IceTop air shower array. The geometry of IceCube is shown in Fig. 1.3 and the corresponding coordinate system in Fig. 1.2.
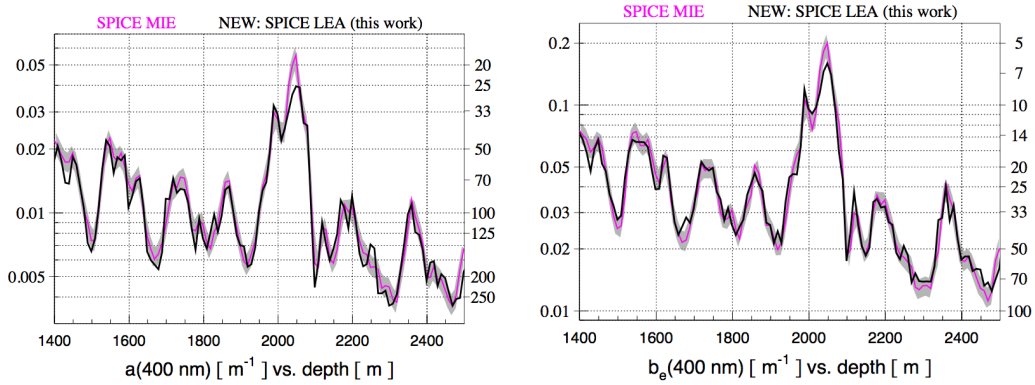
Figure 1.4: The ice properties are implemented into the ice-models as an absorption coefficient a (left) and the effective scattering coefficient b (right) which are shown in dependence of the depth. In these plots the comparison of fit values for 10 m slices is shown for the two ice-models used in this analysis. The large values around 2000 m are assumed to originate from a dust layer of volcanic ash. Taken from [Chi13].
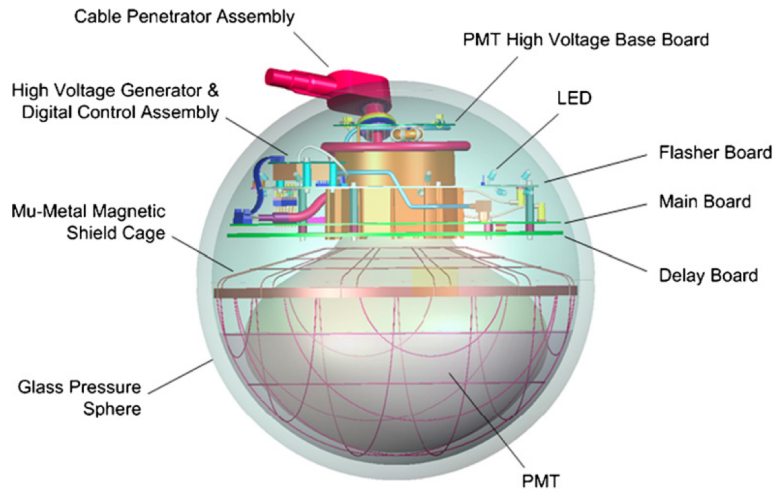
Figure 1.5: Schematic view of an IceCube DOM. The PMT has a diameter of 25 cm coupled to a glass sphere with a diameter of 35.6 cm with gel. Taken from [Ach06].

1.2.2   Antarctic ice

The optical properties of the detection medium are crucial for the interpretation of recorded data. The ice in Antarctica near the South Pole is about 2800 m thick and it is a glacier which moves about 10 m/a west at the surface. The temperature varies from $-10°$C at the bedrock to $-55°$C at the surface where there is a 50 m firn layer above the glacial ice. The glacial ice has a special structure as it originates from snow which is squeezed together by the pressure of new layers until it becomes "the most transparent solid known" [Ack06] for wavelengths between $200-400$ nm.

The derivation of the optical attenuation comprises the measurement of scattering and absorption depending on the depth, shown in Fig. 1.4. This information is collected
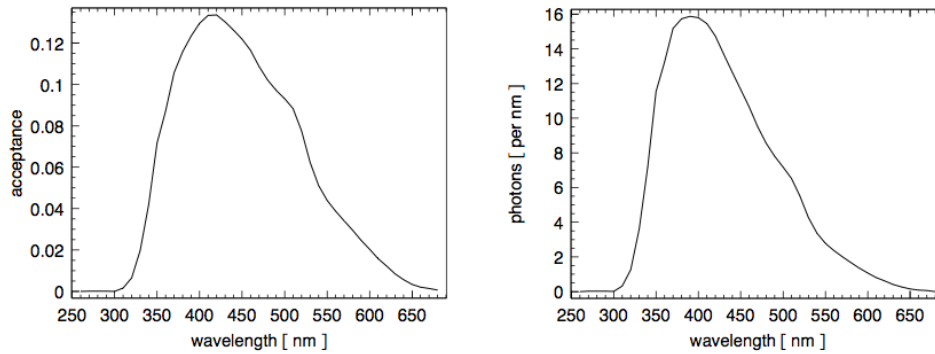
Figure 1.6: Measured DOM acceptance depending on the incident wavelength (left). The acceptance is reduced by the wavelength dependency of the DOM glass, gel and the PMT quantum efficiency. The absolute number of photons(right) is based on the photon yield of a bare muon. Taken from [Aar13b].

in the ice-model *Spice-Mie* for usage in reconstruction and simulation [Aar13b]. Spice-Mie is the ice-model used in the analysis presented later. Further measurements add the dependency on the wavelength and azimuthal direction, included in the *Spice-Lea* model [Chi13] which is used in the analysis to estimate the ice-model uncertainties. Both ice-models also implement the different properties of the re-frozen ice in the string holes which contains more air bubbles than the surrounding ice.

1.2.3   DOMs

The DOMs consist of a photomultiplier tube (PMT) and supplementing read-out electronics in a glass pressure sphere, shown in Fig. 1.5 [Abb10a]. The glass properties and the wavelengths dependence of the PMT were chosen to account for the short wavelengths of Cherenkov light, see Fig. 1.6. The quantum efficiency is about a factor 10 higher for the denser instrumented DeepCore region for the detection of fainter, i.e. lower energetic, events. The time resolution is about 3 ns. Typical measurements are shown in Fig. 1.7 explaining some inherent features of PMTs. If the PMT signal exceeds a threshold corresponding to 0.25 photo-electrons (PE), this is called a *pulse* and the data acquisition (DAQ) of the DOM electronics is initiated. The group of pulses caused by one particle building the entire waveform measured at one DOM is called a *hit*.

The interpretation of the recorded data suffers from different noise sources:

- the dark noise rate of the PMT, i.e. thermionic emission at the dynodes, which is reduced because of the low environmental temperature

- radioactive decays of isotopes producing light via scintillation or luminescence in the glass which increases with lower temperature

The PMT current is read-out by a set of digitizers which gives the so called *DOMLaunch* in the unit counts per bin over time. This information is sent to the surface electronics. For
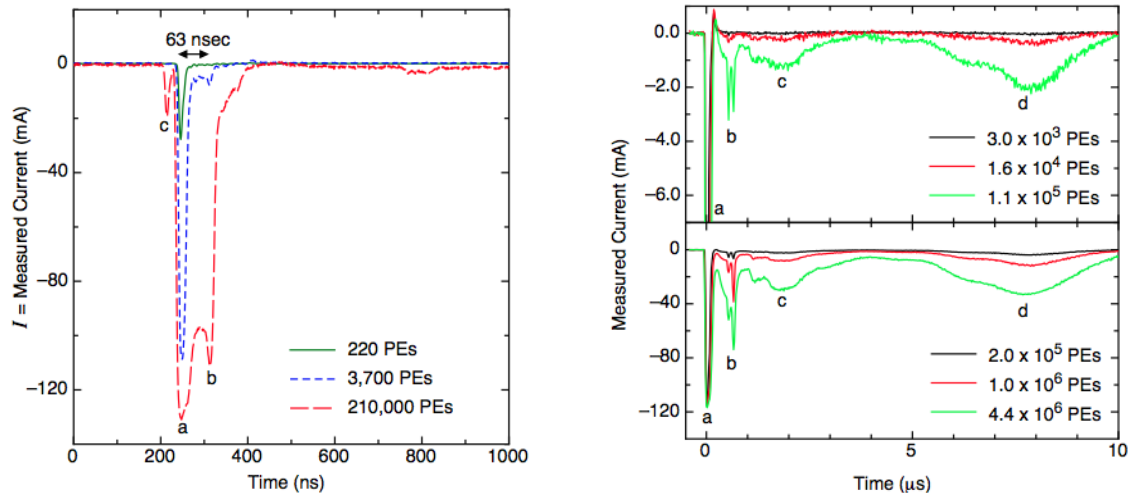
Figure 1.7: Averaged waveforms measured with an IceCube PMT for light pulses of different brightness, shown for different time scales. The left plot shows the main peak (a) where photons knock electrons off the PMT's photo-cathode. These, so called photo-electrons, are amplified by acceleration to a dynode with a potential where they knock off further electrons. This process is repeated several times until the final current is measured. The total amount of photo-electrons at the final dynode n_{NPE} is also referred to as the measured charge. The second peak (b) comes from electrons with an unusual track in the PMT. The pre-pulse (c) is produced by electrons directly originating from the first dynode. Very bright light pulses create the different waveforms shown on the right. The narrow late-pulse (b) about 600 ns after the main pulse (a) is produced by elastic backscattered photo-electrons. The broad late pulse (c) about $2\,\mu$s later and the after-pulse about $8\,\mu$s later than the main pulse are due to ions created from impurities of the PMT gas. As they are positively charged, they are accelerated back to the photo-cathode where they release multiple photo-electrons which are then multiplied and produce the after-pulse. Additional information can be found in Refs. [Ach06, Ma11]. Taken from [Abb10a].

that two DOMs are linked and connected to a copper cable which enables transportation of information and current to and from the surface. The DOMLaunches are then transformed into a waveform in mV using the calibration information for each DOM. The calibration of IceCube is described in detail in [Ach06].

If a DOM records a hit in addition to a hit recorded by the next or next-to-nearest DOM one talks about a hard local coincidence (HLC) of hits. The complete recorded information about these hits is sent to the DAQ. The remaining single hits are in soft local coincidence (SLC) mode, i.e. just a reduced information of the recorded waveform is sent to the DAQ. Further data processing is done using software and is described in Ch. 4 and in [Abb09].

Data recording is restarted at least every 8 hrs to build a new run. The requirements for *good run*s, which are used for analyses such as this analysis, are

- The run should take longer than 10 minutes.

- No external light sources were switched on.

- No significant problems arose during the run, for example a part of the data acquisition fails during the run.

- The run was monitored by a person in charge.

- The rate is stable during the run and there were no processing problems.

During detector deployment, a new season was started every year in April or May extending data acquisition to the new parts. In addition further changes in data processing are implemented at this time which is carried on after completion in an annual pattern.

1.2.4 Analysis strategy

Apart from the measurements of cosmic ray air showers, most IceCube analyses are searches for rare signals, (non-rare) signals of unknown origins, or other unpredictable features. The confidence in the results of such analyses could suffer from experimental bias [Roo03]. Therefore these IceCube analyses follow a blind analysis strategy. This is realized by basing the analyses on simulated signal and background only. The simulation quality can be verified using $10\,\%$ of the real data recorded by IceCube per season which is called the *burn sample*. To match the burn sample, simulation imitates all physical and technical processes an event undergoes including the event processing to higher reconstruction levels which are described in Ch. 5.1.2. The analysis is applied on the complementary $90\,\%$ of data (the data is unblinded) only after the analysis is finalized, i.e. all criteria for signal selection are fixed, the interpretation strategy is developed, and the analysis is approved by the IceCube collaboration.

1.3 Discussion

The IceCube design requires the following prerequisites from detectable particles

- the ability to interact with matter depending on a sufficiently large cross section and flux

- production of light in ice with short wavelengths (according to Fig. 1.6) and sufficient brightness for the sparse instrumentation

- capability to penetrate the atmosphere and ice down, or through Earth up, towards the detector

- relativistic particle velocities $v \gtrsim 0.4\,c$ (or very low velocities $v \lesssim 0.1\,c$ since IC79) are expected by the data acquisition system. However, this criterion can be loosened in software.

These criteria can be fulfilled by many particles which are proposed beyond the standard model, such as charged dark matter particles [Kop15] or secondaries [Aar15], Q-balls [Bel98] or magnetic monopoles [Abb13, Aar14d].

In the next two chapters it will be shown that magnetic monopoles can fulfill these requirements in several ways, using a light production mechanism which has not been used in IceCube before.

2 Magnetic Monopoles

A magnetic monopole is defined as a particle[3] carrying an isolated magnetic charge. Their existence is implied or even predicted by theories of magnetism ranging from classical electrodynamics to modern quantum field theories. For example, Polchinski discusses in [Pol04] that any theory, which explains the quantization of electric charge, inevitably predicts the existence of magnetic monopoles.

However, apart from their existence no theory can currently form a full picture of a monopole, describing the creation, mass, and flux at the same time [Raj12]. Due to this lack of knowledge and the experimental intention of this work, in this chapter the proposed ranges of the monopole properties are discussed to motivate rather than to speculate. Recent theoretical and experimental constraints on the monopole flux are summarized at the end of this chapter.

2.1 Charge

As a method for further advances in theoretical physics, Dirac suggested generalizing established mathematical formalisms and to "interpret the new mathematical features in terms of physical entities" [Dir31]. He had used this method to propose the existence of electrons with positive charge [Dir28], today called *positrons*, which was experimentally confirmed in 1932 [And33]. Thus, he tried to use the same method to find "the reason for the existence of a smallest electric charge" [Dir31] e with the value[4]

$$e = \sqrt{\hbar c \alpha} \tag{2.1}$$

where $\hbar = h/2\pi$ is the reduced Planck constant and c is the speed of light in vacuum. The value of the constant $\alpha \approx 1/137$ was only known from experiments and its physical meaning was yet to be derived. Today it is known as *fine structure constant*.

Dirac first recalls that the electric scalar potential ϕ and the magnetic vector potential $\vec{A}$ are gauge invariant, i.e. different configurations of these non observable potentials generate the same observable electric $\vec{E}$ and magnetic fields $\vec{B}$ via [Max65]

$$\vec{E} = -\frac{\partial \vec{A}}{\partial t} - \vec{\nabla}\phi \tag{2.2}$$

$$\vec{B} = \vec{\nabla} \times \vec{A} \tag{2.3}$$

The divergence of the magnetic field $\vec{\nabla}\vec{B}$ vanishes for all regular $\vec{A}$ without singularity. Because there are no sources of the magnetic field the magnetic flux through the surface of a volume is zero. Therefore the vector potential $\vec{A}$ should not be able to describe an isolated magnetic source, i.e. a magnetic monopole.

---

[3]The term particle is used here in a classical interpretation despite the fact that modern monopole theories exhibit significant differences between standard model particles and monopoles.

[4]All equations in this chapter are in cgs-units (centimeter-gram-second) with the speed of light $c = \frac{1}{\sqrt{\mu_0 \epsilon_0}}$ defined by the dielectric constant ϵ_0 and vacuum permeability μ_0. This gives the substitutions $\sqrt{4\pi\epsilon_0} \to 1$ and $4\pi/\sqrt{\mu_0} \to 1$ in electrodynamic equations.

A charged particle is considered with wave function $\psi = \psi_0 \cdot e^{i\gamma}$ moving in an electromagnetic field where $\psi_0 = \psi_0(\vec{x}, t)$ is the amplitude depending on the 3-dimensional position $\vec{x}$ and the time t. The phase $\gamma = \gamma(\vec{x}, t) = \alpha(\vec{x}, t) + \beta$ is determined except for a value β. While developing modern gauge theory, Weyl showed, that the derivatives of β change along the components of the vector potential $\vec{A}$ and the scalar electric potential $\phi := A_0$ via [Wey29]

$$\vec{A} = \frac{\hbar c}{e} \cdot \vec{\nabla}\beta \text{ and } A_0 = -\frac{\hbar}{e} \cdot \frac{\partial \beta}{\partial t} \qquad (2.4)$$

Considering the particle moving on a small closed curve within the vector potential, the phase difference $\Delta\beta$ for one cycle is[5]

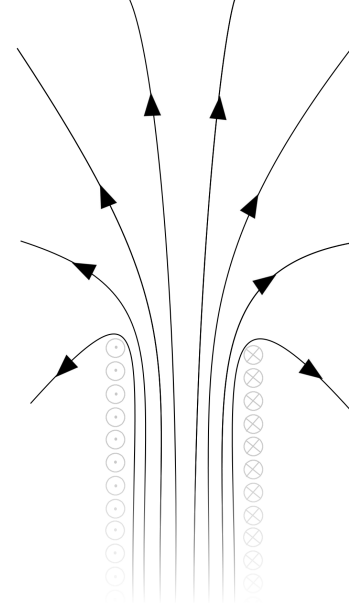$$\Delta\beta = \frac{e}{\hbar c} \oint \vec{A}\, d\vec{r} = \frac{e}{\hbar c} \Phi_m \qquad (2.5)$$

where the second equality follows from Stokes theorem yielding the magnetic flux $\Phi_m = 4\pi g$ of a magnetic charge g. This gives rise to the vector potential with singularity[6]

$$\vec{A}(\vec{r}) = \frac{g}{|\vec{r}|} \frac{\vec{r} \times \hat{k}}{|\vec{r}| - \vec{r} \cdot \hat{k}} \qquad (2.6)$$

Figure 2.1: Magnetic field calculated for a infinitely long and thin solenoid (gray). The shape of the field lines (black) at one end correspond to the field of a Dirac monopole.

With $\vec{\nabla}^2 \vec{A} = -\mu \vec{j}_e$ [Max65] the potential can be pictured as the end of an infinitesimally thin and long solenoid, i.e. a magnetic monopole connected to an infinitesimally thin *Dirac string*, illustrated in Figs. 2.1 and 3.5. as a function of the distance $\vec{r}$ of the endpoint and with the unit vector $\hat{k}$ pointing in the direction of the string. The potential is singular at the end of the string and along the string. If the phase difference $\Delta\beta$ is an integer multiple n of 2π this does not change[7] the complex value of the phase γ, i.e. the string is invisible to the particle. Thus, the end of the string acts like a classic point-like charge, that is a magnetic monopole. In this form, the vector potential is therefore consistent with quantum theory and satisfies Maxwell's equations [Max65] (given in Eqs. 2.11 to 2.14). The combination of Eq. 2.5 with $\Delta\beta = 2\pi n$ gives Dirac's quantization condition

$$2\frac{eg}{\hbar c} = n \text{ with } n \in \mathbb{Z} \qquad (2.7)$$

Thus, Dirac found that the electric charge is quantized by $e = 1/2 \cdot n\hbar c/g$ answering his initial question in an unexpected way. With $n = 1$ the quantization condition gives the

---

[5]The definition of mathematical symbols is given once every chapter. All symbols, which are used in more than one equation, are linked in to the Index for easy look-up.

[6]If the vector potential A is regular, it follows from $\vec{B} = \vec{\nabla} \times \vec{A}$ that the magnetic field has no sources $\vec{\nabla}\vec{B} = 0$. Thus, the vector potential needs to have a singularity at the origin. In addition, due to the symmetry to electric monopoles, the magnetic monopole field is modeled as $\vec{B} = \frac{g}{r^2}\hat{r}$. This gives the vector potential $\vec{A} = \frac{g\,(1-\cos\theta)}{r\sin\theta}\varphi$ in polar coordinates.

[7]Two complex numbers $e^{i\varphi_1}$ and $e^{i\varphi_2}$ are equal, when the phases differ by an integer multiple n of $|\varphi_1 - \varphi_2|/n = 2\pi$.

smallest possible charge, called the Dirac charge

$$g_D = \frac{1}{2}\frac{\hbar c}{e} = \frac{1}{2}\frac{e}{\alpha} \approx 68.5 \cdot e \tag{2.8}$$

with the fine structure constant $\alpha = e^2/\hbar c \approx 1/137$. This implies equivalently a coupling constant of [Kep96]

$$\alpha_M = \frac{g_D^2}{\hbar c} = \frac{1}{4\alpha} \approx 34 \tag{2.9}$$

for the magnetic charge. Since Dirac achieved the elemental monopole charge from basic considerations, it is not surprising that all later derivations of the monopole charge are the same or integer multiples of this elemental magnetic charge.

2.2   Mass

The concept of a gauge theory of electromagnetism, marked out in the last section, was extended further in the 1970s. The electromagnetic and weak nuclear forces could be unified into one theory above the energy scale of $\Lambda_{\text{weak}} \approx 100\,\text{GeV}$, called electroweak unification. These theories predicted the W and Z bosons which were discovered in the 1980s [Arn83, Ban83]. Also proposed was the Higgs-field [Hig64b, Hig64a, Eng64, Gur64], represented by the Higgs particle which was discovered in 2012 [Aad12, Cha12]. Some of these theories also predict a magnetic monopole in a similar way which is described in the next paragraph. Due to the large energy scale, gauge theories elude experimental confirmation, to date.

Subsequent theories, the so called *Grand Unified Theories* (GUT), predict the unification of the strong nuclear force with the electroweak theory at a higher energy scale $\Lambda_{\text{GUT}} \approx 10^{15}\,\text{GeV}$. Above the GUT scale Λ_{GUT} the corresponding Higgs field is a 3-dimensional[8] vector field. Rotations around its vectors restrict the gauge transformations. Below the GUT scale the direction of the vectors get fixed leaving only the gauge transformations allowed in the standard model [Boe04]. Every theory, describing this so called *symmetry breaking* into the standard model, generically predicts magnetic monopoles [Raj12].

The Higgs field might be in a *hedgehog configuration*, shown in Fig. 2.2, at some point, i.e. all vectors point away from one origin. During symmetry breaking, it cannot transform into a uniform vacuum state continuously at this point and stays in this topologically stable configuration. Far from the origin the Higgs field is nearly in its vacuum state. However, confined in a small volume near the origin there is an amount of energy E corresponding to the GUT scale in a small volume. This energy can also be interpreted as a mass of the value $M = E/c^2$ which also justifies the use of the term particle for this topological defect. The electromagnetic field of the hedgehog configuration can be calculated due to the dependence of electromagnetism from the Higgs-field vectors. This gives a magnetic charge of integer multiple n times the Dirac charge $g_{GUT} = n \cdot g_D$ with n depending on the GUT model [Pre84]. The mass M of a magnetic monopole is then related to the unification

---

[8]These dimensions do not span the real, but an abstract space.
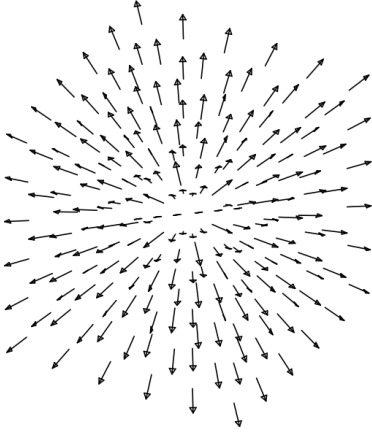
Figure 2.2: The hedgehog configuration when all vectors of the Higgs field point away from one origin. During symmetry breaking this cannot be transformed into a uniform vacuum value. Therefore, this configuration is stable and can be identified with a monopole. Taken from [Raj12].
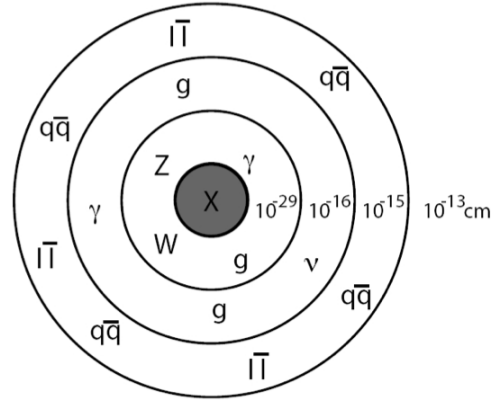
Figure 2.3: The structure of a GUT monopole. Inside the origin the original gauge symmetry of is unbroken in a radius of $R_{\text{GUT}} = \hbar c \Lambda_{\text{GUT}}^{-1} \approx 10^{-29}$ cm. According virtual gauge bosons populate the outer spheres, the electroweak region $R_{\text{weak}} \lesssim 10^{-16}$ cm and the confinement region $R_{\text{strong}} \lesssim 10^{-15}$ cm as well as fermion-antifermion pairs in $R_{\text{pair}} \lesssim 10^{-13}$ cm. Taken from [Boe04].

scale Λ of the GUT (accordingly for electroweak theory) by the coupling constant α_{GUT} (in the order of 10^{-2} for the simplest groups) [Pre84]

$$Mc^2 \gtrsim \frac{\Lambda_{\text{GUT}}}{\alpha_{\text{GUT}}} \tag{2.10}$$

If the gauge symmetry is not directly breaking into the electromagnetic gauge group but via intermediate steps, the monopole mass can be lower compared to the equation. These are *intermediate mass* monopoles. Depending on the GUT, the mass of a monopole ranges from[9] 10^{10} GeV $\leq M_{\text{GUT}} \leq 10^{17}$ GeV [Pre84, Geo74, Dan80, Wei84]. Near the origin of the topological defect the original gauge symmetry is restored. Approaching true vacuum the monopole is enclosed by shells of virtual particles, illustrated in Fig. 2.3.

Magnetic monopoles also arise in supersymmetric versions of GUT where there is an additional symmetry between bosons and fermions. The corresponding mass is then restricted to $M_{\text{SUSY}} \geq 10^7$ GeV [Kin98, Kep07]. Further unification of all forces including gravitation, as described by Superstring or Kaluza-Klein theories, predict a monopole mass of $M_{\text{String}} \approx 10^{16}$ GeV and $M_{\text{KK}} \approx 5 \cdot 10^{19}$ GeV respectively [Raj12]. Depending on the unknown physical processes involved in the evolution of the early universe there might also be monopoles with even lower masses [Raj12].

In conclusion, the predicted masses cover several orders of magnitude starting from 10^7 GeV. Monopoles with these masses cannot be produced in any foreseeable accelerator. The description of monopole production in the early universe is currently not consistent among

---

[9]For simplicity the mass unit GeV/c^2 is displayed in natural units where $c = 1$.
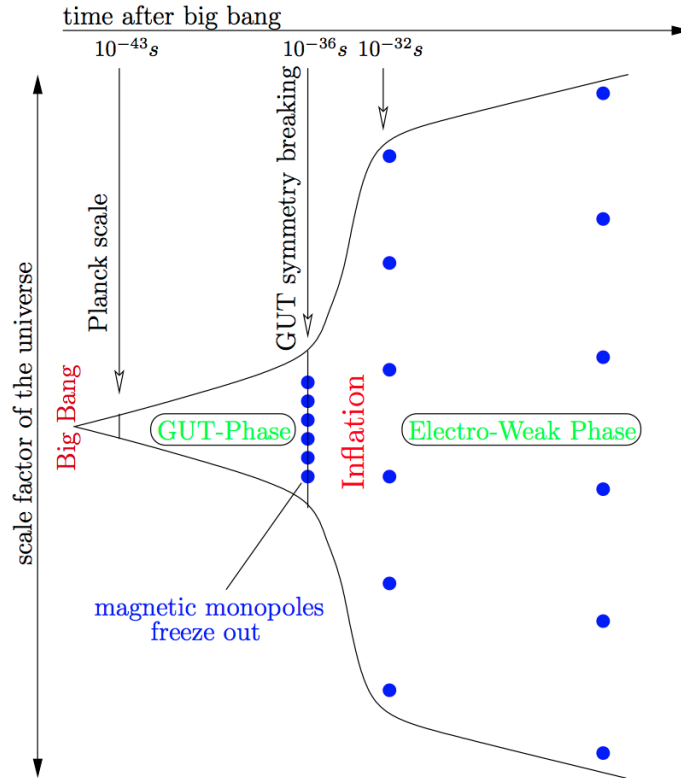
Figure 2.4: Illustration of the time evolution in the early Universe. If monopoles are created before the symmetry breaking, their density is diluted by inflation. Taken from [Glu10].

different theories [Raj12]. One model is the often referenced Kibble mechanism predicting a monopole density which exceeds the observed mass density of the Universe by calculating the number of causal domains of the Higgs field between which the monopoles are created [Kib76]. A possible solution to this so called *monopole problem*, is an inflationary expansion phase of the universe during or shortly after the time of monopole creation which tightly constrains the monopole number, illustrated in Fig. 2.4 [Raj12]. However, depending on the exact process of the inflationary phase this yields highly variable predictions for the current monopole density.

Still, there is the benefit that monopoles are predicted in almost all modern theories because they are generic solutions of symmetry breaking models and "one would be surprised if Nature had made no use of it" [Dir31]. Therefore experimental evidence for the existence of magnetic monopoles would be of great interest even without a model of their mass and flux.

2.3 Acceleration

A convenient feature of magnetic monopoles is the simple acceleration mechanism compared to cosmic rays which, for very high energies, is not solved sufficiently yet. For

that, magnetic monopoles are added in Maxwell's equations[10] which in their original form describe the generation [Max65]

$$\vec{\nabla} \cdot \vec{D} = 4\pi\rho_e \tag{2.11}$$
$$\vec{\nabla} \cdot \vec{B} = 0 \tag{2.12}$$

and interaction

$$\vec{\nabla} \times \vec{H} - \frac{1}{c}\frac{\partial \vec{D}}{\partial t} = \frac{4\pi}{c}\vec{j}_e \tag{2.13}$$

$$-\vec{\nabla} \times \vec{E} - \frac{1}{c}\frac{\partial \vec{B}}{\partial t} = 0 \tag{2.14}$$

of the electric $\vec{E} = \vec{D}/\epsilon$ and magnetic $\vec{B} = \vec{H}/\mu$ fields. In these equations ρ_e and $\vec{j}_e$ are the electric charge and current densities and ϵ and μ are the permittivity and permeability of the medium. The asymmetry between the right side of each pair of equations, which are the source terms of the fields, reflects the non-observation of magnetic monopoles. There is no theoretical reason of the asymmetry regarding the sources of electric and magnetic fields since all other aspects of electromagnetism posses symmetry between electric and magnetic fields. If magnetic monopoles exist, there would be a magnetic charge density ρ_M and a magnetic current density $\vec{j}_M$. The magnetic field would be radial and interacting via an $1/r$ potential. The Maxwell's equations would change into [Mou01]

$$\vec{\nabla} \cdot \vec{B} = 4\pi\rho_M \tag{2.15}$$

$$-\vec{\nabla} \times \vec{E} - \frac{1}{c}\frac{\partial \vec{B}}{\partial t} = \frac{4\pi}{c}\vec{j}_M \tag{2.16}$$

Then, the Lorentz force $\vec{F}_L$ of electric and magnetic fields on a moving particle with an electric Ze and magnetic charge $Z'g_D$ (see Eq. 2.8) at velocity $\vec{v}$ is derived by [Mou01]

$$\vec{F}_L = Ze\left(\vec{E} + \frac{\vec{v}}{c} \times \vec{B}\right) + Z'g_D\left(\vec{B} + \frac{\vec{v}}{c} \times \vec{E}\right) \tag{2.17}$$

The kinetic energy $T = \int \vec{F}\,d\vec{s}$, a monopole would gain while transversing one magnetic field of coherence length[11] L along the path $d\vec{s}$, is then

$$T_0 = Z'g_D \int \vec{B}\,d\vec{s} \tag{2.18}$$

$$= Z'g_D \cdot \left|\vec{B}\right| L \tag{2.19}$$

From observations and modeling the coherence length in our own galaxy is derived to be about $300\,\text{pc}$ with a field strength of $3 \cdot 10^{-6}\,\text{G}$. When a monopole once passes this domain, it would gain the kinetic energy of $T_{\text{MW}} = 6 \cdot 10^{10}\,\text{GeV}$. Even more kinetic energy could be gained in magnetic fields of star-burst galaxies $T_{\text{star}} \approx 10^{11}\,\text{GeV}$, jets of active galactic nuclei $T_{\text{AGN}} \approx 10^{13}\,\text{GeV}$, and galaxy clusters $T_{\text{cluster}} \approx 10^{14}\,\text{GeV}$ (summarized in [Wic03, Hug00]).

---

[10]These equations are in cgs-units as defined in the footnote 4 on page 11.

[11]The coherence length of a cosmic magnetic field is the extension, also called domain, where the direction of the field $\hat{k}_B = \vec{B}/\left|\vec{B}\right|$ is constant.

Considering a random-walk through n domains of coherent fields in a structure of size R the kinetic energy after transversing the structure is $T_R = \sqrt{n} \cdot T_0$ with $n = R/L$ [Kep96]. For our galaxy this gives $n \approx 184$ with $R = 55\,\text{kpc}$ of the spherical halo. Monopoles lose negligible energy in radiation processes, as explained later in Ch. 3.2.3, or inverse Compton scattering [Kep96]. Therefore, monopoles with masses smaller than the kinetic energy $M \ll T_R$, i.e.

$$M < T_{\text{cluster}} \approx 10^{14}\,\text{GeV} \tag{2.20}$$

may obtain relativistic velocities with a broad distribution of energies $\Delta T_R/T_R \approx 1$. However, the energy distribution is rather broad with the mean T_R and standard deviation ΔT_R being of comparable magnitude [Wic03].

2.4 Theoretical and experimental constraints

With the acceleration mechanism, described in the last section, monopoles gain energy from the magnetic field which loses this energy in return and might dissipate or neutralize. The dissipation rate per unit volume [Par70]

$$\frac{d\mathcal{D}}{dt} = \vec{j}_M \cdot \vec{B} \tag{2.21}$$

depends on the magnetic current $\vec{j}_M = g n_M \vec{u}$ where n_M is the monopole number density and $\vec{u}$ is the drift velocity of monopoles considered to be relativistic $|\vec{u}| \approx c$. A flux limit is calculated using the generalized energy equation

$$\frac{\partial}{\partial t}\left(E^2 + B^2\right) = 8\pi\left[-\vec{j}_e\vec{E} - \vec{j}_M\vec{B} + \vec{\nabla}\left(c\vec{E} \times \frac{\vec{B}}{4\pi}\right)\right] \tag{2.22}$$

which is derived from Maxwell's equations (adding Eqs. 2.14 and 2.15). Using Eq. 2.22 with $E = 0$ this gives a bound on the monopole density number

$$n_M < \frac{B}{8\pi Z' g_D c t} \tag{2.23}$$

with monopoles of charge $Z'g_D$. The galactic magnetic field is supposed to be generated by a dynamo effect with a time constant of $t = 10^8\,\text{a}$. This gives an upper monopole density of one monopole per 10^{26} nucleons or an upper flux limit of $\Phi_{\text{Parker}} \leq 10^{-15}\,\text{cm}^{-2}\text{sr}^{-1}\text{s}^{-1}$ which is known as Parker bound [Par70]. This approach has been refined, taking the deflection of monopoles with masses above $10^{17}\,\text{GeV}/c^2$ into account[12] [Par71] and is currently the most stringent and model independent upper limit on the monopole flux. Other theories regarding the flux limit are collected in Ref. [Oli14].

However, this limit has already been superseded by various experiments, as shown in Fig. 2.5. A comprehensive list of experiments is given in Ref. [Oli14]. Experiments, like MACRO (Monopole, Astrophysics and Cosmic Ray Observatory) were specially designed to search for magnetic monopoles in different parameter ranges [Amb02] motivated by an unconfirmed detection of a magnetic monopole in Cabrera's experiment [Cab82].

---

[12]Sometimes this correction is referred to as *Parker bound* instead of the first mention in [Par70].
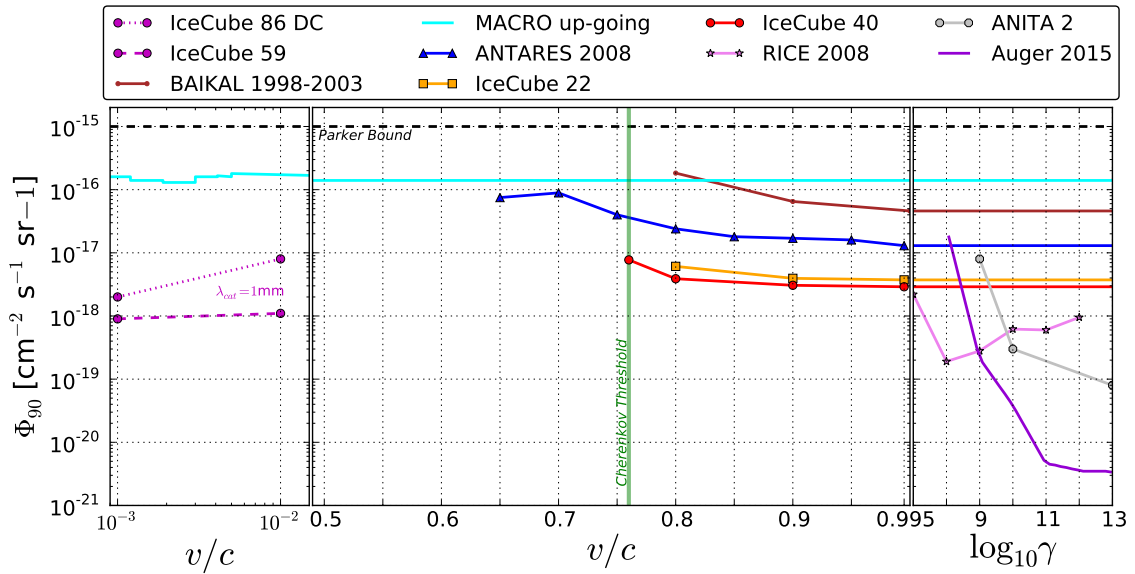
**Figure 2.5:** The Parker limit and experimental constraints previous to this analysis in the non-relativistic $v < 0.1\,c$, mildly relativistic $v < 0.76\,c$, highly relativistic $v > 0.76\,c$, and ultra-relativistic $\gamma > 10^4$ velocity ranges. $\gamma = \sqrt{1 - \beta^2}$ is the Lorentz factor for relativistic speeds. References are given in the text.

The advantage of those kind of detectors is the large parameter space as most of them can perform velocity and mass independent searches. A disadvantage are their small effective areas. Therefore, recent searches use detectors which have a large effective area, although not specialized for monopole searches. These include RICE (Radio Ice Cherenkov Experiment) based in the Antarctic ice and ANITA (ANtarctic Impulsive Transient Antenna) a balloon observing from the atmosphere above Antarctica. They detect radio signals of charged cosmic rays and had provided the most stringent upper flux limits for magnetic monopoles with ultra-relativistic velocities [Hog08, Det11]. Recently those limits were superseded by the largest cosmic ray air shower experiment, the Pierre Auger Observatory, searching for air shower configurations which could be produced by magnetic monopoles [Fuj15].

Previous IceCube analyses covered the parameter ranges of relativistic and non-relativistic magnetic monopoles. The relativistic limits can be interpreted as a conservative estimation of ultra-relativistic limits as shown in Fig. 2.5. They were achieved with data recorded during deployment of IceCube when 22 and 40 strings were operational [Abb13, Pos13a] (referred to as IC22 and IC40 configurations). The non-relativistic analyses assume the catalysis of nucleon decay by magnetic monopoles. The sensitivity of these analyses is highly depending on the different mean free paths λ_{cat} predicted by GUT theories. The searches were performed on the datasets of the 59 and 86 string configurations [Aar14d] (IC59 and IC86-DC configuration because the latter uses just DeepCore strings).

Baikal and ANTARES (Astronomy with a Neutrino Telescope and Abyss environmental RESearch) are also neutrino detectors and use a comparable detector design to IceCube. They are built in the Russian Baikal lake and the Mediterranean sea respectively [Ayn08, AM12]. Both comprise a smaller volume with the benefit of a denser instrumentation
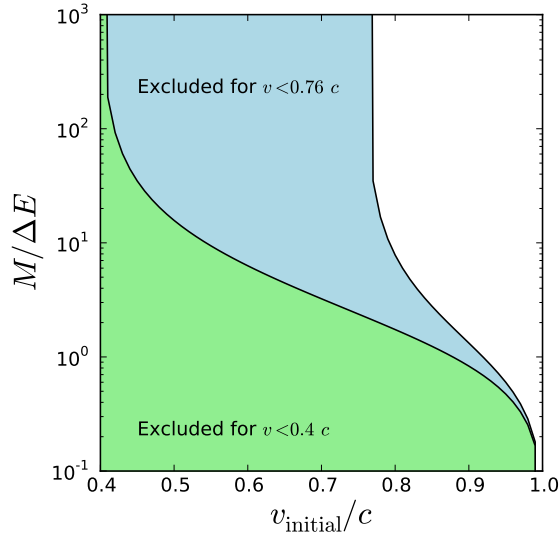
Figure 2.6: Condition for which monopoles will not be mildly $v > 0.4\,c$ (green) or highly relativistic $v > 0.76\,c$ (blue and green) after loosing an energy of ΔE while traversing the Earth. The velocity on the x-axis is the velocity of the monopole before passing through Earth. The aim of this work is to extend the velocity range from highly to mildly relativistic velocities. As shown above this would enhance the parameter range of detectable monopoles.

and lower energy threshold. Analyzers of IceCube, Baikal, and ANTARES divide the relativistic parameter range into two regions where different detection mechanisms have to be used. Direct Cherenkov light can be used above the Cherenkov threshold which is $v_c = v_{\text{ice}} \approx 0.76\,c$ in ice and $v_{\text{w}} \approx 0.74\,c$ in water. Below this threshold, detection relies on indirect Cherenkov light which is about one order of magnitude less intense. Both mechanisms are explained in detail in Ch. 3.3.

2.5 Discussion

ANTARES is the only neutrino detector which accomplished a search below the Cherenkov threshold v_c at mildly relativistic velocities. Lower velocities have never been considered[13]. This suggests a further investigation of this parameter range $< v_c$ using IceCube data which is reported in this work.

As discussed in Ch. 2.3 in Eq. 2.20, monopoles with a mass $M < 10^{14}$ GeV are expected to be relativistic. Monopoles are supposed to be extremely penetrating, slightly increasing with mass. While transversing the full diameter of the Earth a monopole loses about $\Delta E = 10^{11}$ GeV of its kinetic energy $T = M(\gamma - 1)$ assuming a mass of $M = 10^{11}$ GeV. When the monopole comes from just below the horizon it loses about $\Delta E = 10^{8}$ GeV. The regarding equations will be given in Ch. 3.2. The relation between the Lorentz factors before γ' and after γ traversing the Earth is $\gamma' - \gamma = \Delta E/M$. This gives the following

---

[13]There was also a search for monopoles with lower velocities by BAIKAL [Tro92] using luminescence light but it was never published.

condition for monopole energy and mass to traverse the Earth visualized in Fig. 2.6 [Nie01]

$$\frac{M}{\Delta E} > \frac{1}{\gamma' - \gamma} \tag{2.24}$$

It will be shown in Ch. 3 that the detector signal is not dependent on the monopole mass (apart from their direction) therefore an arbitrary mass of 10^{11} GeV is chosen for this analysis.

The charge is only restricted with the smallest value g_D, however, most of the models predict a charge of $n \cdot g_D$ with $n = \{1, 2\}$. The brightness of the simulated monopole signal depends on the charge with less than the factor n^2, as will be shown in Ch. 3. This is small compared to the variation of brightness in dependence of the velocity. Therefore a monopole charge of g_D is assumed in this analysis. This assumption will result in a conservative limit.

A possibly detected monopole signal could be analyzed regarding the energy and direction to estimate its charge and mass. This would enable the choice of appropriate theoretical models predicting the corresponding parameter ranges and therefore a constraint of the models describing the development of the early universe.

3 Interaction with matter

To find detection signatures for magnetic monopoles, one has to study their interaction with matter. IceCube is designed to record Cherenkov light which restricts this study to light producing mechanisms. For monopoles there are currently three proposed mechanisms

- direct Cherenkov light induced by the magnetic charge of the monopole itself

- indirect Cherenkov light by

  - δ-electrons from the ionization of atoms by the monopole
  - electrically charged secondaries from the catalysis of nucleon decay by the monopole (see App. A.2)
  - radiative energy losses

- luminescence light due to the excitation of atoms by the monopole (see App. A.1)

As shown in Ch. 2.4 multiple analyses have been performed using direct Cherenkov light and the catalysis of nucleon decay as detection signature. Luminescence light has not been studied yet since it is strongly dependent on the structure and state of the detection medium and there are no suitable measurements for IceCube's ice configuration.

The indirect Cherenkov light by ionization has not been used for monopole searches in IceCube so far, however, there is a search using the ANTARES detector. ANTARES is more densely instrumented than IceCube which leads to a lower threshold in detecting less intense signals. However, it is shown in [Obe12] that monopole signals with only indirect Cherenkov light can be bright enough to be detected by IceCube.

Since this is the first analysis of this kind in IceCube a literature study was done to collect the information about monopole interactions which is needed to simulate the signal in the detector. The following chapter is focused only on the theory of direct and indirect Cherenkov light production. For completeness a short overview of luminescence and nucleon decay are given in the App. A.2 and A.1.

The calculation of indirect Cherenkov light depends on several prerequisites which have to be discussed before showing the final derivation. While the monopole passes through matter, it loses energy through interactions with the surrounding matter depending on its velocity. To calculate the energy loss rate, the interaction cross section which describes the monopole interaction in medium is required. Analyzers and theorists of recent papers chose two different cross sections. Those are discussed in the following chapter to decide which one to use in this analysis. The corresponding energy loss rate is introduced in the second part of this chapter.

The last part of this chapter explains direct Cherenkov light from electrically and magnetically charged particles. Indirect Cherenkov light is produced by electrons knocked off their atoms by the monopole depending on its velocity. Therefore, indirect Cherenkov light depends on the energy loss rate of monopoles in matter leading to ionization. Eventually all equations are combined to calculate the total photon number and angular distribution of indirect Cherenkov light.

3.1 Monopole-electron cross section

The interaction cross section gives the probability for Coulomb-scattering of an atomic electron in the field of a monopole. According to Fermi's Golden Rule[14] the cross section depends on the transition matrix M_{fi} [Fer50, p. 140]

$$\sigma \propto |M_{fi}|^2 \tag{3.1}$$

where

$$M_{fi} = \langle \psi_f | \mathcal{H} | \psi_i \rangle = \int \psi_f^* \mathcal{H} \psi_i dV \tag{3.2}$$

The interaction potential is described by the Hamilton operator $\mathcal{H}$ which transforms the initial wave function ψ_i of an incident particle into the final wave function ψ_f after scattering. The Hamilton operator is given by the kinetic $\mathcal{T}$ and potential $\mathcal{V}$ energy operators $\mathcal{H} = \mathcal{T} + \mathcal{V}$ which are different for electric and magnetic charges.

Usually the interaction cross section is given in a differential form $d\sigma/d\Omega$. $d\sigma$ is defined to be the flux of particles in state ψ_f scattered into the space angle $d\Omega$ per unit time, divided by the flux density of the initial wave ψ_i. Additionally, cross sections are often shown as a form factor F which is defined as the ratio to the Rutherford cross section σ_R described in the next section

$$F = \frac{\sigma}{\sigma_R} \tag{3.3}$$

or corresponding differential forms. Following this approach first the Rutherford cross section for monopoles is introduced in this chapter. Based on this, the two monopole cross sections, one finds in literature for the inelastic Coulomb scattering, are called *Mott* and *KYG* (Kazama Yang and Goldhaber) cross section.

3.1.1 Rutherford cross section

The Rutherford cross section σ_R uses the simplest approach for the derivation of cross sections with a semi-classical ansatz. An elastic scattering is assumed where

- both particles are point-like, have no spins and no magnetic moment

- the incoming particle is not relativistic

- the recoil of the target is negligible

---

[14]Fermi's Golden Rule: If an initial state is exposed to an outer disruption, here the scattering M_{fi}, the probability per unit time to transform into the final state is given in first order by $W = \frac{2\pi}{\hbar} |M_{fi}|^2 \cdot \rho(E')$ where W is the reaction rate per target particle and per incoming particle and $\rho(E')$ is the density of final states of energy E' and $W \propto \sigma$ [Pov09].
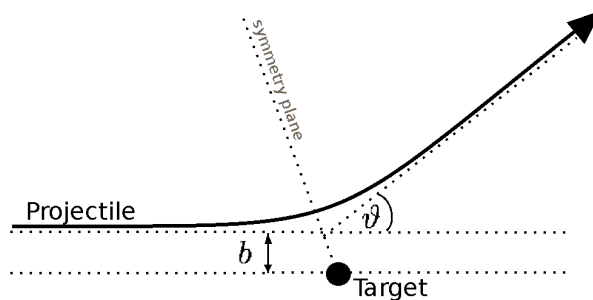
Figure 3.1: Coloumb scattering of an electron off a heavy electric charge or a magnetic monopole where b is the impact parameter and ϑ is the scattering angle. The impact parameter is defined as the perpendicular distance from the target to the direction of the incident particle if there were no interactions between them. The dependence of the scattering angle and the impact parameter is given by $b \propto \cot(\vartheta/2)$. In a Coulomb potential the path of the incident particle follows a hyperbola.

For an electric charge scattering off a target, which is a comparably heavy electric charge, the cross section is calculated in [Bau51] with the potential energy operator $\mathcal{V}$ and the electric field ϕ of the target

$$\mathcal{V}(\vec{r}) = e \cdot \vec{r}\,\vec{\phi}(\vec{r}) \ \text{with} \ \vec{\phi}(\vec{r}) = Ze\frac{\vec{r}}{r^3} \tag{3.4}$$

where $\vec{r}$ is the position of the electron and Ze is the charge of the target generating a radially symmetric potential. This gives the Rutherford cross section [Rut11]

$$\left(\frac{d\sigma}{d\Omega}\right)_R^{el} = \left(\frac{Z'e \cdot Ze}{4T_0}\right)^2 \frac{1}{\sin^4\frac{\vartheta}{2}} \tag{3.5}$$

where ϑ is the scattering angle (see definition in Fig. 3.1), $Z'e$ is the charge of the incident particle ($Z' = 1$ for electrons), and T_0 is the kinetic energy of the projectile before the scattering.

The first ever calculations of the monopole cross section were executed in 1951 [Bau51, Col51]. The potential operator of a magnetic monopole, acting on a stationary electron (bound to a nucleus), is

$$\mathcal{V}(\vec{R},\vec{r}) = -\frac{e}{c}\left[\vec{r}\cdot\left(\vec{v}\times\vec{H}(\vec{R})\right)\right] \ \text{with velocity} \ \vec{v} = \frac{\hbar}{2M}(\vec{p}_i + \vec{p}_f) \tag{3.6}$$

where M is the mass of the monopole, $\vec{R}$ is its position vector relative to nucleus on which the electron is bound. The monopole interacts with this electron at point $\vec{r}$ and $\vec{p}_{i/f}$ are the initial and final momenta of the monopole. The magnetic field for a magnetic charge g is given by

$$\vec{H}(\vec{R}) = g\frac{\vec{R}}{R^3} \tag{3.7}$$

which is symmetric to the electric field in Eq. 3.4. The result of Bauer's calculation is

$$\left(\frac{d\sigma}{d\Omega}\right)_R^{m} = \left(\frac{g\beta \cdot Ze}{4T_0}\right)^2 \frac{1}{\sin^4\frac{\vartheta}{2}} \tag{3.8}$$
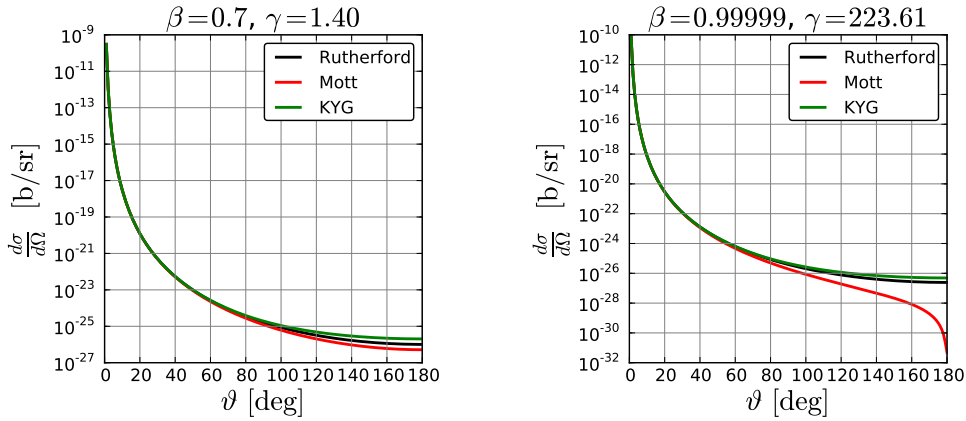
Figure 3.2: Comparison of differential cross sections for mildly relativistic (left) and ultra relativistic (right) monopole velocities.

where $\beta = v/c$ is the monopole velocity in terms of the speed of light c. Since the potential of a monopole depends on the monopole velocity, the cross section between a stationary electron and a magnetic monopole can be calculated by replacing the electric charge $Z'e$ with the monopole charge and velocity $g\beta$ in the Eq. 3.5 for electric charges.

The Rutherford differential cross section diverges for $\vartheta \to 0$ due to the infinite range of the Coulomb potential. This means that the probability for the incident particle to pass by the target (interacting while not changing the direction) is much higher than the probability to scatter off the target due to the small cross section.

3.1.2   Mott cross section

Differing from the Rutherford cross section, the Mott cross section assumes an elastic scattering where

- the incoming particle has a relativistic velocity
- the electron has the spin $\frac{1}{2}$ and magnetic moment; the monopole target has no spin
- the recoil of the target is taken into account

The result is the modification of the Rutherford cross section with the form factor [Bau51, Ahl75]

$$F_M(\beta) = 1 - \beta^2 \sin^2 \frac{\vartheta}{2} \tag{3.9}$$

The backward scattering $\vartheta = \pi$ is suppressed because the target has no spin. This is approximately also the case for monopoles because of their high mass allowing the approximation of their spin to be 0 [Ahl80]. The influence of the spin is of the order of the inverse particle mass $1/M$ [Pes94] which is very small for a magnetic monopole. The difference of the described cross sections is shown in Fig. 3.2 for two velocities.

To show the cross section in dependence of the final electron energy T the following approximation for the scattering angle is used [Ahl75]

$$\sin^2 \frac{\vartheta}{2} \approx \frac{T}{T_{\max}} \qquad (3.10)$$

where $T_{\max}$ is the maximum energy transfer between monopole and electron [Oli14, eq. 32.4] which is illustrated in Fig. 3.3

$$T_{\max} = \frac{2m_e c^2 \beta^2 \gamma^2}{1 + \frac{2\gamma m_e}{M} + \left(\frac{m_e}{M}\right)^2} \qquad (3.11)$$

Figure 3.3: Maximum energy $T_{\max}$ transferred between monopole and electron using the correction factor for Mott.

where m_e is the electron mass, M is the mass of the incident particle (here the monopole mass), $\beta = v/c$ is the speed in terms of c, and γ is the Lorentz factor $\gamma = 1/\sqrt{1 - \beta^2}$. Most calculations use the approximate values for $T_{\max}$

$$\Rightarrow T_{\max} \approx \begin{cases} 2m_e c^2 \beta^2 \gamma^2 & \text{for } \frac{2\gamma m_e}{M} \ll 1 \\ M c^2 \beta^2 \gamma & \text{for } \frac{2\gamma m_e}{M} \gg 1 \end{cases} \qquad (3.12)$$

although they might introduce a non negligible error [Oli14]. The energy transfer can also be expressed as a function of the impact parameter b [Jac99]

$$T(b) \propto \frac{1}{b_{\min}^2 + b^2} \qquad (3.13)$$

where $b_{\min}$ is the lower limit of the impact parameter.

Quantum-mechanical effects, not considered by the Rutherford cross section, can be taken into account as a modification of $b_{\min}$ in papers prior to the calculation of the Mott cross section. For a scattering angle of $\theta = 0°$ the energy transfer can be calculated classically. However, for large scattering angles up to $\theta = 180°$ the Heisenberg uncertainty relation has to be considered with $b_{\min} > \hbar/p$ which reduces the corresponding maximum energy transfer $T_{\max}(b = b_{\min})$ to approximately[15] [Boh13, Col51]

$$T_m = k \cdot T_{\max} \text{ with } k \approx 0.69 \qquad (3.14)$$

This is used by Ahlen in [Ahl75], where he summarizes the calculation of the Rutherford cross section, only briefly mentioning the Mott Form factor, and shows the application for monopole searches. The latter is referenced in the ANTARES analyses which all use the Mott cross section [Ric02, vR06a, PC10, AM12]. However, as written in [vR06b], the

---

[15]In the context of monopole interaction with matter the references [Ahl75, Dom70a] are usually given as original sources. Ahlen summarizes a calculation, similar to what is done in Ch. 3.3, using the Rutherford cross section. Regarding the correction factor k he refers to [Jac99] in the version of 1967. Domogatski cites [Col51] in connection with the energy loss of monopoles in matter without mentioning k. The correction factor was originally calculated for standard model particles and with the help of [Col51], the calculation of this number can be traced back to [Boh13].
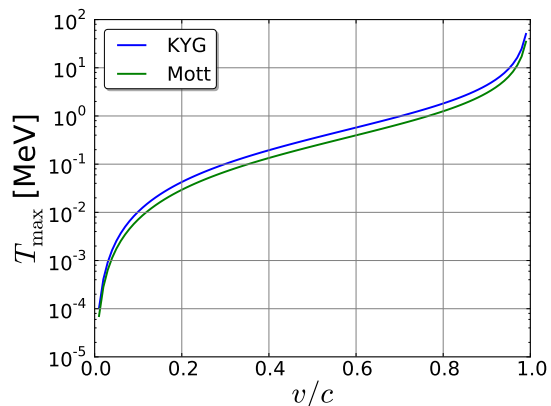
correction factor k is not needed for the Mott cross section. The electric Mott cross section is then [Ber12, eq. 32.1]

$$\left(\frac{d\sigma}{dT}\right)_M^{el} = \frac{2\pi r_e^2 c^2 Z'^2}{\beta^2}\left(\frac{1 - \frac{\beta^2 T}{T_{\max}}}{T^2}\right) \tag{3.15}$$

where r_e is the classical electron radius $r_e = e^2/m_e c^2 \approx 2.81\,\text{fm}$. The same transition from $d\sigma/d\Omega$ to $d\sigma/dT$ can be used for the KYG cross section of magnetic monopoles described in the next chapter. The factor T_m is required only when this transition is used for the Rutherford cross section.

3.1.3 KYG cross section

As described in Ch. 2.1 the vector potential $\vec{A}$ has a singularity at the position of the monopole. For a time, this prevented calculation of the scattered wave functions using the Dirac equation [Dir58] to be consistent with both quantum mechanics as well as special relativity. This was solved in 1977 with the so-called KYG cross section [Kaz77] which takes into account (additionally to the Mott cross section)

- helicity flip and non-flip amplitudes of the cross section for relativistic velocities taking the spin into account[16]

- the vector potential $\vec{A}$ (in opposite to the magneto-static way before)

The issue with the singularity of the vector potential was solved by using one-dimensional *vector bundles* (also called line bundles) [Wu76]. Two overlapping regions around the singularity (the position of the monopole) are defined which are each singularity-free. This is explained in [dS15] as "analogous to the problem of terrestrial geographic poles when trying to map the Earth's surface with a single chart." These regions R_a and R_b are defined in terms of zenith angle θ as
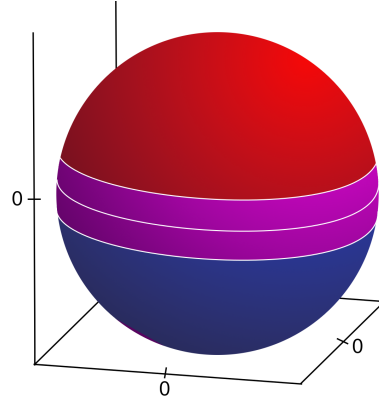
Figure 3.4: Regions of the line bundle where red is R_a, blue is R_b, and violet is R_{ab}. The latter is the overlapping region with $\delta = 0.1 \cdot \frac{\pi}{2}$.

$$R_a: \quad 0 < \theta < \frac{1}{2}\pi + \delta \tag{3.16}$$

$$R_b: \quad \frac{1}{2}\pi - \delta < \theta < \pi \tag{3.17}$$

with $0 < \delta \leq \frac{1}{2}\pi$ defining the overlapping region, illustrated in Fig. 3.4. The two different vector potentials for these two regions are given in spheric coordinates (r, ϕ, θ) with the

---

[16]The helicity is defined as the projection of the spin onto the direction of the momentum.
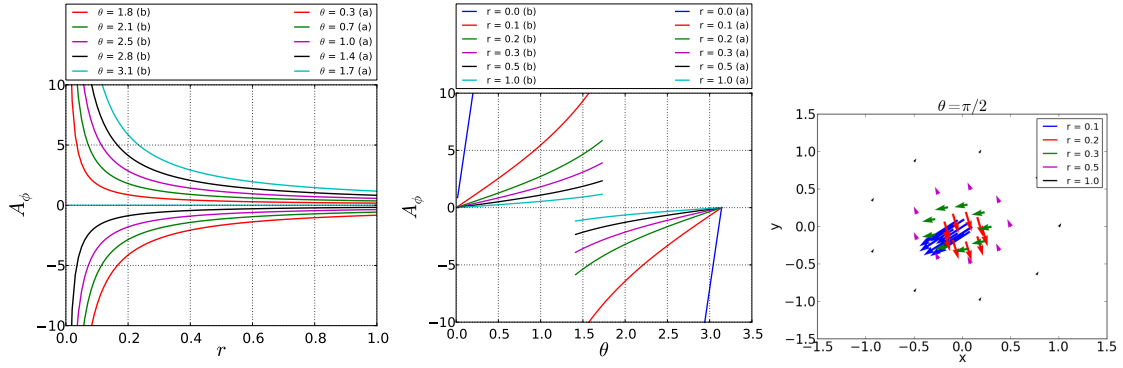
Figure 3.5: The vector potential A_ϕ drawn in 2 dimensions depending on radius (left, right) in arbitrary units and theta (middle) for both regions overlapping with $\delta = 0.1 \cdot \frac{\pi}{2}$. The field is stronger the nearer to the origin $r = 0$ and $\theta = \frac{\pi}{2}$. The direction of the vector potential is rotating.

monopole as origin

$$(A_r)_a = (A_r)_b \quad = \quad 0 \tag{3.18}$$

$$(A_\phi)_{a/b} \quad = \quad \frac{\pm g}{r \sin \theta}(1 \mp \cos \theta) \tag{3.19}$$

$$(A_\theta)_a = (A_\theta)_b \quad = \quad 0 \tag{3.20}$$

For illustration these are plotted in Fig. 3.5. The potentials can be transformed into each other by a transition function

$$S_{ab} = e^{2i \cdot Zeg \cdot \phi} \tag{3.21}$$

This function also transforms the electron wave functions in the field of a magnetic monopole

$$\psi_a = S_{ab}\psi_b \tag{3.22}$$

The last equation is the definition of a *section* (a function) on the line bundle, thus ψ is a section. A linear combination of three sections is used in [Kaz77] to calculate the so-called KYG form factor. An extra infinitesimal magnetic moment had to be added to the equations describing the monopole to prevent the electron passing through the undefined region in the core of the monopole. This does not change the derived cross section. The contribution of the spin at relativistic speeds increases the helicity flip cross section, i.e. when the spin does not flip, for large scattering angles, illustrated in Fig. 3.6. The helicity non-flip cross section, i.e. when the spin flips, is comparable with the Mott cross section. Eventually, the helicity flip and non-flip amplitudes are summed which yields the KYG form factor

$$F_K = \left(\frac{g\beta}{Ze}\right)^2 \left[\frac{T^2}{(Zeg)^2}\sin^4\frac{\vartheta}{2} + 2\left(\sin\frac{\vartheta}{2}\right)^{4Zeg+2}\right] \tag{3.23}$$

This is valid for both regions. The form factor is given as tabulated values in [Kaz77] which are fit for use in this analysis[17], shown in Fig. 3.7. The correction factor of Eq.

---

[17]The fit is used instead of the actual equation, since this simplifies the integration over this term.
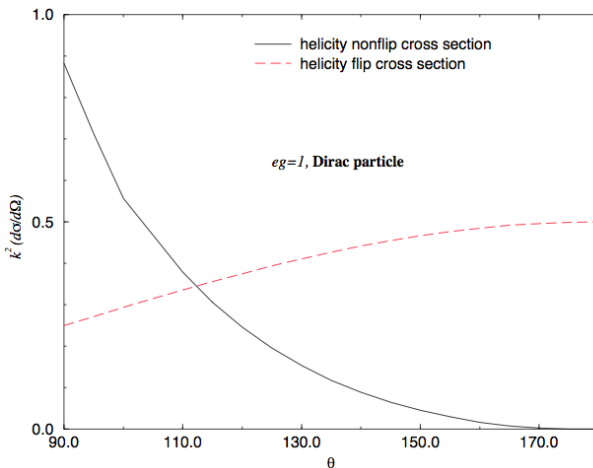
Figure 3.6: Relative contribution of helicity-flip and helicity-nonflip amplitudes of the KYG cross section. Taken from [Mil06].
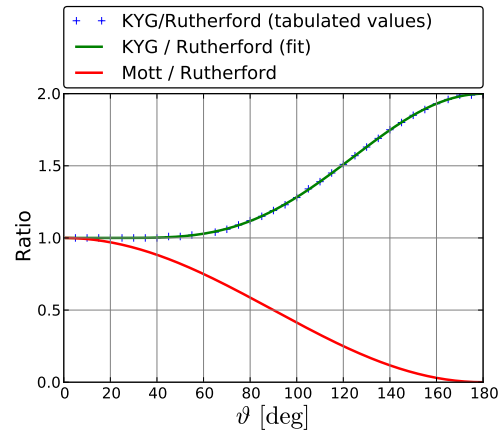
Figure 3.7: Fit of the KYG form factor values which are divided by the Rutherford cross section. Also shown is the ratio of Mott form factor and Rutherford cross section.

3.14 is not needed here because this cross section is calculated in full terms of quantum electrodynamics (QED). Due to this form factor the KYG cross section does not decline as much as the Mott cross section for a large scattering angle ϑ.

3.1.4   Discussion

Since the KYG cross section is most advanced, fully respecting electro-dynamics, quantum mechanics, and special relativity, this cross-cross section is chosen for this analysis. However, the only comparable analysis from ANTARES [AM12] uses the Mott cross section and references the summary of Ahlen [Ahl75], who used the original descriptions by Bauer and Cole [Bau51, Col51]. The Mott cross section leads to a less intense signal in the detector therefore a monopole with this cross section would be more difficult to detect. However, the Mott cross section cannot be used as a conservative approach for the monopole cross section, since the resulting detector signal differs too much (compare [Obe12]). Therefore, future ANTARES analyses will also use the KYG cross section [Pos13b].

In addition, Ahlen himself uses the KYG cross section after it was published [Ahl78] and argues that this cross section must be valid within an uncertainty of 3% [Ahl78]. This is also reflected by a negligible number of citations of Ref. [Ahl75] while Ref. [Kaz77] is mentioned in reviews [Mil06] and textbooks [Esp04]. The KYG cross section is mentioned in analyses by BAIKAL[18] and AMANDA [Ayn08, Nie01]. The KYG approach was also used to calculate the quark-monopole cross section [Rat09].

---

[18]Despite mentioning the KYG cross section, the correction factor of Eq. 3.14 is also used in [Ayn08] referencing [Dom70b]. The monopole cross section is not discussed in the referenced paper. So it cannot be retraced why the factor is used in this combination. It is not used when the KYG cross section is applied in all the other mentioned references.

3.2   Energy loss

The cross section can now be used to calculate the energy loss of monopoles in matter due to electronic interactions. That is ionization and atomic excitation of the medium, also referred to as collisional losses. This consideration is restricted to intermediate relativistic velocities of the incident particles. However, energy losses due to radiative processes as well as strong and weak interactions are briefly summarized for completeness. The energy loss is calculated in three steps:

- First the distant collision, leading mostly to atomic excitation, is calculated using the Born approximation [Bor26] neglecting the electron spin and the inner structure of the heavy charge.

- For lower impact parameters the atom cannot be approximated as point like any more and the form factor of the charge distribution has to be taken into account. The close collision contribution to the energy loss, leading mostly to atomic ionization, can be calculated using a semi-classical approach as shown for the Mott cross section in Ch. 3.1.2. An improved ansatz is the quantum electrodynamic calculation described in Ch. 3.1.3.

- Finally Bethe's sum rule [Bet30] allows to join the distant and close collision equations.

At large distances and at high velocities, the electromagnetic interaction of monopoles is comparable to the interactions of heavy ions of charge $Z \propto \sqrt{\alpha_M/\alpha} \propto 1/2\alpha \approx 68$ with the monopole coupling α_M from Eq. 2.9. The resulting energy loss rate is first shown for standard model particles for comparison and later use.

3.2.1   Standard model particles

For heavy particles, e.g. α-particles, with a speed of $0.1 \lesssim \beta\gamma \lesssim 1000$ the mean rate of the energy loss dE per unit path length dx in a medium is given by[19] [Oli14]

$$-\left\langle \frac{dE}{dx} \right\rangle = \frac{4\pi N_e \cdot Z^2 e^2 \cdot Z'^2 e^2}{m_e \beta^2} \left[\frac{1}{2} \ln \frac{2m_e c^2 \beta^2 \gamma^2 T_{\max}}{I^2} - \beta^2 - \frac{\delta(\beta\gamma)}{2} \right] \tag{3.24}$$

in units of $\mathrm{MeV\,cm^2/g}$, where I is the mean excitation energy of the target in units of eV, and δ is the density effect correction. The latter accounts for the deformation of the electric field of a particle at relativistic velocities which limits its interaction with the medium. The values for I and δ can be found in Ref. [Ste84] or with the help of Ref. [Oli14]. The electron density N_e in units of $\mathrm{m^{-3}}$ is given by

$$N_e = \rho \cdot \frac{Z}{A} \cdot N_A \tag{3.25}$$

---

[19]This equation is in cgs-units as defined in the footnote of page 4.

where ρ is the density, N_A is the Avogadro constant, Z is the average atomic number, and A is the average atomic weight. The mean energy loss decreases with increasing velocity up to about $\beta\gamma = 3.5$ where it starts to increase again. The energy loss rate in media with higher atomic numbers Z' is slightly decreasing with Z/A.

For lower velocities $\beta\gamma \lesssim 0.1$ shell corrections must be considered and for higher velocities $\beta\gamma \gtrsim 1000$ radiative effects must be taken into account. The energy loss is almost independent of the mass M of the incident particle which only enters through $T_{\max}$. This equation for the mean rate of the energy loss is supported by experimental measurements and valid within a few percent [Oli14].

The energy loss of electrons in the considered velocity range has almost the same shape. The difference is due to the indistinguishability of the incident electron with the electron of the atom it ionizes, as well as spin, charge, and kinematics. The faster electron after interaction is considered to be the incident particle. It gains a maximum kinetic energy of $T_{\max}/2$ of the transferred energy $T_{\max}$, described in Eq. 3.11 and plotted in Fig. 3.3. This gives the Moller cross section [Oli14]

$$-\left\langle \frac{dE}{dx} \right\rangle = \frac{4\pi N_e \cdot Z^2 e^2 \cdot Z'^2 e^2}{m_e \beta^2} \left[\frac{1}{2} \ln \frac{\tau^2(\tau+2)}{2(I/m_e)^2} + \frac{F(\tau)}{2} - \frac{\delta(\beta)}{2} \right] \qquad (3.26)$$

with

$$F(\tau) = 1 - \beta^2 + \frac{\tau^2/8 - (2\tau+1)\ln 2}{(\tau+1)} \qquad (3.27)$$

for electrons (different for positrons) where $\tau = \gamma - 1$ is equal to the kinetic energy of the electron divided by $m_e c^2$. Energy loss from Cherenkov radiation is included in the density effect. The energy loss due to bremsstrahlung depending on the kinetic energy of the electron is approximately given by [Oli14]

$$-\left\langle \frac{dE}{dx} \right\rangle_{\mathrm{brems}} = \frac{T}{X_0} \qquad (3.28)$$

with the radiation length $X_0 = 63.04\,\mathrm{g/cm}^2$ in water and $X_0 = 36.08\,\mathrm{g/cm}^2$ in ice. The critical energy E_c, where the energy losses due to collisional losses and bremsstrahlung are equal, is $E_c = 278.02\,\mathrm{MeV}$ in water and $E_c = 78.99\,\mathrm{MeV}$ in ice [Oli14]. Compared with $T_{\max}/2$ (see also Fig. 3.3) bremsstrahlung is a negligible effect for electrons produced by monopoles.

3.2.2 Collisional losses

The energy loss of monopoles due to electronic interactions was first calculated by Ahlen [Ahl75] based on the Mott cross sections by Bauer and Cole [Bau51, Col51]. After the publication of the KYG cross section Ahlen re-calculated the energy loss for close-collisions [Ahl78]

$$-\left\langle \frac{dE}{dx} \right\rangle_{\mathrm{close}} = \frac{2\pi N_e g^2 e^2}{m_e c^2} \left[\ln \frac{2m_e c^2 \beta^2 \gamma^2}{T_{\min}} + K(g) \right] \qquad (3.29)$$

The energy transfer, below which it is no longer valid to handle the atomic electron approximation as a free electron, is given by $T_{\min} = \hbar^2 k_0^2/(2m_e)$ where $\hbar k_0$ is the maximum
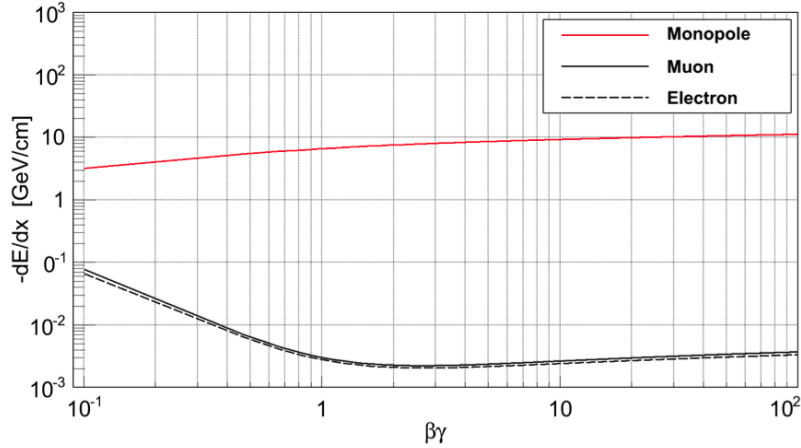
Figure 3.8: Mean energy loss rate due to collisional losses for monopoles, muons and electrons. The monopole energy loss is constantly increasing with velocity whereas the energy loss of leptons is decreasing up to $\beta\gamma = 3.5$ before increasing again. Taken from [Pos13a].

momentum transfer. $K(g)$ is a QED-correction term derived from the KYG cross section of Ch. 3.1.3

$$K(g) = \begin{cases} 0.406 & \text{for } |g| = 137e/2 \\ 0.345 & \text{for } |g| = 137e \end{cases} \tag{3.30}$$

It does not depend on β because the cross section ratio (Rutherford-KYG) is independent of the velocity. The dependence on the monopole charge is minor.

The distant-collision loss is calculated with the first Born approximation analogous to the electric equation [Lan60]

$$-\left\langle \frac{dE}{dx} \right\rangle_{\text{distant}} = \frac{4\pi N g^2 e^2}{mc^2} \left[\frac{\beta\gamma c \cdot k_0}{\omega_m} - \frac{1}{2} + \frac{\zeta^2}{2\beta^2\gamma^2\omega_p^2} \right] \tag{3.31}$$

where ω_m is the mean excitation frequency, $\epsilon(\omega)$ is the complex dielectric constant of the medium for the frequency ω, and the value ζ is defined with $\epsilon(i\zeta) = 1/\beta^2$ in a non-permeable medium with $\mu = 1$.

The equations for the distant- and close-collision energy losses are derived in terms of momentum transfer k_0 which allows the use of Bethe's generalized sum rule. If there are values of k_0 for which both equations are valid the energy loss rate is simply the sum of Eqs. 3.29 and 3.31 which is derived in [Ahl78] with intermediate steps

$$-\left\langle \frac{dE}{dx} \right\rangle = \frac{4\pi N_e g^2 e^2}{m_e c^2} \left[\ln \frac{2m_e c^2 \beta^2 \gamma^2}{I} + \frac{K(g)}{2} - \frac{\delta + 1}{2} \right] \tag{3.32}$$

where $I = 74\,\text{eV}$ is the mean ionization potential in water (calculated in [Ste56]) and δ is the density-effect correction

$$\delta = \begin{cases} 2\ln 10 \cdot x + \alpha\left[x_1 - x\right]^m + C & \text{for } x_0 < x < x_1 \\ 2\ln 10 \cdot x + C & \text{for } x > x_1 \\ 0 & \text{for } x < x_0 \end{cases} \tag{3.33}$$

31

where $x = \log(\beta\gamma)$. For water (and ice) it is $x_0 = 0.23$, $x_1 = 2.0$, $\alpha = 0.519$, $m = 2.69$, and $C = -3.47$ [Ste84]. Both values, I and δ, can be shown to be identical for the magnetic and electric cases [Ahl78].

Equation 3.32 has to be extended by the Bloch correction which accounts for the difference of the lateral extent of the electron wave functions and the monopole size. The following equation is plotted in Fig. 3.8 [Ahl78]

$$-\left\langle \frac{dE}{dx} \right\rangle_m = \frac{4\pi N_e g^2 e^2}{m_e c^2} \left[\ln \frac{2 m_e c^2 \beta^2 \gamma^2}{I} + \frac{K(g)}{2} - \frac{\delta + 1}{2} - B(g) \right] \qquad (3.34)$$

where $B(g)$ is the Bloch correction depending on the monopole charge [Ste84]

$$B(g) = \begin{cases} 0.248 & \text{for } |g| = 137e/2 \\ 0.672 & \text{for } |g| = 137e \end{cases} \qquad (3.35)$$

The strength of the monopole-electron force is $g\beta/Ze$ times larger than the force between standard model particles which leads to a high energy loss of monopoles in matter in comparison (for $Z/\beta < 68.5$). The approximations used while deriving Eq. 3.34 lead to an uncertainty of about $3\,\%$ [Ahl78]. The uncertainty could be decreased in future by developing a magnetic equivalent of the Bethe sum rule and the Bloch correction which are adopted here from the electrical case. The energy loss equation is valid for $\beta > 0.1$ below which shell corrections become important, and it is also accurate for $\gamma < 100$ as internal structure effects of the monopole are negligible.

"To sum up, the main difference of behavior between electric particles and monopoles lies in the greater ionizing power per centimeter of the monopole, except near the end of the path where the characteristic sharp increase of the ionization caused by an electric particle is completely missing" [Col51]. The reason is that the electric field of a moving monopole, and with it the ionization rate, is proportional to β. Therefore, with the effective substitution $(Z'e)^2 \rightarrow (g\beta)^2$ the factor β^{-2} in Eq. 3.24 cancels out.

3.2.3   Radiative energy losses

The energy losses due to direct and indirect Cherenkov light, described in Ch. 3.3, are minor and therefore negligible. At velocities $\gamma > 10^3$ ($\beta \approx 0.99995\,c$) radiative processes have to be considered. These are pair production, bremsstrahlung, and photo-nuclear interactions.

The rate of pair production by monopoles can be adapted from pair production of muons [Kel67, Kel68]. It dominates the total energy loss [20] [Wic03]

$$-\left\langle \frac{dE}{dx} \right\rangle_{\text{pair}} = -\frac{16\alpha^3 \alpha_M \gamma Z^2 N_A}{\pi A m_e} \left(\frac{M}{m_e} \chi(\eta) \right) \qquad (3.36)$$

between $10^4 < \gamma < 10^6$ where χ is a correction factor which depends on the fraction of monopole energy $\eta = \Delta T/T$ transferred in the interaction.

---

[20]Variable names defined before can also be found in the index on page XLIV.
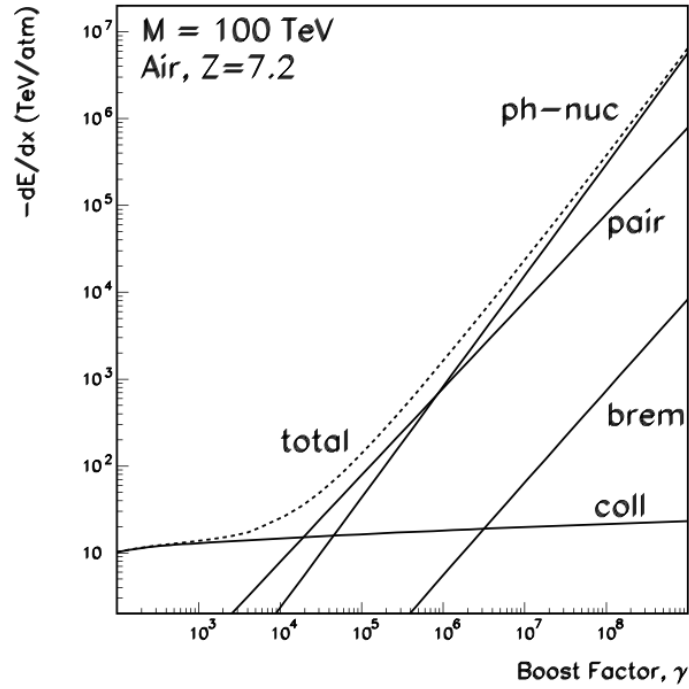
Figure 3.9: The total radiative energy losses of a light monopole $M = 10^5$ GeV and the partial contributions from bremsstrahlung, pair production, and photo-nuclear interactions. Taken from [Wic03].

The radiation due to bremsstrahlung is inversely proportional to the monopole mass M. It is calculated for electric charges in [Jac99] and adopted for monopoles in [Wic03]

$$-\left\langle \frac{dE}{dx} \right\rangle_{\mathrm{brems}} = -\frac{16}{3} \frac{\alpha \alpha_M^2 Z^2 N_A}{AM} \cdot \gamma \ln(\gamma) \tag{3.37}$$

Due to the high monopole mass (compare Ch. 2.2), bremsstrahlung is highly suppressed. The photo-nuclear cross section describes the exchange of a virtual photon between a monopole and a nucleus with a changed hadronic final state. The adoption of the lepton result [Dut01] for $\gamma > 10^6$ gives [Wic03]

$$-\left\langle \frac{dE}{dx} \right\rangle_{\mathrm{photo}} = \gamma^{1.28} \tag{3.38}$$

The three contributions to the total radiative energy loss of monopoles are shown in Fig. 3.9. Since they dominate above the considered velocity range in this analysis they can be neglected.

3.2.4 Weak and strong interactions

To this point only electromagnetic interactions have been considered. This is because weak interactions are suppressed in amplitude by a factor of M_Z^{-2} where M_Z is the mass of the neutral Z-Boson [Wic03] and will be neglected in this analysis.

Fundamental monopoles carry no color charge and therefore they do not participate in hadronic interactions. However, the unbroken symmetry in their core leads to strongly interacting particles which leak out from the core region to the confinement distance $\Lambda_{QCD}^{-1} \approx 1\,\text{fm}$. For small impact parameters these monopoles would undergo hadronic interactions leading to an energy loss of [Wic03]

$$-\left\langle \frac{dE}{dx} \right\rangle_{\text{had}} = -\frac{\gamma \Lambda_{QCD}}{\lambda_{\text{had}}} \tag{3.39}$$

where λ_{had} is the mean-free-path of a typical hadron. This expression lacks information about the precise hadronic interactions of monopoles. The hadronic energy losses are therefore linearly dependent on the Lorentz boost and can therefore be neglected for the considered velocity range of this analysis. Theycould be up to the order of losses due to pair production, .

3.3 Cherenkov light

Cherenkov light was first experimentally identified to be distinct from luminescence light by Cherenkov and Vavilov ([Che37] based on the Russian publications [Che34, Vav34])[21]. The theory was later developed by Frank and Tamm [Tam37].

3.3.1 Direct Cherenkov light from electrically charged particles

Cherenkov light is produced when electrically charged particles traverse a dielectric medium with a speed greater than the phase velocity of light c_p in the medium

$$c_p = \frac{c}{n_p} \tag{3.40}$$

where c is the speed of light and n_p is the refraction index of the medium[22]. The refraction index in ice is $n = n_p(\lambda_{\text{ref}}) \approx 1.3195$ for a wavelength of $\lambda_{\text{ref}} = 400\,\text{nm}$ which gives a phase velocity c_p or Cherenkov threshold $v_c = c_p \approx 0.75786\,c$ [War84]. The dependence of the refraction index on the wavelength is considered while implementing the calculations for simulations [Ack06], however it is omitted in the following equations for simplicity.

A charged particle with velocity v polarizes the surrounding atoms with its electric field. The relaxation of this polarization leads to the emission of weak concentric electromagnetic

---

[21] In reference [Che60] the historical development of knowledge about Cherenkov light is explained in detail. At the time of the discovery only natural sources of particle radiation were available. Cherenkov light was therefore hard to identify by eye when it was overlaid with *classic* luminescence light. The sensitivity of the eye was increased several tens of thousands times compared to the sensitivity of eyes at daylight by spending some time in complete darkness. This method also suffered from subjectivity but it allowed the first quantitative determination of the observed radiation. Cherenkov light was identified by the fact that the radiation strength could not be affected by heating the radiator or dissolving quenchers into the material. In addition the polarization was not changeable with these methods. However, this should be the case for luminescence producing mechanisms.

[22] Not to be confused with the usual definition of the speed of light in a medium which is calculated using the group velocity refraction index $n_g \approx 1.35634$ which gives $c_g \approx 0.73728\,c$ in ice [War84]. In a non-dispersive medium $n_p = n_g$.
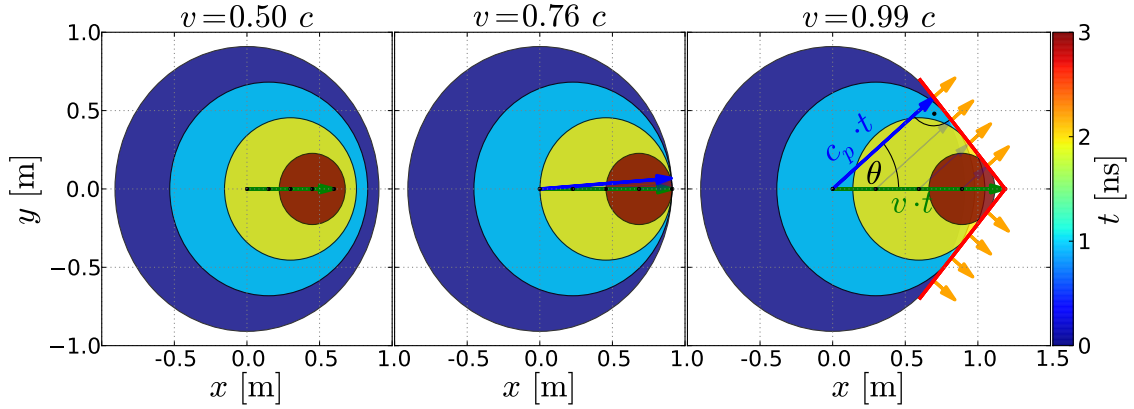
Figure 3.10: Light waves originating from a particle path (black points on green arrow) for different velocities. Smaller wave circles denote younger waves produced at a later time (see color-bar). For low particle velocities $v < v_c$ (left) the wavefronts are faster than the particle velocity. Therefore the wavefronts of different waves never cross and cannot interfere. The opposite is the case for higher particle velocities slightly (middle) and significantly (right) above the Cherenkov threshold: The wavefronts cross each other and interfere positively on a cone (red). The resulting polarized Cherenkov light (orange) then originates from this cone.

waves. For velocities below v_c the wave-fronts emitted at different times will never meet. At high velocities the wave-fronts overlap and will positively interfere at an angle θ relative to the particle track given by [Tam37]

$$\cos \theta(\lambda) = \frac{c_{\mathrm{p}}(\lambda)}{v} = \frac{1}{\beta n} \tag{3.41}$$

This defines the geometry of a cone with opening angle θ and the tip at the position of the charged particle as illustrated in Fig. 3.10. Linearly polarized light originates from this cone perpendicular to the interfering wave-fronts. If $\vec{p}$ is the momentum of the charged particle and $\vec{k}$ is the wave vector of the Cherenkov light, then the radiation is polarized in the direction of $\vec{k} \times \left(\vec{k} \times \vec{p} \right)$, i.e. the polarization vector lies in the plane between the emitted light and the direction of the charged particle.

As the radiation spectrum of the relaxation is continuos the wavelength dependence has to be considered while constructing the cone. Longer wavelengths (red) correspond to smaller angles θ as short (ultra-violet) do to larger. This is reflected by the Frank-Tamm equation for electrically charged particles[23] [Tam37]

$$\frac{d^2 E_\gamma}{dx\, d\omega} = \frac{(Ze)^2 \mu}{4\pi} \omega \left(1 - \frac{1}{\beta^2 n^2} \right) \tag{3.42}$$

where E_γ is the energy of the Cherenkov photons produced with an angular frequency ω per unit path length dx of a particle with charge Ze and speed $v = \beta c$. The permeability $\mu = \mu_0 \mu_r$ comprises of the vacuum permeability μ_0 and the relative permeability of the

---

[23]Note that the electric charge e and permittivity are hidden in the fine structure constant $\alpha = e^2/(2c\epsilon_0 h)$. The dependence of the angle θ is given because of $1/(\beta^2 n^2) = \cos^2 \theta \Rightarrow [1 - 1/(\beta^2 n^2)] = \sin^2 \theta$.
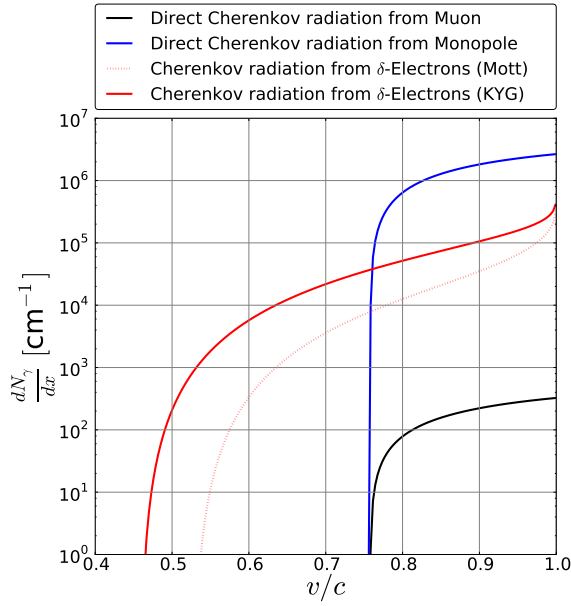
Figure 3.11: Number of photons produced by a monopole depending on its velocity, taking energy loss into account. The contribution of direct Cherenkov light (blue) and indirect Cherenkov light (red) are shown separately. For simulation they are summed up. For comparison the number of photons by direct Cherenkov light from a bare muon is shown. Taken from [Pol16].

medium μ_r. The equation can be transformed into the radiation spectrum $d^2E/dx\,d\lambda$ by using the relation $\omega = 2\pi c/\lambda$ for the substitution $d\omega(\lambda) = 2\pi c\,d\lambda/\lambda^2$

$$\frac{d^2 E_\gamma}{dx\,d\lambda} = \frac{\pi\,(Ze)^2\,c^2\mu}{\lambda^3}\left(1 - \frac{1}{\beta^2 n^2}\right) \tag{3.43}$$

Additionally the relations for the fine structure constant $\alpha = e^2/2c\epsilon_0 h$ and the speed of light $c^2 = 1/\epsilon_0\mu_0$ are used. Assuming $\mu_r \approx 1$ in ice this gives

$$\frac{d^2 E_\gamma}{dx\,d\lambda} = \frac{2\pi hc\alpha Z^2}{\lambda^3}\left(1 - \frac{1}{\beta^2 n^2}\right) \tag{3.44}$$

The radiation spectrum is proportional to λ^{-3} so that lower wavelengths dominate the Cherenkov light. Since the photon energy is connected with the photon number N_γ by $E_\gamma = N_\gamma hc/\lambda$, the photon number can be derived with $dN_\gamma = \lambda \cdot dE/(hc)$

$$\frac{d^2 N_\gamma}{dxd\lambda}(\beta_e, \lambda) = \frac{2\pi\alpha Z^2}{\lambda^2}\left(1 - \frac{1}{\beta^2 n^2}\right) \tag{3.45}$$

which gives the number of photons produced with wavelength between[24] λ_0 and λ_1 [Bel53]

$$\frac{dN_\gamma}{dx}(\beta_e) = 2\pi\alpha Z^2\left(\frac{1}{\lambda_0} - \frac{1}{\lambda_1}\right)\left(1 - \frac{1}{\beta^2 n^2}\right) \tag{3.46}$$

This is plotted for a muon in Fig. 3.11 in comparison to other kinds of Cherenkov light described in the following sections.

---

[24] The integration limits have to be limited, otherwise the number of photons would diverge for $\lambda \to 0$.

3.3.2 Direct Cherenkov light from monopoles

A magnetic charge g gives rise to a radial magnetic field $\vec{B}$ analogous to the electric field of a electric charge [Raj12]

$$\vec{B} = g\frac{\hat{r}}{r^2} \tag{3.47}$$

where $\hat{r}$ is the radial unit vector and r is the radial distance. A magnetic field moving with velocity $\vec{v}$ induces an electric field $\vec{E}$ of the form [Raj12]

$$\vec{E} = g\frac{\vec{v} \times \hat{r}}{r^2} \tag{3.48}$$

The electric field induces the production of Cherenkov light as described above. For monopoles the Frank-Tamm equation (and its integral over the wavelength) is [Tom64]

$$\frac{d^2 N_\gamma}{dx d\lambda} = \frac{2\pi\alpha}{\lambda^2}\left(\frac{gn}{e}\right)^2\left(1 - \frac{1}{\beta^2 n^2}\right) \tag{3.49}$$

$$\frac{dN_\gamma}{dx} = 2\pi\alpha\left(\frac{gn}{e}\right)^2\left(\frac{1}{\lambda_0} - \frac{1}{\lambda_1}\right)\left(1 - \frac{1}{\beta^2 n^2}\right) \tag{3.50}$$

which is similar to Eq. 3.45 when accounting for the different charge value with the effective substitution[25] $(Ze)^2 \to (gn)^2$. A monopole produces $(gn/e)^2 \approx 8200$ more photons in ice per wavelength interval compared to a particle with charge e, as can be seen in Fig. 3.11. Comparing Eqs. 3.49 and 3.45, the wavelength spectrum and the geometry of the cone remain unchanged. However, the polarization $\vec{p}_e = \vec{k} \times \left(\vec{k} \times \vec{q}\right)$ will be rotated by 90 degrees from that of an electric charge $\vec{p}_m = \vec{k} \times \vec{q}$ where $\vec{k}$ is the wave vector and $\vec{q}$ is the momentum of the Cherenkov light producing particle [Hag75, Wic03], see Fig. 3.12.
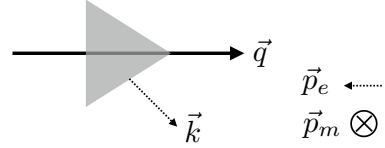
Figure 3.12: The polarization $\vec{p}$ of Cherenkov light (originating from the grey cone) by a particle with momentum $\vec{q}$ carrying electric $\vec{p}_e$ or magnetic $\vec{p}_m$ charge. $\vec{k}$ is the wave vector.

3.3.3 Indirect Cherenkov light from monopoles

When a monopole ionizes matter, it knocks electrons out of their atomic bindings. These electrons are called δ-rays or δ-electrons as they have relatively high energies and a different creation mechanism than β-radiation. Due to the high kinetic energy of monopoles this happens even if it is slower than the Cherenkov threshold. The transferred energy to electrons leads to an acceleration of many electrons above the Cherenkov threshold. The overall outline of the calculation is done as described in [Bel53], however more recent equations are also considered.

The monopole-electron cross sections derived in Chs. 3.1.2 and 3.1.3 can be used to calculate the number of generated δ-electrons N_e per unit energy interval and unit path

---

[25]The actual substitutions are $Ze \to g$ and $\mu_r \to \epsilon_r \approx n^2$.
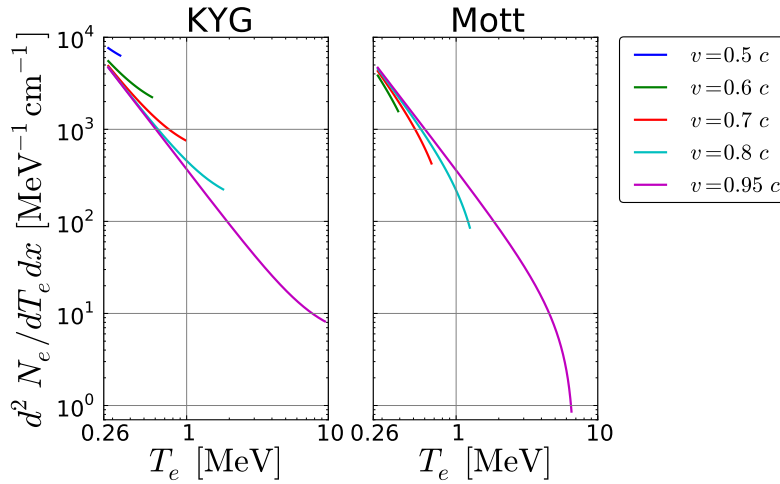
Figure 3.13: Number of electrons per unit energy interval and unit path length calculated with Mott and KYG cross sections. The KYG cross section gives more electrons with higher energies compared to the Mott cross section. For the lowest drawn velocity $v = 0.5\,c$ and Mott cross section there are no electrons with $T_e > T_0$.

length of the monopole [Ahl75, Oli14]

$$\frac{dN_e^2}{dT_e\,dx} = \frac{4\pi N_e}{T_{\max}}\frac{d\sigma}{d\Omega} \tag{3.51}$$

where N_e is the electron number density and $d\sigma/d\Omega$ is the differential cross section in the center-of-momentum frame. The transferred energy T_e in this frame depends on the scattering angle ϑ between electron and monopole [Ahl75] where $T_{\max}$ is is the maximum possible energy transfer given by Eq. 3.11. This leads to

$$\frac{dN_e^2}{dT_e\,dx} = \frac{2\pi n\beta^2 g^2 e^2}{m_e c^2 T_e^2}F(T_e,\beta) \tag{3.52}$$

where the form factors $F(\vartheta)$ of the different cross sections can be inserted when converted with Eq. 3.10. For the Mott cross section this is

$$\frac{dN_e^2}{dT_e\,dx} = \frac{2\pi n\beta^2 g^2 e^2}{m_e c^2 T_e^2}\left(1 - \beta^2\frac{T_e}{T_m}\right) \tag{3.53}$$

The result is plotted in Fig. 3.13 for different monopole velocities. Lower monopole velocities lead to a high number of electrons which are, however, restricted to low kinetic energies. Larger velocities lead to much higher electron energies with substantially decreased rate. Integration of Eq. 3.53 over T from T_0 to T_m gives the number of δ-electrons a monopole produces per unit path length dx

$$\frac{dN_e}{dx} = \int_{T_0}^{T_m}\frac{dN_e^2}{dT_e\,dx} \tag{3.54}$$

Here, the lower integration limit T_0 is derived by calculating the minimal kinetic energy
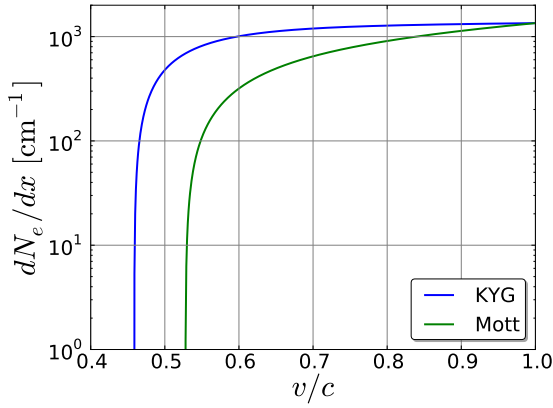
Figure 3.14: Number of δ-electrons per cm calculated with Mott and KYG cross section for comparison.
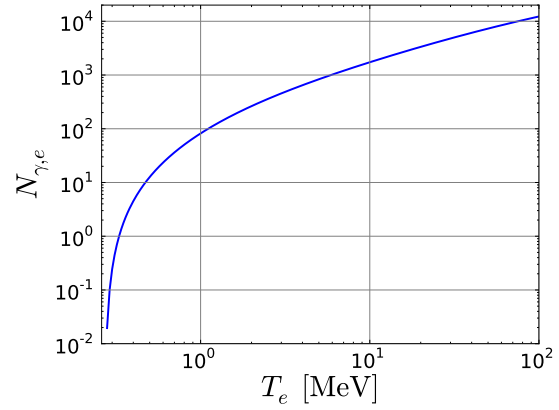
Figure 3.15: Number of photons from a δ-electron with energy T_e calculated with the Frank-Tamm formula.

the electron must have to emit Cherenkov light[26]

$$T_0 \;=\; T(v_c) - E_0 \tag{3.55}$$

$$\;=\; [\gamma(v_c) - 1] \cdot E_0 \tag{3.56}$$

$$\;\approx\; 271.8 \, \text{keV} \tag{3.57}$$

The electron number is plotted in Fig. 3.14. Due to the characteristics shown in Fig. 3.13, the number of electrons almost converges at higher velocities. Dividing the Frank-Tamm formula for electrons dN_γ/dx_e (Eq. 3.46) by the electron energy loss dE_e/dx_e (Eq. 3.26) yields the number of photons per electron energy dN_γ/dE_e. The δ-electron loses its initial kinetic energy T_e while passing through matter until it cannot produce Cherenkov light below T_0. Therefore the following integral gives the total number of photons $N_{\gamma,e}$ produced by one δ-electron[27]

$$N_{\gamma,e} = \int_{T_0}^{T_e} \frac{dN_\gamma}{dx_e} \left(\frac{dE_e}{dx_e} \right)^{-1} dE_e \tag{3.58}$$

This is drawn in Fig. 3.15 in dependence of the kinetic energy.

Finally the number of electrons in Eq. 3.52 is multiplied with the number of photons per electron Eq. 3.58 which gives the total number of Cherenkov photons per unit path length of the monopole after integrating over the kinetic energy

$$\frac{dN_\gamma}{dx} = \int_{T_0}^{T_m} \frac{d^2 N_e}{dT_e dx} \left[\int_{T_0}^{T_e} \frac{dN_\gamma}{dx_e} \left(\frac{dE_e}{dx_e} \right)^{-1} dE_e \right] dT_e \tag{3.59}$$

This is the brightness of monopole signals due to indirect Cherenkov light from δ-electrons. It is plotted for Mott and KYG cross section in Fig. 3.11 in comparison to the direct Cherenkov light of a muon and a monopole.

---

[26]The electron energy at rest is $E_0 = m_0 c^2 = 511 \, \text{keV}$.

[27]The wavelengths $\lambda_1 = 600$ and $\lambda_0 = 300 \, \text{nm}$ are used in the Frank-Tamm formula to account for the sensitive region of the IceCube's PMTs.
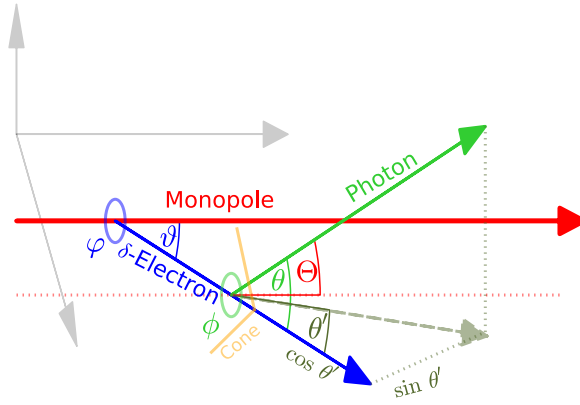
Figure 3.16: Projection (dark green) of the photon track (light green) onto the plane between monopole (red) and electron (blue). The azimuth angle ϕ rotates the photon track around the electron track. The azimuth angle φ rotates the electron track around the monopole track. When rotating around ϕ the cosinus of the projected angle θ' (dark green), does not change but the sinus.

3.3.4   Angular distribution of indirect Cherenkov light

The angular distribution of indirect Cherenkov light is derived analogous to the indirect Cherenkov light by standard model particles. The angle between the trajectories of monopole with velocity v_M and δ-electron θ_m^e is given by[28] [Oli14, vR06a]

$$\cos \vartheta_m^e \quad = \quad \frac{T_e}{p_e} \frac{p_{\max}}{T_{\max}} \tag{3.60}$$

$$\approx \quad \frac{c}{v_M} \sqrt{\frac{T_e}{T_e + 2m_e}} \tag{3.61}$$

where p_e is the momentum of the electron, and p_{max} is the momentum with the maximum possible energy transfer $T_{\max}$ given by Eq. 3.11. Also known is the Cherenkov angle of photons emitted by electrons θ_e^γ (Eq. 3.41). The regarding azimuth angle ϕ_e^γ is isotropic with the δ-electron trajectory as reference axis. The angle between the Cherenkov photons and the monopole track is then

$$\Theta_m^\gamma = \vartheta_m^e + \theta_e^{'\gamma} \tag{3.62}$$

where $\theta_e^{'\gamma}$ is defined by

$$\sin \theta_e^{'\gamma} = \sin \theta_e^\gamma \cdot \cos \phi_e^\gamma \tag{3.63}$$

thus, it is the angle θ_e^γ projected into the plane which is spanned between the direction of the monopole and the electron. Additionally it is

$$\cos \theta_e^{'\gamma} = \cos \theta_e^\gamma \tag{3.64}$$

The angles are illustrated in Fig. 3.16 and the final distribution is shown in Fig. 3.17 in comparison to the values for the direct Cherenkov light in Fig. 3.18. The addition theorem for $\cos \Theta_m^\gamma$ then gives

---

[28]Another approximation for this is given in Eq. 3.10. For easier reading the names of the angles are complemented with the indices of the particle which causes (subscript) the creation of another particle (superscript) although all names are unambiguous.
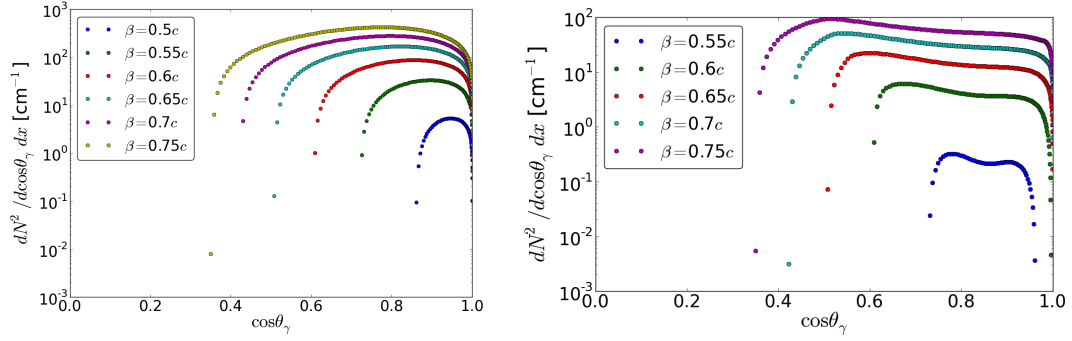
Figure 3.17: Angular distribution of indirect Cherenkov light calculated with KYG and Mott cross section (left) and Rutherford cross section (right). The difference is due to the quantum mechanical correction factor from Eq. 3.14. To calculate the distributions in Fig. 3.17, the relation $d\Omega = 2\pi \sin\theta d\theta = 2\pi\, d(\cos\theta)$ was used in Eq. 3.51.
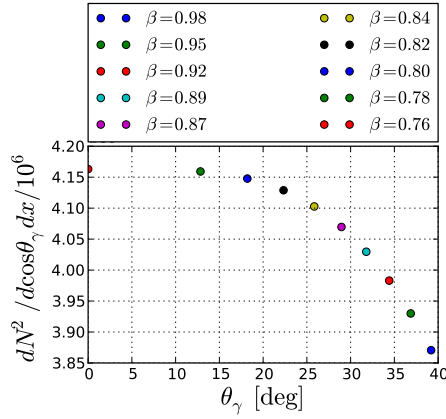
Figure 3.18: The angular distribution of direct Cherenkov light is peaked at one angle which is dependent on the velocity. To draw this plot Eq. 3.46 is written as $dN_\gamma/dx = 2\pi\alpha Z^2(\lambda_0^{-1} - \lambda_1^{-1})(1 - \cos\theta)$ and integrated to $dN_\gamma^2/dx\, d\cos\theta = 2\pi\alpha Z^2(\lambda_0^{-1} - \lambda_1^{-1})(\cos\theta - \cos^3\theta/3)$.

$$\cos\Theta_m^\gamma = -\sin\vartheta_m^e \sin\theta_e'^\gamma + \cos\vartheta_m^e \cos\theta_e'^\gamma \tag{3.65}$$

$$= -\sin\vartheta_m^e \sin\theta_e^\gamma \cdot \cos\phi_e^\gamma + \cos\vartheta_m^e \cos\theta_e^\gamma \tag{3.66}$$

The result is independent of the cross section form factor but dependent on the correction factor from Eq. 3.14.

3.3.5   Discussion

As discussed in Ch. 3.1.4, the KYG cross section is used in this analyses for the calculation of the indirect Cherenkov light. Above the Cherenkov threshold the addition from indirect Cherenkov light to the total yield is minor. However, the angular distribution is more diffuse which might change the monopole signature in IceCube. Therefore indirect Cherenkov light is used in addition to the direct Cherenkov light for velocities above the Cherenkov threshold.

4   Simulation and data processing

The properties of standard model particles are partly known from measurements and partly modeled. The features of magnetic monopoles are proposed in theory. Transferring this information into simulation technically requires the[29]

- generation of fundamental parameters (position, time, direction, velocity, energy etc.) of standard model particles, such as muons and neutrinos, as well as magnetic monopoles (see Chs. 4.1.1, 4.1.2, and 4.2.1)

- propagation of background and signal particles through the atmosphere, the Earth and the Antarctic ice, taking into account decay and interaction probabilities and propagating all secondary particles (see Chs. 4.1.3 and 4.2.2)

- generation of Cherenkov light when the background or signal particle is close to the detector (see Chs. 4.1.4 and 4.2.3)

- propagation of light through the ice (see Ch. 4.1.4)

- calculation of the response of the PMT and DOM electronics including the generation of noise hits (see Chs. 4.1.4 and 1.2.3)

- triggering (i.e. starting) the event readout if trigger conditions are fulfilled (see Ch. 4.4.1)

- filtering of events to reduce the data rate for satellite transfer (see Ch. 4.4.2)

Particle generation, propagation, and Cherenkov light production is treated differently for various particle types and is therefore described separately for background and magnetic monopoles in the next two sections. Background simulation is validated using the burn sample introduced in the third section. The subsequent processes are described for all particle types in the further sections.

4.1   Background simulation

For background simulation the particle type, energy, rate, and interaction with matter have to be measured or modeled. The applied models are shown hereafter.

---

[29]To perform all these steps, the IceCube software *IceTray* is used [DeY04]. It is a C++ framework which has a modular structure reflecting different purposes such as those listed above. In IceTray one recorded event, which is the set of all hits during a trigger window, is saved into one data container, called a frame. This analysis uses the meta-projects (a collection of modules) IceSim, version 3.2, for signal and background simulation and IceRec, version IC2011-L2_v12.08, which is required for standard processing of filters. The reconstruction described in the next chapter is done with IceRec, version 4.2.

j	R_c [V]	γ					$a_{i,j}$				
		p	He	CNO	Mg-Si	Fe	p	He	CNO	Mg-Si	Fe
1	$4 \cdot 10^{15}$	1.66	1.58	1.63	1.67	1.63	7860	3550	2200	1430	2120
2	$30 \cdot 10^{15}$	1.4					20	20	13.4	13.4	13.4
3	$2 \cdot 10^{18}$	1.4					1.7	1.7	1.14	1.14	1.14

Table 4.1: Parametrization values for Eq. 4.1. These are used to parametrize the measurements shown in Fig. 4.1. Taken from [Gai12].

4.1.1   Muons originating from air showers

The abundant flux of muons recorded by IceCube originates from interactions in cosmic ray air showers. The energy spectrum and composition of cosmic ray primaries have been measured by many experiments. These measurements are used to develop physical models explaining the shape of the energy spectrum over large energy ranges and the variation in elemental composition as a function of primary energy. One approach is to build the total spectrum out of spectra for different nuclei with a hard cutoff at different energies [Hil05b]. Additionally the spectrum is divided artificially into two distinct galactic populations (approximately above and below the knee of cosmic rays, explained in the caption of Fig. 4.1) and an extragalactic population. The spectrum of a primary nucleus i depending on its energy E_{prim} is then given by

$$\Phi_i \left(E_{\mathrm{prim}} \right) = \sum_{j=1}^{3} a_{i,j} \cdot E_{\mathrm{prim}}^{-\gamma_{i,j}} \cdot \exp \left(-\frac{E_{\mathrm{prim}}}{Z_i \cdot R_{c,j}} \right) \tag{4.1}$$

with the integral spectral index γ which is dependent on the nucleus i, the population j, and the normalization constant $a_{i,j}$. R is the magnetic rigidity and R_c is the characteristic rigidity or cutoff above which a particular acceleration process reaches its limit. The values in Tab. 4.1 are calculated to parametrize the experimental data shown in Fig. 4.1 using a mixed extragalactic composition in this model called *GaisserH3a* [Gai12]. The nuclei are divided into five elemental types with identical parametrization values.

The muon component of cosmic rays can be measured with the in-ice component of IceCube restricted to an energy interval from 10 TeV to 10 EeV. The lower energy threshold is caused by the limited penetration depth of muons through the ice. For this analysis two disjunct IceCube simulation sets are used. The first ranges between primary energies of 600 GeV to 100 TeV with a spectral index[30] of 2.6. The second is for primary energies between 100 TeV and 10^{11} GeV with a spectral index of 2.0. In this analysis the spectrum was re-weighted to the reflect GaisserH3a model[31] (see App. D.3). About 15 % of air showers are recorded nearly simultaneously by IceCube as *coincident events*. The hits recorded

---

[30]The spectral indices in the GaisserH3a model depend on population and nuclei. This is in contrast to the common spectral index which is dependent on energy.

[31]The interaction of the primary nuclei with the atmosphere and the propagation of the secondaries as an air shower through the atmosphere are calculated with the software CORSIKA (COsmic Ray Simulations for KASKADE) [Hec98]. In IceCube the SIBYLL event generator, version 2.1 [Fle94], is used within CORSIKA to describe hadronic interactions at high energies. Compared to other models it comprises of a minimum number of assumptions.
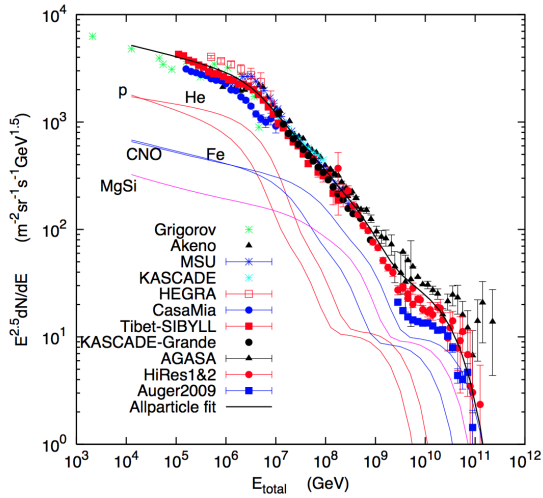
Figure 4.1: Energy spectrum of cosmic rays measured by several experiments and fitted by the GaisserH3a model. The change in slope from $E^{2.7}$ to $E^{3.1}$ at roughly 10^6 GeV is called the *knee* and the harder slope at roughly 10^{10} GeV is called the *ankle*. Taken from [Gai12, Fig. 1].
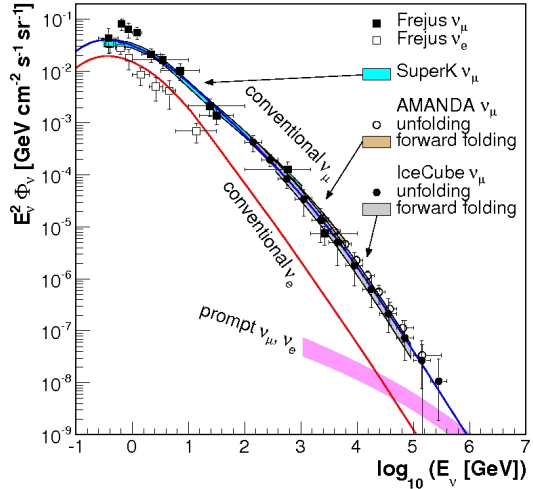
Figure 4.2: Energy spectrum of neutrinos measured by several experiments. The Honda model (thin solid lines) and Sarcevic model (bold magenta band including uncertainties) are also shown. Taken from [Sul13, Fig. 1].

in one event are not necessarily originating from the same physical event but often from several different events building a coincident event. This is also taken into account by the simulation process.

4.1.2 Neutrinos

Electron and muon neutrinos are considered as background in this analysis. Tau neutrinos have never been identified by IceCube and therefore they are not considered as a background with distinct signature. They are accounted for by the other neutrino flavors. A generic energy spectrum of E^{-2} is generated[32] to allow re-weighting to different models for various analysis purposes. The spectral index 2.0 over-samples neutrinos with higher energies in order to reduce computing time while gaining sufficient *statistics* (definition in App. D.1) at this energy level. Since the neutrino cross section is low, it is required that every neutrino interacts and the interaction probability is taken care of by weighting the event.

The conventional atmospheric neutrinos are weighted (see App. D.3) to the *Honda2006* spectrum [Hon07], which is based on *DPMJet-III* simulations [Dpm00]. This is shown in Fig. 4.2 in comparison to measurements. At high energies the dominant production mechanism is the leptonic decay of mesons comprising at least one charm quark. This is included into the background simulation using the *SarcevicStd* model which inherits a

---

[32]The IceTray module is called *NuGen*.
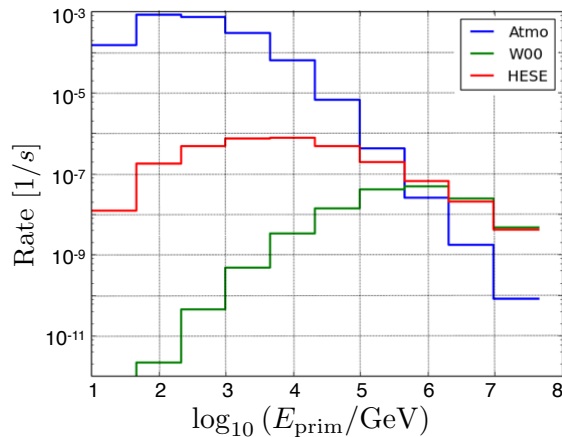
Figure 4.3:   Model of muon neutrino fluxes applied in the simulation. The atmospheric spectrum (blue) comprises of conventional and prompt neutrinos modeled with Honda2006 and SarcevicStd. The fit on recent measurements of astrophysical neutrinos (red) is compared with the latest model before the measurement (green) [Rom03] based on the Waxman-Bahcall bound [Wax00].

significant suppression of the prompt neutrino flux [Enb08]. For the calculation of uncertainties of this analysis the less recent *Bartol* [Bar04] and *NaumovRqpm* models [Fio01] are used for conventional and prompt neutrino fluxes.

Since there is evidence for the measurement of neutrinos with astrophysical origin performed with IceCube this flux has also to be considered as a background source. It is assumed that this neutrino component was an unaccounted background in the search for highly relativistic monopoles in IC40 data [Pos13a, Pol16]. The flux from the latest fit to this data, recorded between 2010 and 2013, was implemented in this analysis [Aar14c]

$$E^2\Phi(E) = 1.5 \cdot 10^{-8} \left(\frac{E}{100\,\mathrm{TeV}} \right)^{-0.3} \mathrm{GeV\,cm^{-2}\,s^{-1}\,sr^{-1}} \tag{4.2}$$

The resulting energy spectra of muon neutrino background simulation sets is shown in Fig. 4.3. The neutrino rate from every origin is much lower than the air shower rate in IceCube. Nevertheless many neutrino secondaries cross the detector at the same time as muons from air showers. By mixing a cosmic ray background into the neutrino background simulation using CORSIKA, the effect of coincident events is simulated.

4.1.3   Particle Propagation

The propagation of standard model particles reaching the deep ice is done by calculating the continuous energy loss and the probability of stochastical energy losses from pair-production, bremsstrahlung, or photo-nuclear processes[33] [Chi04, Koe13]. The develop-

---

[33]The propagation of particles is performed using the IceTray module *MMC*. Cascades are simulated with *CMC*. The physical effects along a particle track or the secondaries of a cascade are saved in an IceTray data container, called *I3MCTree*. The abbreviation *I3* means IceCube. The acronym *MC* stands for *Monte Carlo* simulation. This is a stochastical method to obtain numerical results by doing random experiments.

ment of electromagnetic and hadronic cascades caused by electron neutrinos or stochastical energy losses of muons is also handled.

4.1.4   Light generation and propagation

The software package *Photonics* [Lun07], which tracks photons through matter, was replaced as the standard module for simulations by *PPC* (Photon Propagation Code) [Aar13b] during the development of this analysis. Photonics generates 6-dimensional tables (3 spatial, 2 directional, and 1 temporal) which are used in a subsequent step to retrieve the probability of a photon to hit a certain DOM. At least one set of tables has to be created per particle type and velocity. This requires constant particle velocities and large disk storage for the tables. The binning of the tables can have a noticeable effect on the calculated light output of low energetic particles.

For this purpose the module *CLSim* provides access to the simulation software *GEANT* (GEometry And Tracking) [All06] which propagates each photon individually through the ice. GEANT is currently used for analyses of low energetic events in IceCube or air shower secondaries in IceTop. The disadvantage of this software is long processing time for bright events. A compromise is PPC, which is used for the background and monopole simulation in this analysis, because it uses parameterizations of GEANT simulations to accelerate the processing. The photon generation and propagation in PPC is described in detail in this section in order to have a base for the description of the adjustments for monopole simulation. It was originally developed to calculate the parameters for ice models describing the IceCube detection medium. These parameters are based on measurements with artificial lights deployed in the DOMs. The software is built to run on GPUs (Graphics Processing Unit) as well as on CPUs (Central Processing Unit) because GPUs reduce the processing time needed by CPUs by a factor of 100.

PPC reads all particles produced by the propagator, described in the previous section, and treats them according to their type. The light output of different particles was simulated using GEANT and afterwards parametrized for use in PPC [Rae12a]. The created photons are propagated through ice, using a user-defined ice-model as input, until they reach a DOM or are absorbed. To decrease calculation time the DOM size is scaled up by a factor of $f = 5$ to 16, which increases the DOM area quadratically whereas the number of emitted photons is scaled down by a factor of f^2 [Aar13b].

Prior to this analysis only track signatures from muons were implemented into PPC. The other implemented signatures are cascades from various origins. The number of photons produced from Cherenkov light can be calculated directly using the Frank-Tamm Eq. 3.46 integrating from 300 to 600 nm wavelengths to account for the DOM acceptance. The number of photons per meter from a bare[34] muon is approximately $dN_\gamma/dx_\mu = 30000$ for $v_\mu = c$. The photon number is reduced while traversing the glass and gel of the DOM and because of the PMT's quantum and collection efficiencies (Fig. 1.6). This is handled using the wavelength dependent DOM acceptance $d\rho_{\text{DOM}}/d\lambda$ which is the fraction

---

[34]A relativistic muon produces δ-electrons and undergoes stochastical energy losses which are not taken into account when speaking of a *bare* muon.
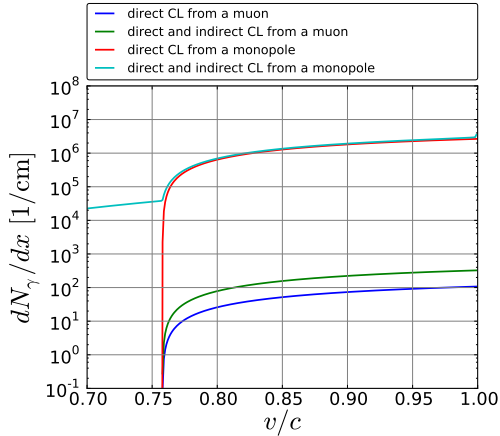
Figure 4.4: Light yield of a bare muon, a muon accompanied by δ-electrons (using Eq. 4.5), a bare monopole, and a monopole producing indirect Cherenkov light (calculated with the KYG cross section).
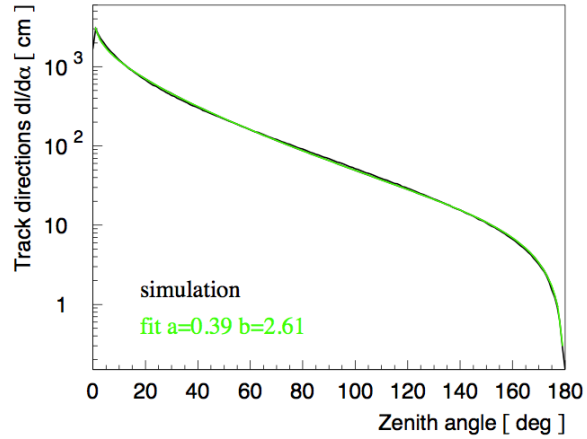
Figure 4.5: Angular distribution of $100\,\text{GeV}$ electron cascades simulated (black) and fitted (green) according to Eq. 4.7. Taken from [Aar13b].

of incident photons onto the cross section of a DOM that causes a signal in the PMT. The measurement of the IceCube DOM acceptance is shown in Fig. 1.6. The (non-integrated) Frank Tamm Formula $d^2N_\gamma/dx_\mu d\lambda$ is convolved with the DOM acceptance to get the final photon number

$$\frac{dN_{\gamma,f}}{dx_\mu} = \int_\lambda \frac{d^2N_\gamma}{dx_\mu d\lambda} \cdot \frac{d\rho_{\text{DOM}}}{d\lambda}\, d\lambda \tag{4.3}$$

This gives about $dN_{\gamma,f}/dx_\mu = 2450$ photons per meter of track length which is only $8\,\%$ of the previous value for muons. The wavelength dependence is shown in Fig. 1.6. This value for the light yield of a bare muon is hard coded in PPC. This is used to get the number of photons which need to be propagated in the CPU part of PPC which prepares the photon propagation in the GPU part.

Since the muon is also accompanied by δ-electrons the non-bare muon emits more light than the bare muon. Up to a δ-electron energy of $0.5\,\text{GeV}$ the contribution of Cherenkov light due to δ-electrons is uncorrelated and randomly distributed along the length of the track. The additional light yield by δ-electrons and all other secondaries is taken into account by scaling the track length of the particle l to the effective track length $\hat{l}$ [Rae12b]

$$\hat{l} = l \cdot \frac{\sin^2\theta}{\sin^2\theta_{\beta=1}} \quad \text{with} \ \sin^2\theta = 1 - \frac{1}{\beta^2 n_p^2} \tag{4.4}$$

with the Cherenkov angle θ, the velocity β in units of c and the refraction index of ice n_p. The value $\hat{l}$ corresponds to the equivalent length of a relativistic track with the same photon yield as the track length l. The following equations are implemented into PPC depending on the particle energy. For muons it is [Aar13b]

$$d\hat{l} = dl \cdot (1.188 + 0.0206 \cdot \log_e E\,[\text{GeV}]) \tag{4.5}$$

and for electromagnetic cascades it is

$$d\hat{l} = 5.21 \frac{\mathrm{m}}{\mathrm{GeV}} \cdot \frac{0.924}{\rho} \cdot E \,[\mathrm{GeV}] \tag{4.6}$$

The increasing light yield of non-bare muons is also shown in Fig. 4.4. These values were originally derived for water, and they are updated for the density ratio of ice to water $\rho = 0.9216$ as it is used in PPC to scale up the photon number $dN_{\gamma,f}/dx_\mu$.

The angular distribution of the δ-electrons, plotted in Fig. 4.5, is also parametrized using the track length l giving [Aar13b]

$$\frac{dl}{dx} = \exp(-b \cdot x^a) \cdot x^{a-1} \text{ with } x = 1 - \cos\theta \tag{4.7}$$

with values $a = 0.39$ and $b = 2.61$ which are constant with energy. This was fitted on the simulation output of $100\,\mathrm{GeV}$ electron cascades. It is also valid for electromagnetic and hadronic cascades (independent of the incident particle) down to a few MeV [Rae12b].

To use this in PPC one needs to generate angles as random numbers with the function dl/dx as a probability distribution. See App. D.2 for the mathematical base. Using the normalized cumulative distribution function [Rae12b]

$$f(x) = \frac{\int_0^t \frac{dl}{dx'} dx'}{\int_0^1 \frac{dl}{dx'} dx'} \tag{4.8}$$

and $x = 1 - t$ with $t = \cos\theta$ one gets

$$f^{-1}(x) = 1 - \left[-\frac{\log_e(1 - x \cdot (1 - e^{-b \cdot 2^a}))}{b} \right]^{\frac{1}{a}} \tag{4.9}$$

In the GPU part of PPC, where the photons are propagated through the ice, the photon angle is sampled with the help of this function.

The response of the detector is simulated for all components and is independent of the particle type producing the light. After the light has passed through the bulk ice, hole ice, glass, and gel of the DOM it hits the PMT.

The next step in simulation is subsequent processing by triggers and filters which is described in Ch. 4.4. These processes are the same for background and monopole simulations. Therefore, the differing parts of monopole simulations are described first.

4.2   Signal simulation

The theoretical parameter space of magnetic monopoles according to mass and kinetic energy at Earth's surface is too large to produce appropriate simulation sets, as discussed before. Therefore, IceCube analyses, searching for magnetic monopoles, usually concentrate on one detection signature or signal topology in the detector. The particles are given an arbitrary mass of 10^{11} GeV without limiting generality because the signal topology is
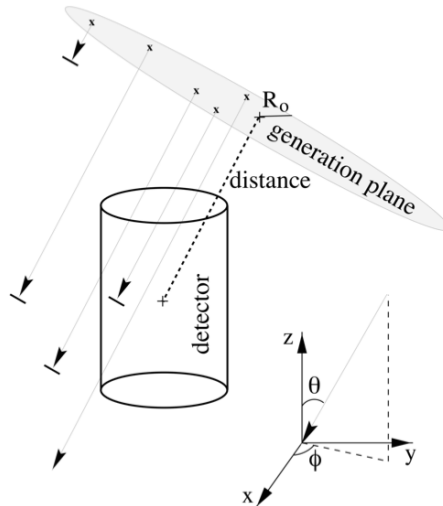
Figure 4.6: Generation of monopole tracks: The starting point of each track is sampled from generation disk of radius 850 m at a constant distance of 1000 m from the detector center. Taken from [Wie98].

independent of mass for constant velocities. A flux of $10^{-16}\,\text{cm}^{-2}\text{s}^{-1}\text{sr}^{-1}$ is assumed which is roughly the best previous flux limit from ANTARES analyses in the lower velocity range [AM12].

This analysis focuses on magnetic monopoles below the Cherenkov threshold of $0.76\,c$ where they produce indirect Cherenkov light (see Ch. 3.3.3). The light detection capability of IceCube ends at a monopole speed of about $0.45\,c$. Therefore, $0.4\,c$ is taken as the lower simulation limit. To keep the option of exceeding previous limits slightly above the Cherenkov threshold the upper simulation limit was extended to $0.99\,c$ where stochastical energy losses, such as bremsstrahlung, pair production, and photo-nuclear processes, do not occur.

Signal simulation uses the same software framework as background simulation with different modules to account for the differences in particle types. The monopole software modules were developed and improved during previous analyses for relativistic and non-relativistic monopoles [Glu10, Chr11, Pos13a]. The latest software versions developed for this analysis, unite the requirements of all purposes.

4.2.1   Monopole Generation

The goal of this step is an isotropic distribution of tracks through the detector[35]. For that, a generation disk with radius 850 m is randomly positioned at a distance of 1000 m around the detector. This is illustrated in Fig. 4.6. The optimal parameters for distance

---

[35]The *monopole-generator* is the IceTray module which calculates and samples the starting point, direction, and velocity of magnetic monopoles. The monopole-generator module saves the user defined parameters and randomized numbers into the frame in which the particle is stored. These are mass, velocity, disk radius and distance, weight, zenith angle and azimuth angle. In addition it calculates the sum of all weights which is used for normalization.
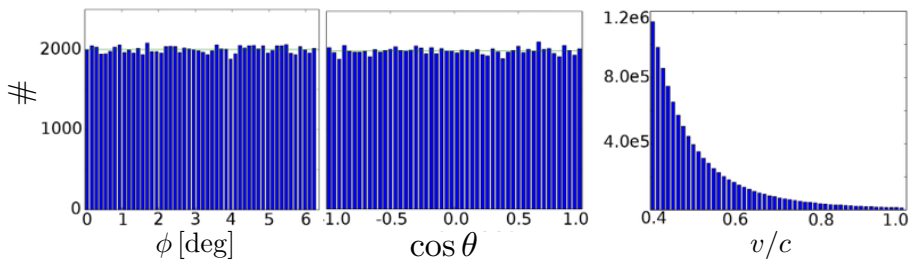
Figure 4.7: Monopole simulation showing a uniform distribution in azimuth (left) and zenith angle (middle). See App. D.4 for the explanation the angular distributions are drawn in this way. Simulation of a β^{-5} power law for the velocity distribution (right). When the weights are applied the velocity distribution is uniform, however statistics (definition in App. D.1) are two orders of magnitude higher for $v = 0.4\,c$ than for $v = 0.99\,c$.

and radius were derived in a previous IceCube analysis [Chr11], based on the coverage of the entire detector and fast processing time. The direction of the monopole track is perpendicular to the disk. The starting point of the particle is sampled on the plane. The resulting angular distributions are plotted in Fig. 4.7. They are uniform as expected.

This work takes advantage of software advances, such as GPU processing, which enables simulation of a velocity distribution instead of few fixed velocity values. A uniform distribution would lead to insufficient statistics at lower velocities, therefore the software is modified to enable the choice of a power law $\beta^{-\gamma}$. For the technical implementation see App. D.2. The choice of a velocity distribution instead of particular velocities can be misleading since only one characteristic velocity is expected for monopoles of a certain mass and direction. This has to be considered when interpreting the final results.

Ten million monopole events were simulated with a power law of β^{-5} and re-weighted to a uniform distribution, see Fig. 4.7. This gives about ten thousand events at the highest velocity $0.99\,c$ and several million at lowest velocity $0.4\,c$ which proved to be sufficient statistics.

4.2.2 Monopole Propagation

The propagation is done by determining the distance from the current position in which a monopole loses $0.1\,\%$ of its kinetic energy by collisional losses using Eq. 3.34[36]. Thus, segments of the monopole track are created of which the lengths are restricted between $0.001\,\text{m}$ and $10\,\text{m}$. The propagation is stopped $1400\,\text{m}$ away from the center of the detector or when the velocity drops below $0.2\,c$. Due to the chosen mass for the simulated monopoles (Ch. 2.5), the simulated events do not lose sufficient energy to change their velocity significantly.

---

[36]The *monopole-propagator* module reads the values stored by the monopole-generator into the I3MCTree container. The *monopole-propagator* stores the track segment and its initial velocity into the I3MCTree container.
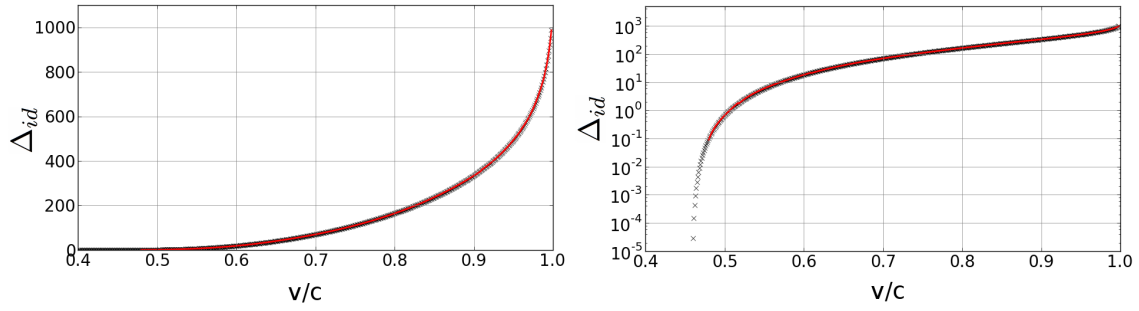
Figure 4.8: Fit (red line) of exact calculation of the light yield of δ-electrons accompanying a monopole using the KYG cross section (black crosses) divided by the light yield of a bare muon with $\beta = 1$. Fit values for the Eq. 4.13 are in Tab. 4.2.

4.2.3 Light simulation

As described in Ch. 4.1.4 the module PPC is used for light generation and propagation. It reads the particles and their track segments and processes them according to their type. In PPC the light yield per path length is assumed to be constant for all energies. To account for the additional light from δ-electrons and radiative losses, the track length is adjusted to an effective track length which is accordingly longer as explained in Ch. 4.1.4. The magnetic monopole type was implemented as a second track-like signature in addition to the muon signature. Since all parameters and functions in PPC rely on the features of a bare muons, all monopole parameters were implemented as an additional adjustment of the effective muon track length. The ratio Δl is wavelength independent which simplifies the calculation regarding Eq. 4.3 convoluting the DOM acceptance with the Frank-Tamm formula

$$\Delta l_d(\beta) = \frac{\left(\frac{d^2 N}{dx d\lambda}\right)_M}{\left(\frac{d^2 N_{\beta=1}}{dx d\lambda}\right)_\mu} = \frac{\left(\frac{dN}{dx}\right)_M}{\left(\frac{dN_{\beta=1}}{dx}\right)_\mu} \tag{4.10}$$

For direct Cherenkov light Δl_d Eqs. 3.46, 3.49, and 3.41 are used

$$\Delta l_d \quad (\beta) = \frac{\left(\frac{d^2 N}{dx d\lambda}\right)_M}{\left(\frac{d^2 N_{\beta=1}}{dx d\lambda}\right)_\mu} = \left(\frac{gn}{Ze}\right)^2 \frac{\left(1 - \frac{1}{\beta_M^2 n_{ice}^2}\right)}{\left(1 - \frac{1}{n_{ice}^2}\right)} = \left(\frac{gn}{Ze}\right)^2 \frac{\sin^2 \theta_M}{\sin^2 \theta_{\beta=1}} \tag{4.11}$$

$$\Rightarrow \Delta l_d \quad (\beta) \approx \frac{624464828.676 \cdot \left(1 - \frac{1}{1.741 \cdot \beta^2}\right)}{32359.138} \tag{4.12}$$

This is illustrated in Fig. 4.8. For indirect Cherenkov light Δl_{id} Eq. 3.59 in combination with the KYG cross section (Eq. 3.52) is used and divided by the hard coded muon light yield. The resulting distribution is fitted with six functions of the following form to decrease processing time

$$\Delta l_{id}(\beta) = a \cdot e^{b \cdot \beta + c} + d \tag{4.13}$$

where a, b, c, and d are fit parameters given in Tab. 4.2. Both Δl_d and Δl_{id} are then normalized to the track length, described in Ch. 4.2.2, and the photon yield of a bare muon with $\beta = 1$. In addition they are reduced by the PPC value for DOM efficiency.

β-range $[c]$	a $[\frac{1}{\text{cm}}]$	b $[\frac{1}{c}]$	c	d $[\frac{1}{\text{cm}}]$
< 0.51	$1.15 \cdot 10^{-10}$	48.53	-1.46	0.26
< 0.61	$5.06 \cdot 10^{-3}$	14.79	-0.42	-5.30
< 0.91	0.70	5.86	1.02	-48.55
< 0.96	$4.66 \cdot 10^{-4}$	13.70	0.42	$1.77 \cdot 10^{2}$
< 0.99	$2.99 \cdot 10^{-13}$	35.08	$6.13 \cdot 10^{-2}$	$4.08 \cdot 10^{2}$
≥ 0.99	$9.14 \cdot 10^{-49}$	$1.17 \cdot 10^{2}$	-0.25	$6.76 \cdot 10^{2}$

Table 4.2: Fit values of the light yield of δ-electrons using Eq. 4.13. The lower limit of the β-range is the value in the previous row apart from the first row where it is technically zero and physically about $0.45\,c$. The first term in the equation is strongly suppressed by the small value of a in three cases. The fit is plotted in Fig. 4.8.

The angular distribution of the direct Cherenkov photons of a monopole is adjusted to account for the changing velocity by implementing Eq. 3.41. To do that the internal PPC container for particle parameters is changed to store the particle velocity and type. Since the energy range of δ-electrons produced by a monopole is between $271.8\,\text{keV}$ and $0.511\,\text{GeV}$ the parametrization of the muon case is valid here, too. In addition the angular distribution of photons in IceCube is smeared out by the strong scattering in ice. Therefore the angular distribution of photons produced by δ-electrons is adopted from the muon case because no measurable difference is expected.

Due to the many changes in monopole simulation, checks have been performed after applying the detector response simulation, described in Ch. 4.1.4, comparing the old and new modules, especially Photonics and PPC. No significant changes in the distributions of reconstructed variables have been found apart from differences expected because of the non-avoidable usage of different ice-models.

4.3 Burn sample

The burn sample of IC86-1 analyses usually consists of every tenth run defined by a run-number ending in zero. This sums up to a livetime of about 31 days. The livetime is the recording time for clean data. The rate varies with season due to the different conditions in the atmosphere.

The burned data is used to validate the background simulation and reconstruction. In addition, Monte Carlo simulation consistency to data ensures the robustness of reconstructed variables regarding differences in data and simulation.

Due to technical reasons only small air shower simulation sets were produced for the first year of the IC86 configuration. Since all the sets are weighted to get more high energetic events (see App. D.3), low energetic events in particular have insufficient statistics. This can be compensated, up to a certain point, by checking the rates with the burn sample. The treatment of low energetic air shower events is described in Ch. 5.4.

4.4   Standard processing

The IceCube processing scheme of recorded data is organized in levels which will be described in this and the following chapter

Level 0: application of triggers

Level 1: online base processing and application of filters; offline re-processing

Level 2: processing and reconstructions specialized for different event types

Level 3: reconstructions and quality cuts specialized for different physics cases

Apart from level 2, all levels reduce the amount of data drastically by discarding events which are most likely not needed by analyzers. With increasing level the processing gets more specific to the considered physics case. The standard IceCube simulation follows this scheme. Most IceCube analyses can use the provided data and simulation which is processed up to level 3. Analyses searching for rare event types use level 2 data and create their own level 3, such as it is done in this analysis. For consistency the level nomenclature is used in this text.

4.4.1   Trigger

When light is recorded by the DOMs and the HLC condition, described in Ch. 1.2.3, is fulfilled, IceCube's data acquisition system is notified. The software driven trigger system checks if a trigger condition is fulfilled. Every year, these triggers are adjusted for different IceCube configurations and to account for software improvements. The documentation is mainly the program code, therefore they are explained in this work. The IceCube triggers working on standard strings (apart from DeepCore strings) which are considered in this analysis are

Simple multiplicity trigger (SMT8): At least 8 DOMLaunches are recorded within a time window of 5000 ns.

String or cluster trigger: At least 5 DOMs out of a series of 7 DOMs are hit on one string within a time window of 1500 ns. Events that have hits in the top 2 DOM layers are vetoed. The trigger is designed to capture low energy muon neutrinos with energies below those detectable by the SMT8 trigger.

Cylinder or volume trigger: If the condition of a simple multiplicity trigger with 4 hits (SMT4) is fulfilled, a cylinder is spanned around this point, ranging of each the half of 75 m (4 DOMs) up and down, with a radius of 175 m (1 string) to all sides. Altogether this cylinder comprises of 4 strings times 5 DOMs around the SMT4 triggered hit. The trigger condition is fulfilled if 8 hits are recorded within 1000 ns in this cylinder. The trigger is designed to capture low energy horizontal events.

If at least one trigger condition is fulfilled, all hits within a trigger window of up to $10\,\mu s$ will be recorded and combined to one event. There is no special trigger concerning monopoles with the considered velocity range because the SMT8 trigger is fulfilled due to the long time window. The recorded events are combined to runs which last up to eight hours.

4.4.2   Online processing and filter

The recorded events are sent to server farms in the northern hemisphere via a satellite connection with restricted bandwidth. Thus, there are filters implemented after triggering to reduce the event rate further and extract interesting events. Such as the triggers, they are adjusted every year accounting for changes in bandwidth and physics requirements. The filters chosen for this analysis are described in the following.

Online level 1:   The base processing prepares data for the filters and comprises of

1. removing the hits of DOMs with known issues

2. applying calibration constants, which correct known effects of the electronics, to transform the contents of raw DOMLaunches into waveforms (this might differ for recorded data and simulated events)

3. analyzing the waveform to reconstruct the number and arrival times of photons which hit the DOMs

4. cleaning of SLC caused probably by noise hits using a time-window of $1000\,\mathrm{ns}$ and radius of $150\,\mathrm{m}$ around HLC hits (so called *RT-condition*): first all HLC hits are identified and used as seeds to check if they fulfill the RT-condition themselves, then the SLC hits are retained which fulfill the RT condition regarding a seeding HLC hit (SRT cleaning)

5. cleaning of hits using a sliding time window of $6000\,\mathrm{ns}$: all hits within the $6000\,\mathrm{ns}$ window containing the most hits are kept (TW cleaning)

(SDST) Muon filter: This filter is designed to select particle signals from muon-neutrino interactions which show a track-like signature with preference of up-going events. This means events which develop in time from the deeper layers of the detector to higher layers. Based on the level 1 processing the filter does a

- reconstruction using *LineFit*: a 4-dimensional (position plus time) least-squares fit which yields an estimated direction and velocity for an event

- cut on the number of hit DOMs n_{DOM} dependent on the LineFit's zenith angle θ_{LF}. This cut is harder for down-going events, to reduce the data rate prior to the time consuming Likelihood fit

$$n_{DOM} \geq \begin{cases} 8 & \text{for } \theta_{LF} > 70° \\ 10 & \text{for } \theta_{LF} \leq 70° \end{cases} \tag{4.14}$$

- simple Likelihood fit based on the first photons arriving at a DOM which are expected not to be scattered (SPE1st)

- cut on the the Likelihood L and number of reconstructed photons summed over all DOMs n_{NPE} optimized in three different zenith θ_{SPE1st} regions

$$\frac{\log_e L_{\mathrm{SPE1st}}}{n_{\mathrm{DOM}} - 3} \leq 8.7 \text{ for } \theta_{\mathrm{SPE1st}} \geq 78.5° \tag{4.15}$$

$$\frac{\log_{10} n_{\mathrm{NPE}} - 2.6}{\cos\theta_{\mathrm{SPE1st}} - 0.5} \geq 3.9 \text{ for } 60° < \theta_{\mathrm{SPE1st}} < 78.5° \tag{4.16}$$

$$\frac{\log_{10} n_{\mathrm{NPE}} - 2.6}{\cos\theta_{\mathrm{SPE1st}} - 0.5} \geq 0.6 \text{ for } \theta_{\mathrm{SPE1st}} \leq 60° \tag{4.17}$$

The events retained after all cuts are saved in the Super Data Storage and Transfer (SDST) format. This is a compressed data storage format which enables saving of more events into one file with a small size. In addition the standard (non-SDST) muon filter is also kept with the addition of the cut $n_{DOM} \geq 18$ applied first to reduce the data rate for the non-SDST data.

EHE filter: The EHE filter retains events with $n_{\mathrm{NPE}} \geq 1000$ reconstructed photo-electrons summed over all DOMs. This provides a filter stream containing extremely bright events.

LowUp filter: This filter is designed to retain up-going events with a reconstructed angle of $> 80°$ and a low number of NPEs. It uses the fit from the muon filter if available or a Likelihood Fit based on a less restricted number of hits. If both fits are not converging it uses a LineFit. Then the following cuts are applied

- $n_{\mathrm{DOM}} > 4$; the number of hit DOMs

- $\theta_{\mathrm{LF}} > 80°$; the zenith angle reconstructed with LineFit

- $z_{\mathrm{Travel}} \geq -10\,\mathrm{m}$; this is the average penetration depth of hits defined from below

$$z_{\mathrm{Travel}} = \langle z_{\mathrm{DOM}} - \langle Q_{0.25}(z_{\mathrm{DOM}}) \rangle \rangle \tag{4.18}$$

where z_{DOM} is the z position of a DOM and $Q_{0.25}$ are the DOMs from the earliest quantile of hits

- $\Delta t = t_{\max} - t_{\min} < 4000\,\mathrm{ns}$; The time extension (the maximal time of all pulses minus the minimal time of all pulses) is less than $4000\,\mathrm{ns}$

- $\Delta z = z_{\max} - z_{\min} < 600\,\mathrm{m}$; The height extension (the maximal z position z_{DOM} of all hits minus the minimal z_{DOM} of all hits) is less than $600\,\mathrm{m}$

- $z_{\min} < 440\,\mathrm{m}$; this is the minimal z_{DOM} of all hits

The Muon filter was chosen because it retains most track like signatures. The LowUp filter focuses on up-going tracks as this analysis does. Since some monopole signatures are very bright, the EHE filter was chosen to retain them.

4.4.3 Offline processing

After the filtered events have been sent to the northern server farm they are de-compressed[37]. Not all information is sent, so the online level 1 base processing, described in Ch. 4.4.2, is repeated as offline level 1. [38]

The offline level 2 reconstructions are then applied. These were proposed by working groups in IceCube focussing on different event types. In both offline level 1 and 2 no cuts are applied. Data and simulation provided to analyzers are at least at offline level 2. The working groups apply further reconstructions and cuts to reduce the data rate at level 3.

The physics topic of this analysis is not covered by any level 2 or 3 stream but the event signature can pass some filters. Therefore this analysis starts using offline level 2 background simulation, signal simulation, and burn sample data, which passed the EHE, Muon, and LowUp filters. A customized level 3 stream was developed, described in Ch. 5.1.

4.5 Discussion

Simulation is the technical implementation of the theories presented in the previous chapters. Thus, the monopole signature in IceCube can now be visualized in an event viewer and compared with signatures of standard model particles.

In simulation, monopoles produce a track which traverses the whole detector with a constant velocity. The light emission is dependent on speed and therefore constant along the track. For monopole speeds below $0.5\,c$ the light emission is not sufficient to be detected with the current detector hardware and software. An event view of the monopole signature is illustrated in Fig. 4.9.

The signature of a muon bundle from an air shower, see Fig. 4.10, can be described as a downward going track incoming with the speed of light. The track might end inside the detector. Stochastical energy losses of muons, causing cascades, result in a nearly symmetric outburst of light. If two air showers happen at almost the same time, the signatures could be hard to distinguish from each other.

Muon-neutrino signatures can be tracks from all directions which start in, stop in, or pass through the detector comprising of somewhat distinct cascades. Electron-neutrinos have a cascade signature. The light emission of track and cascade depends on the neutrino energy. Tau-neutrinos, which are not considered in this analysis, should cause two cascades with a track in between. The track might be so short that the cascades appear to be a single outburst of light or so long that one of the cascades are outside the range of the detector.

Concluding, the monopole signature is distinguishable from general background signatures. The direction, amount and constance of light emission can be used for separation. Since

---

[37]There is also online level 2 processing comprising further reconstructions which are used for stability checks and real time analyses at Pole.

[38]The resulting *PulseSeries*, a container to store all pulses and their times, is used in this analysis. It is called TWSRTOfflinePulses in the IC86-1 processing from the time window cleaning (TW) and the seeded radius time cleaning (SRT) which were done offline to get those pulses.

all tracks caused by background particles have the speed of light, it is a benefit that this analysis focuses on velocities below three quarters the velocity of light. Therefore the velocity of a track signature is the key variable to identify a monopole, assuming there are no other exotic particles, which might be detected by IceCube with mildly relativistic velocities. However, coincident events and other event types, that will be discussed in the next chapter, can mimic a monopole signature at first glance.
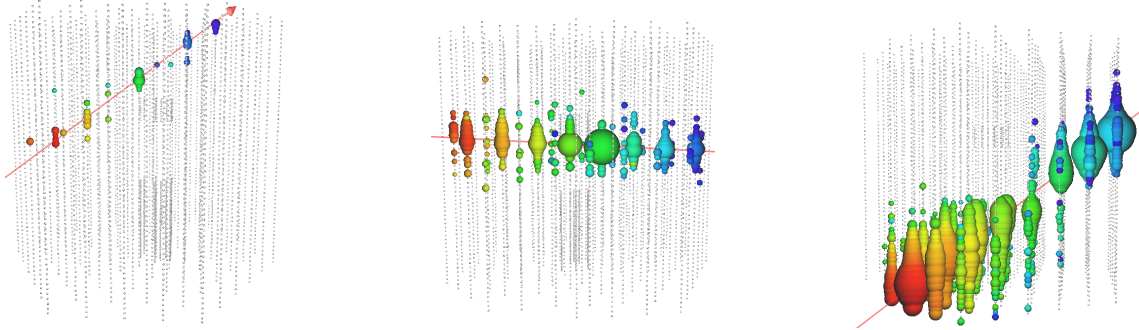
Figure 4.9: Event view of simulated monopoles with velocities $0.54\,c$ (left), $0.66\,c$ (middle), and $0.97\,c$ (right). All events develop from left to right in time (red to blue). The position of the IceCube DOMs are shown with gray spheres. Hit DOMs are visualized with colored spheres, scaling with n_{NPE}. The scaling factor is consistent through all figures in this work. The red line shows the reconstructed track which agrees with the true direction. The increased scattering in the dust layer causes the missing hits in the third displayed events (right). A low energetic muon from a muon-neutrino interaction differs from a low relativistic monopole (left) by velocity only.
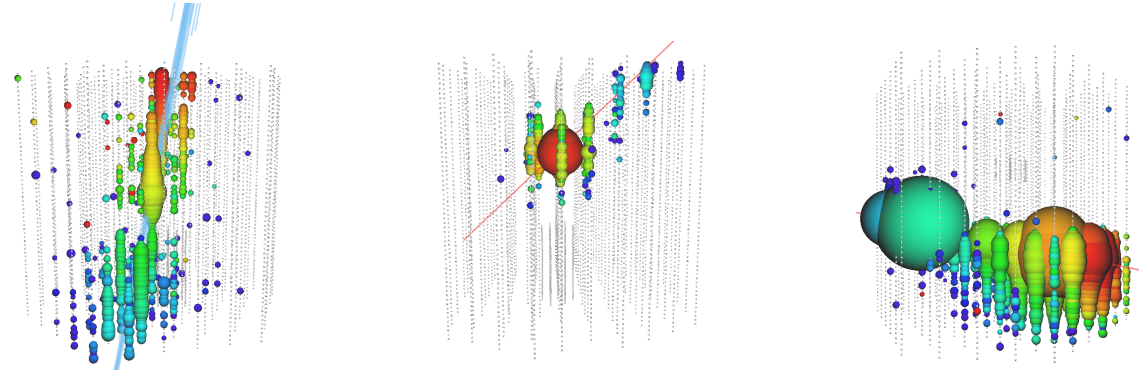
Figure 4.10: Event view of a simulated muon bundle (left) and muons from muon-neutrino interactions (middle and right). The signature of the neutrino secondary (middle) comprises of a cascade developing from near the red colored DOM. Such cascades may also occur within a muon bundle signature but never in a monopole signature of the considered speeds. The energy range of neutrino background after the last cut in this analysis, which includes this event, reaches from $3.3 \cdot 10^2\,\mathrm{GeV}$ to $2.6 \cdot 10^4\,\mathrm{GeV}$. The event on the right was found in IceCube data of season 2014 and is supposed to be the secondary of a muon-neutrino interaction [Rae15]. The deposited energy inside the detector is about $2.6 \pm 0.3\,\mathrm{PeV}$. Therefore this is the highest energetic muon-neutrino measured with IceCube to date. See App. B for a check if this event could be caused by a monopole.

5   Event selection

This chapter describes how monopole signatures can be distinguished from background signatures in IceCube. This is done by reconstructing physical variables, such as velocity and direction, as well as calculating variables describing different aspects of the measurement, such as the number of hit DOMs and others. To enhance the result of those calculations, the measured and simulated events are processed further, for example coincident events are identified and split. In IceCube's nomenclature this is called level 3 processing specialized for mildly relativistic magnetic monopoles, described in the first part of this chapter.

Hereafter, the variables are used to select monopole signatures among the events. Usually this step is distinct from statistical analysis. Due to an insufficient amount of background simulation for this standard procedure, those two steps are combined and presented jointly in the second section. In the subsequent section the uncertainties are analyzed. Finally, the sensitivity of this analysis is calculated.

5.1   Processing and reconstruction

The monopole level 3 processing was specifically developed and performed for this analysis. Despite the uncommon signature of a monopole in IceCube, it was possible to use standard processing and reconstruction tools. However, sometimes the tools are used with inverse purpose compared to their common usage since the monopole signature is so different from the standard background signatures[39].

5.1.1   Monopole processing

To get meaningful variables in the next step, the recorded and simulated events need to be processed further. The according data rates are shown in Tab. 5.1.

Event splitting
Initially coincident events are split into their probable components[40]. The algorithm searches for hits which are causally connected with at least $N = 4$ early pulses within a time window $T = 4000\,\text{ns}$. This results in several clusters of hits for which the causal connection is also checked. The hits are required to be within a horizontal distance of $d_{xy} = 500\,\text{m}$. When the hits are on the same string, they are required to be separated at most by $d_{\text{DOM}} = 30$ DOMs. The travel time between a pair of hits may deviate from the speed of light by $\Delta t = 1000\,\text{ns}$. Causally connected clusters are merged into one sub-event.

About $12\,\%$ of all events are split into two or more sub-events using the described default module parameters. This does not comprise all coincident events since the parameters are chosen in a way that monopole signatures are not split. The remaining coincident events can be reduced using cuts on suitable variables which are described below.

---

[39]As an example the variable *event time length t* (see Tab. 5.3) is usually used to keep short events and to get rid of coincident or noise events. The simulated monopole events in this analysis usually have a time length of more than 3000 ns, therefore shorter events are cut.

[40]The IceTray module is called TopologicalSplitter.

Process	Data Rate [Hz]	Description	Motivation
Filters	67.0	Muon filter, EHE filter, LowUp filter	Reduce data rate for satellite transfer
Splitter	75.2	See text	Split coincident events
After-pulse removal	66.6	See text	Discard split events which are caused by after-pulses
DeepCore hits removal	66.6	See text	More homogeneous geometry of DOMs

Table 5.1: Event rates for the processing steps. The rate is dominated by the events which pass the LowUp filter. The elimination of DeepCore hits does not change the rate.

PMT after-pulses

The algorithm, described above, often splits PMT after-pulses, explained in the caption of Fig. 1.7, into sub-events since they occur in average more than 6000 ns later than the pulses which cause them. Since the time of after-pulse occurrence is random the sub-event reflects the geometry but not the temporal evolution of the original pulses. Therefore it is possible that a down-going high energy muon bundle produces a down-going track-like signature in IceCube which is split into a down-going track and a sub-event in which the after-pulses have an up-going time development by chance. Therefore a module is written for this analysis which discards sub-events containing after-pulses using the knowledge about their signature. All sub-events which fulfill all of the following conditions are discarded. These are about 11 % of the sub-events.

- The event is split into at least two sub-events.

- The after-pulses occur in the same DOMs as the original pulses: all hits, which are in the same DOM, both in the sub-event and the non-split event, contribute to the local match fraction n_i. The fraction divided by the total number of hit DOMs in the sub-event n_{DOM}^i must exceed 0.75

$$\frac{n_i}{n_{\mathrm{DOM}}^i} > 0.75 \tag{5.1}$$

- The after-pulses cause only a minor charge in the DOM: the charge n_{NPE}^i of all hits in the sub-event i divided by the total charge in the non-split event $N_{\mathrm{NPE}} = \sum_i n_{\mathrm{NPE}}^i$ is below 0.1

$$\frac{n_{\mathrm{NPE}}^i}{N_{\mathrm{NPE}}} < 0.1 \tag{5.2}$$

- The after-pulses occur significantly later than the original hits: the difference of the mean time of hits in the sub-event $\bar{t}_i$ and the mean time of all hits $\bar{T}$ is above 3000 ns

$$\bar{t}_i - \bar{T} > 3000 \, \mathrm{ns} \tag{5.3}$$

DeepCore hits

Most of the reconstructed variables in the next section are dependent on the geometry of IceCube which is mostly evenly spaced. The exception are the six DeepCore strings which consist of DOMs with higher quantum efficiency and have a denser instrumentation than the rest of IceCube's DOMs. If the same tracks hit these DeepCore strings compared to the rest of IceCube at the same depth, they would produce different signatures in the detector. Therefore all hits on these strings are removed to achieve better reconstruction quality.

5.1.2 Reconstruction

IceCube events are measured in three dimensions which are the position of the DOMs, the time at which they recorded a hit, and the current measured by the PMT. From these informations, a large number of variables is calculated which describe particular aspects of an event signature.

The track reconstruction is based on a 4-dimensional least-squares fit taking the positions and times of hit DOMs into account. This assumes that the recorded photons originated from a plane wave instead from a Cherenkov cone. Since the emission direction of indirect Cherenkov light is more diffuse and the photons undergo large scattering in ice, this algorithm is sufficient for monopole signatures. This reconstruction provides a direction in zenith θ and azimuth φ and a velocity v for an event[41]. The fit is improved by giving lower weights to hits far from the track [Aar14a]. If needed, this track reconstruction is used for all the following reconstructions.

In addition a likelihood fit with velocity as free parameter was developed. The parameterizations of the expected light yield and angular distribution, described in Chs. 4.2 and 3.3, were implemented. A single muon likelihood fit , which uses only the first photons reaching a DOM, was adjusted. These photons are expected to have undergone less scattering than later arriving photons. The likelihood fit did not improve reconstruction quality compared to the improved track reconstruction but gives better results for particular signatures. This will be discussed later in this chapter and is shown in Fig. 5.12.

Many variables are calculated by IceTray based on the topology of hits. Additional variables were developed for this work which also describe the time evolution. The variables which were used in this analysis are described in Tabs. 5.2 to 5.4. The choice of the variables is explained in the next section[42].

5.1.3 Quality cuts and background reduction

At this point of processing some events consist of only a few hits in the detector. They are most likely caused by noise or extremely low energetic particles (compared to IceCube's

---

[41]From here on an *event* means a split event or the entire recorded event if splitting was not necessary

[42]The described algorithms in this section are implemented in the IceTray modules LineFit , improved-LineFit, Gulliver (SPE1st) and CommonVariables.

Cut variable	Cut value	Data Rate [Hz]	Description	Motivation
θ_{iLF}	$\geq 86°$	23.0	Reconstructed zenith angle using improved LineFit	Muons from air showers above this angle are significantly reduced because of the thick atmosphere and ice; this also requires a cut on the successful fit-status of the reconstruction
n_{String}	≥ 2	18.6	Number of hit strings	Improve data quality and reduce pure noise events
n_{DOM}	≥ 6	16.4	Number of hit DOMs	Improve data quality and reduce pure noise event

Table 5.2: Description of quality cuts in this analysis and the according event rate. The 2nd column displays the condition which events are required to fulfill in order to be kept. The first cut reduces the rate of events which passed the Muon filter by several orders of magnitudes. The other two cuts reduce events which passed the LowUp filter or were split by the algorithm described above. They were chosen comparably loose to retain dim monopole signatures with low velocities. The second cut reduces the sensitivity of this analysis for the dimmest and slowest monopoles at an angle $< 7°$ in the order of less than 1%. It reduces noise-like events which are not sufficiently described in simulations and which therefore lead to a discrepancy of data to background simulation distributions.

sensitivity). A reliable reconstruction is not possible for these events. Therefore they are discarded when less than two strings or less than six DOMs are hit.

The most abundant event type in IceCube are muons or muon bundles produced in air showers. They produce a track-like signature in IceCube which develops downwards, illustrated in Fig. 4.10. Monopoles are expected to reach IceCube from all directions. Therefore a cut on the zenith angle θ_{iLF}, reconstructed with improved track reconstruction described in Ch. 5.1.2, was executed at 86 degrees. This angle is slightly above the horizon but the rate of events caused by air showers is significantly reduced due to their long path length through atmosphere and ice. The data rate of events, which pass these selection criteria[43], is given in Tab. 5.2.

5.2   Pull-validation

In principle, further event selection is feasible using the described variables in Ch. 5.1.2 in a simple cut selection (explained in App. C.1) due to the unique event type of monopoles in IceCube. However, it is not possible to produce sufficient background statistics (definition in App. D.1) for this type of analyses in reasonable CPU time to develop an analysis based on simulation. Other options, like defining off-source or off-time regions [Bri11], are also not available for monopole searches because they are expected to come from every direction at any time.

A method to improve the exploitation of available statistics are re-sampling techniques. Common tools, such as bootstrapping [Efr79] and cross-validation [Lac68], are thoroughly

---

[43]In IceCube's nomenclature, the remaining events in simulation and data are called the monopole level 3 selection.

The Pull-validation process
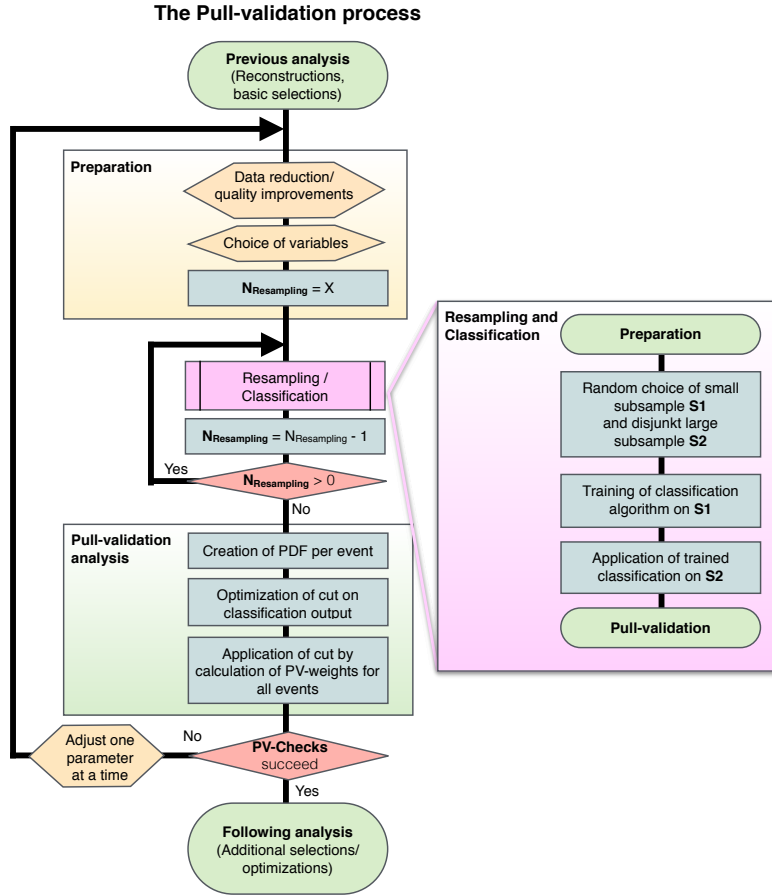
Figure 5.1: The pull-validation process visualized in a flow chart. Detailed explanation is given in Ch. 5.2.

tested using a conservative and therefore mostly fail-safe approach. Both methods are described in App. C.3. A new approach, called pull-validation, was developed for an IceCube analysis of atmospheric muon neutrinos [Sch14]. In that analysis pull-validation was used in parallel to cross-validation which illustrated that the results were reasonable but did not exploit the full power of pull-validation.

Validation techniques are usually combined with multivariate analysis (MVA), in this analysis with a boosted decision tree (BDT) [Qui86, Fre95]. The explanation of BDTs, their usual application, and the used parameters in this analysis are given in App. C.2. The following sections describe the usage of pull-validation on its own for this analysis, exploring its power and limits. This is also described in [Kun15a].

The goal of pull-validation is to estimate the statistical error at every point of a distribution as it is done with bootstrapping and cross-validation. In contrast to these methods the emphasis lies particularly on the distribution's tails, i.e. the end of statistics. In the extreme case, as in this analysis, where there are no simulated events and therefore an undefined error, only pull-validation enables the calculation of an error. The main idea is to create sub-samples from the sample with low statistics and to estimate the statistical
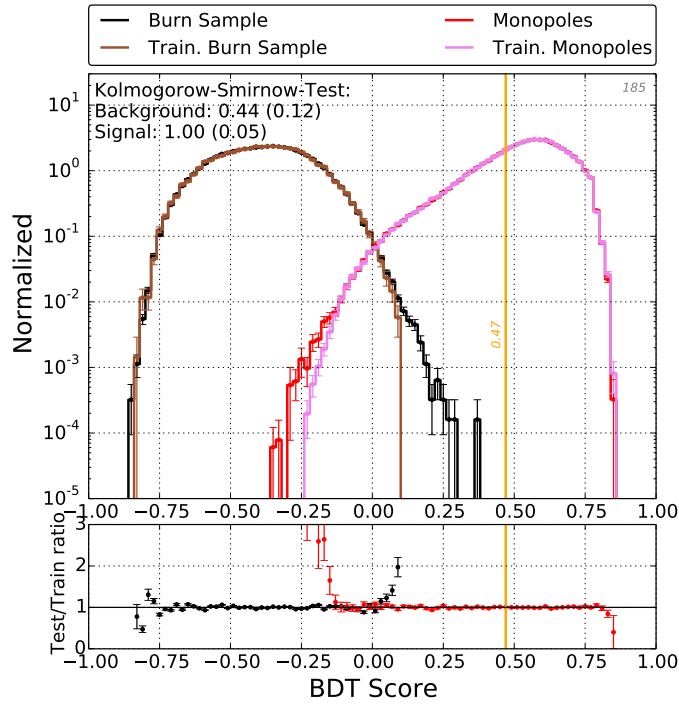
Figure 5.2: The overtraining check of the BDT model is usually obsolete in pull-validation since they will be averaged out by the many repetitions. The plot shows the Kolmogorov-Smirnow test statistic for both, background and simulation, and the corresponding p-value in brackets. This plot also shows the variation of a tail with $k = 1$ for the signal where S_1 is pink and S_2 is red. In addition the extension of a tail with $k = 10$ is shown using the burn-sample where S_1 is brown and S_2 is black which extends to higher BDT scores. The cut at BDT score 0.47, which is later discussed, is also shown.

error by considering the deviation between the sub-samples.

In detail pull-validation is a complex sequence shown in Fig. 5.1. The explanation of the steps, which is kept as general as possible, is supplemented with the description of the application in this analysis.

5.2.1   The pull

The main step of pull-validation, a pull[44], is shown in Fig. 5.1 (right) to be one re-sampling and classification step. Initially, the whole sample of available events S is randomly divided into a small S_1 and a large S_2 sub-sample

$$|S_1| \cdot k = |S_2| \ \text{ with } S = S_1 \cup S_2 \text{ and } S_1 \cap S_2 = \varnothing \tag{5.4}$$

---

[44]The term *pull* is not referring to a common term in physics: if fitting a number of points, the pull for each point is defined as (data-fit)/error. The pull distribution is then a Gaussian distribution around zero with standard deviation of one. Here, the term *pull* is referring to the creation of sub-samples by drawing values from the whole sample randomly.

The term *validation* implies the calculation of the statistical and systematic uncertainties of a model using an algorithm.

where $k > 1$ reflects the order of missing events which is to be compensated. However, k is restricted by the sufficient event number in S.

The classification algorithm, in this analysis a BDT, is trained on S_1 and the trained model is afterwards applied on S_2 supplying a BDT score distribution which is extending further (proportional to k) than the test distribution made with events in S_1. Fig. 5.2 illustrates this extension for this analysis.

The resulting distribution (later illustrated in Fig. 5.6) is highly dependent on the events chosen in S_1. Even a repeated training with $k = 1$ would not lead to equal but at least similar distributions. For larger k, in this analysis $k = 10$, the step to step variation of the distribution's tails is larger. This variation exploits the uncertainty between the sub-samples, the re-sampling uncertainty, which is interpreted as the statistical uncertainty of the whole sample in pull-validation.

The pull is repeated N_R times. Three different analyses, including this one, chose $N_R = 200$ [Sch14, Kun15b]. The optimal number can be found by

- calculating the mean (or median) μ and its error σ of arbitrary values, e.g. the final background rate, calculated using the tail of the BDT score distribution dependent on N_R

- choosing the smallest N_R where μ is not changing or σ is not longer decreasing significantly (a kind of exponential tail was observed in [Kun15b])

Choosing N_R too large leads to an overtraining effect (irregular features in the final re-sampled BDT distribution) because the different S_1 samples are correlated (which is reduced for large k).

In this analysis $N_R = 200$ was chosen due to the checks described in Ch. 5.2.4 and later confirmed with the method described above by [Kun15b].

5.2.2   Preparations

The extension of the S_2 tail compared to the S_1 tail of the BDT score distribution for $k > 1$ is a mathematical extrapolation of a variable, the BDT score (also discussed in App. C.2). The models, built by the BDT algorithm, span a multidimensional phase space. When the models are applied on any data with low statistics, some regions of this phase space are only sparsely populated. Due to the variation introduced by re-sampling, the data populates more parts of the phase space. This enables reliable statements on the sparsely populated regions of the phase space. When the sample S is prepared by pre-cuts in a way that the particular choice of variables describes the possible phase space of data comprehensively with the help of re-sampling, the extrapolation of the BDT score distribution is physically meaningful. This step is illustrated in Fig. 5.1 (top left). The subsequent sections described how it is checked that this aim is achieved.

mRMR order	mRMR score	Feature name	Description	Corr.	
1	0.3878	$n_{\text{DOM}_{100}}$	The number of hit DOMs within the specified cylinder radius in meters around the reconstructed track	5	*
2	2.3019	$\bar{s}$	The mean of all distances of hits from the reconstructed track	7	*
3	3.5803	t_{Gap}	Largest time gap between all hits ordered by time	11	*
4	2.8621	$d_{\text{Gap}_{100}}$	The maximal length of the track, which has no hits within the specified cylinder radius around the track	6	+
5	2.8736	d_{Sep}	The distance the Center-of-Gravity (CoG) positions of the first and the last quantile of the hits, within the specified track cylinder radius, are separated from each other	3	+
6	1.8508	$\bar{s}_{\text{NPE}}$	The average DOM distance from the track weighted by the total charge of each DOM	8	*
7	3.0710	$n^*_{\text{DOM}_{50}}$	The number of DOMs with no hit within the specified cylinder radius around the reconstructed track	1	*
8	3.3042	z_{travel}	Average penetration depth of hits defined from below $\langle z_{\text{DOM}} - \langle Q_{0.25}(z_{\text{DOM}}) \rangle \rangle$ where z_{DOM} is the z position of a DOM and $Q_{0.25}$ are the DOMs from the first quantile of hits	14	+
9	3.0468	z_{pattern}	All hits are ordered in time. If a DOM position of a pulse is higher than the previous z_{pattern} increases with $+1$. If the second pulse is located lower in the detector z_{pattern} decreases with -1. So this variable gives the tendency of the direction of a track	9	*
10	2.8114	$n_{\text{DOM}_{50}}$	The number of DOMs hit within the specified cylinder radius around the reconstructed track	2	*
11	2.7383	v_{proxy}	Reconstructed velocity using improved LineFit	13	+
12	2.3860	k_{100}	The smoothness values ranging from -1 to $+1$ giving the smoothness of distributed hits within the specified cylinder radius around the reconstructed track, see also Ref. [Nie01]	4	
13	2.1754	t_w	The weighted deviation of all hit times from the charge weighted mean of all hit times distribution	12	*
14	2.1539	t	Time length of an event; calculated by ordering all hits in time and subtracting the last from the first time value	10	*
15	1.9562	$\bar{z}_{\text{DOM}}$	Mean of all z_{DOM} per event	15	
16	1.9076	n^{L1}_{NPE}	Number of reconstructed photo-electrons in the outer layer of strings		*
		...			

Table 5.3: BDT features scored using mRMR. The score is relating to maximum relevance whereas the order relates to both relevance and correlation. Altogether 50 out of 58 tested variables where scored > 0. Variables with a star in the last column are particularly developed for this analysis. A plus marks the variables which are also used in the event selection before pull-validation. The number in the penultimate row is used in Fig. 5.3. Distributions of all variables before the final cut are shown in Figs. E.4 to E.18.
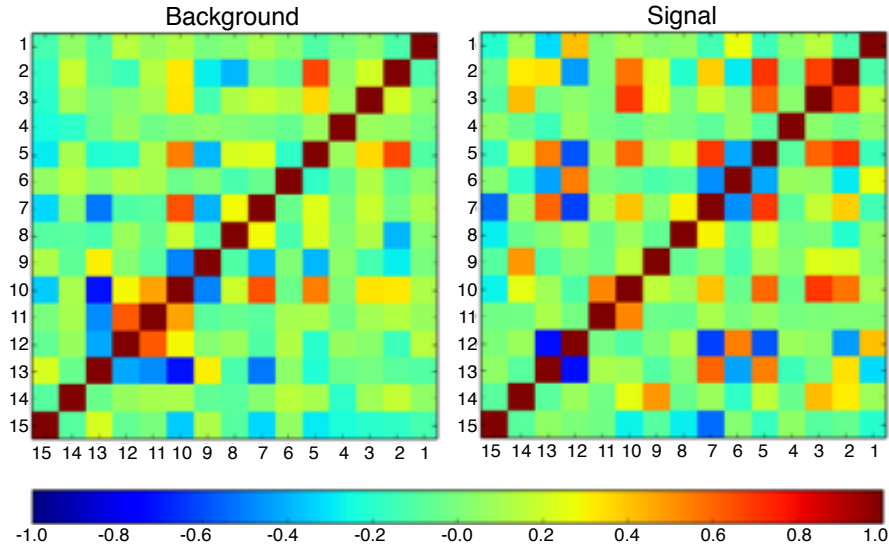
Figure 5.3: Correlation matrices of all used variables in the BDTs for background (left) and signal (right). Though there are some variables which show a (anti-) linear correlation this is mostly only the case for one event class. The variable numbers are given in Tab. 5.3. Non linear correlations were also checked by drawing scatter plots for all variable combinations.

The BDT score has no physical equivalent itself but it is calculated out of variables which describe the physics of an event. Therefore the BDT score has a physical meaning despite that it is unknown exactly how it is calculated. For example a change of slope in the BDT score distribution usually hints to a change of event types (with different rates) at these score values. With this in mind, the distribution can be changed by applying cuts before performing pulls. The cuts account for unwanted event types, i.e. event types that are not well described by the available statistics. The pre-cuts can also be used to reduce disagreement of data and simulated events in certain variables because this leads to the overtraining effect described in the last section.

Compared to simple BDT analyses the number of variables, or features, N_V used for training has to be increased. Optimization can be done by the calculation of

- stability: "the sensitivity of a method to variation in the training set" [Kal07]

- performance: the probability that the feature will rank a randomly chosen signal-like instance higher than a randomly chosen background-like instance [Faw06]

- tree importance: a value depending on the number of usages of a feature in all trained BDT models [Fri01]

Ideally stability and performance are saturated and tree importance is barely > 0. This approach for optimization is a *wrapper method* which means that it optimizes using the specific learning method. It requires high computational effort and does not reduce the correlation between variables.

Cut variable	Cut value	Data Rate [Hz]	Description	Motivation
v_{proxy}	$\leq 0.83\,c$		Reconstructed velocity	Only used in training to focus on low velocities
v_{MC}	$\leq 0.76\,c$		Simulated and true velocity	Only used in training to focus on low velocities
$d_{\text{Gap 100}}$	$\leq 300\,\text{m}$	$1.41 \cdot 10^{1}$	The maximal track length of the track, which got no hits within the specified track cylinder radius in meters	Reduce coincident events and noise events
d_{Sep}	$\geq 350\,\text{m}$	$2.62 \cdot 10^{-1}$	The distance the Center-of-Gravity (CoG) positions of the first and the last quartile of the hits, within the specified track cylinder radius, are separated from each other.	Reduce down-going events, corner-clippers, and cascades
z_{COG}	$\geq -400\,\text{m}$	$2.40 \cdot 10^{-1}$	The z value of the position of the CoG of the event.	Reduce wrongly horizontally reconstructed high energy tracks at the bottom of the detector
z_{travel}	$\geq 0\,\text{m}$	$1.30 \cdot 10^{-1}$	z_{DOM} is the height z of the position of a certain DOM. Then, z_{travel} is the average penetration depth of hits defined from below: The average over (z_{DOM} minus the average over the z_{DOM} values of the first quartile of all hits)	reduce coincident events, down-going tracks and cascades
BDT score	≥ 0.47	$1.12 \cdot 10^{-7}$	Score ranging from -1 to 1 representing how signal- like an event is	For the choice of the value see text; see Tab. 5.3 for the used variables

Table 5.4: Description of pull-validation cuts in this analysis and the according event rate. The sign in the 2nd column displays the condition which events are required to fulfill to be kept. Variable distributions are shown in Figs. 5.4, 5.5 as well as in Figs. E.1 to E.3.

In this analysis, tree importance turned out to deliver unstable results. The choice of the tool Minimum Redundancy Maximum Relevance (mRMR) [Pen05] delivered better results and also fulfills the performance criteria. The tool uses a *filter method* which is defined to be independent of the learning method but selecting features depending on their discrimination power regarding the event classes. The advantage of mRMR is the choice of low correlated variables, see Fig. 5.3, which leads to a complete description of the sample in regards of the parameter space.
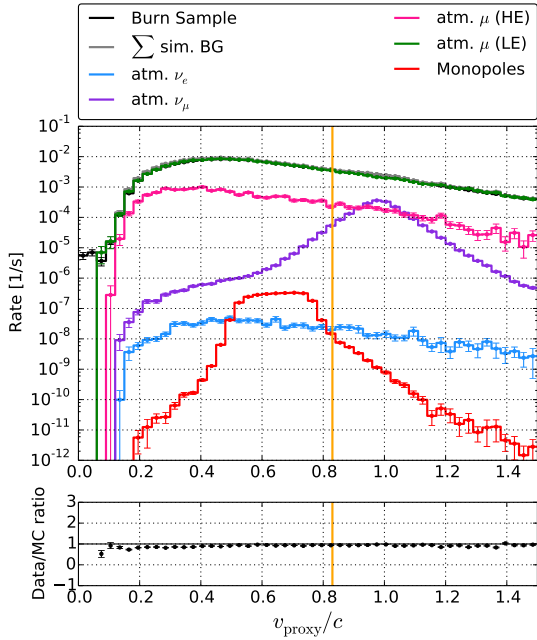
Figure 5.4: Cut on the reconstructed velocity v_{iLF} using the improved LineFit (see section 5.1.2) which was used only for training. Also just for training a cut on the true velocity at $v_{MC} \leq 0.76\,c$ was performed. Compare Tab. 5.4. Taken from [Pol16].
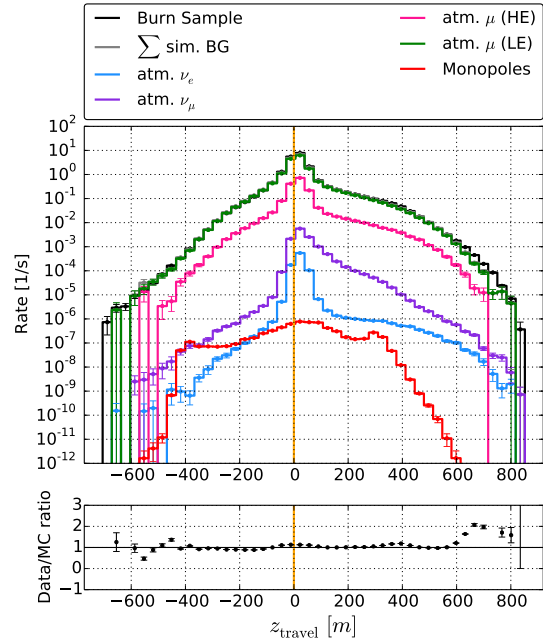
Figure 5.5: Cut on the averaged penetration depth of hits which reduces coincident events. The data/simulation disagreement for $z_{travel} > 600$ is removed in combination with the pre-cuts. Compare Tab. 5.4.

It is assumed that events, which are not in the sample S, lie in this parameter space. Figuratively, the sample is fitted with a multidimensional function and it is assumed that events $\notin S$ could also be described by this fit. The features chosen in this analysis are tabulated in Tab. 5.3 and illustrated in App. E.4.

Concluding, the adjustable parameters of pull-validation are the number of re-samplings, N_R (as described in the last section), the choice of variables N_V, and the choice of pre-cuts. The latter in particular had to be adjusted several times for this analysis. An overview of the final selection of cuts is given in Tab. 5.4 though there are two cuts which need to be explained in detail:

A combination of two cuts was performed on the speed which reject high reconstructed velocities $v_{proxy} > 0.83\,c$ and high true velocities $v_{MC} > 0.76\,c$, see Fig. 5.4. These cuts were used only for the training of the BDTs and removed for testing and application. The purpose was to let the BDTs focus on monopole signals with small velocities and learn their specifications since this analysis targets especially the parameter range where only indirect Cherenkov light occurs.

The second cut used a variable z_{travel} which calculates, stated simply, the averaged penetration depth of a track from below into the detector. See Tab. 5.3 for precise definition. Lower z_{travel} result from down-going tracks, cascades, and coincident events. The latter
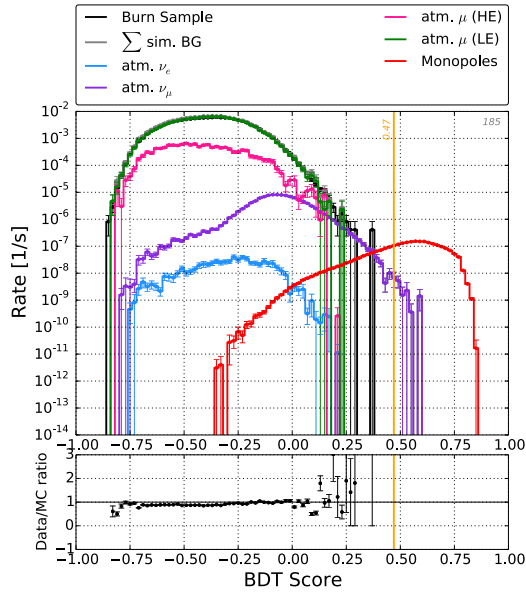
Figure 5.6: BDT score distribution which is the result of one pull. Taken from [Pol16].
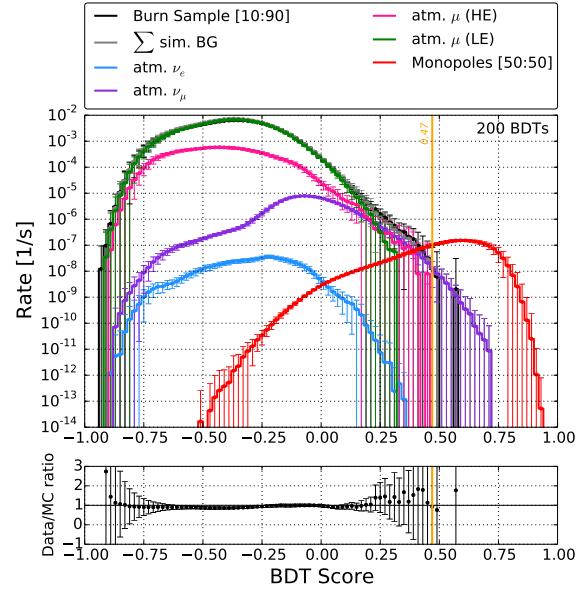
Figure 5.7: Averaged BDT score distribution using $N_R = 200$. Taken from [Pol16].

cause a large variety of topologies in the detector and the BDTs could not reject them sufficiently when the pre-cut was as soft as $z_{\text{travel}} \geq -10$. However, a cut keeping only events with $z_{\text{travel}} \geq 0$ (see Fig. 5.5) leads to a better training of the remaining coincident events and also to a suppression of air shower events (actually only comprising coincident events and representing only four days of data) compared to μ-neutrino tracks in the final BDT score distribution (see Fig. 5.6 and 5.7). Unless there would be a new, not simulated, event topology, it was not expected that after unblinding the air shower data would show a different slope and supersede the suppression. This is supported by the fact that the available burn-sample of 31 days does not show any feature in the distribution though it already has almost one order of magnitude higher statistics than the air shower simulation.

5.2.3 Analysis

After the re-sampling and classification every event has N_R BDT scores assigned, see Fig. 5.1 (bottom left). The BDT score distribution per event can be normalized and interpreted as a probability density function (PDF) of that event. The tails of the PDF contribute to the previously sparsely populated regions of the phase space. A Gaussian distribution is expected, as shown in [Kun15a]. The resulting BDT score distribution for all events, illustrated in Fig. 5.7, is smoother in the tails when compared to one arbitrarily chosen not-resampled distribution, such as in Fig. 5.6.

In this analysis the PDFs are not used directly since the processing of all PDF requires a lot of CPU time. Instead, the N_R histograms of the BDT score are averaged per bin which
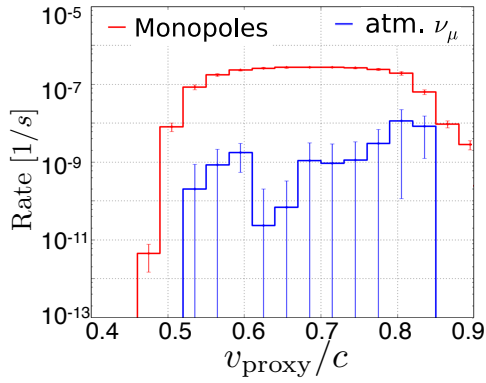
Figure 5.8: Distribution of the speed obtained from the improved track reconstruction estimated after application of the BDT cut.
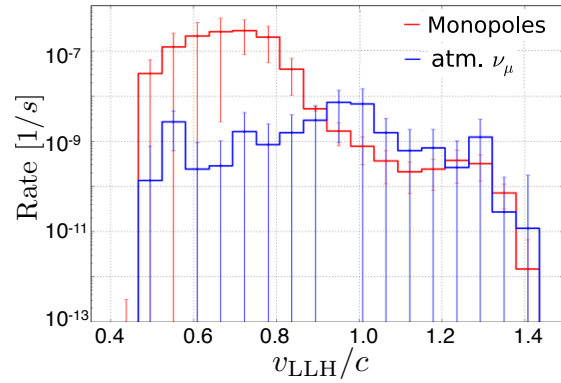
Figure 5.9: Distribution of the speed obtained from the likelihood fit after BDT cut.
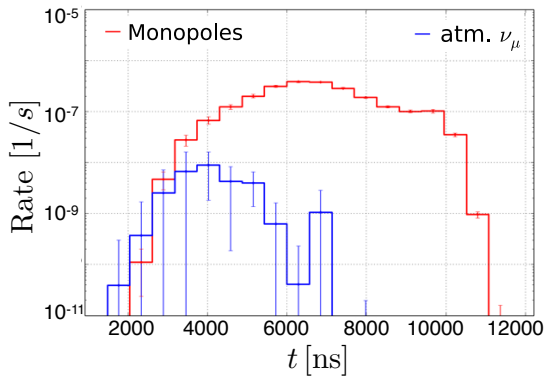
Figure 5.10: Estimated time-length distribution after last cut.
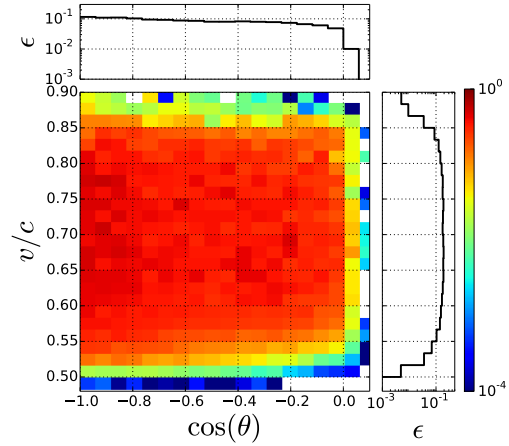
Figure 5.11: Efficiency ϵ of the analysis shown in zenith and speed. The efficiency is the ratio between the signal events which pass all cuts and the number of simulated signal events. The analysis selects upgoing events with velocities of $0.60\,c$ to $0.84\,c$ best.

gives the same result. If single events are treated for further calculations the PDFs per event have to be used instead. Figure 5.7 shows the mean and standard deviation per bin.

Based on the averaged BDT distribution a cut value can be chosen. The application of the cut on every event PDF gives the probability of an event to be retained by the cut which is called the pull-validation weight (PV-weight) here. This weight can be used for further analyses such as for drawing the expected distributions after the last cut. The final signal efficiency of this analysis is plotted in zenith and speed in Fig. 5.11.

Comparison of Fig. 5.8 and 5.9, the likelihood fit, described in Ch. 5.1.2, identifies corridor
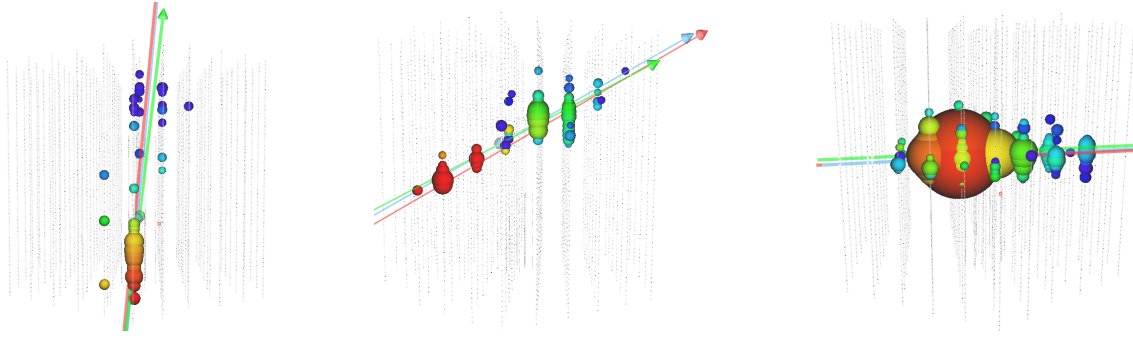
Figure 5.12: Signatures of expected background types: A vertical corridor event slips through the gap between strings (left). A through-going track comprising a cascade also gives $v_{\text{proxy}} < v_{\text{MC}}$ (middle). A track starting inside the detector with a cascade gives $v_{\text{proxy}} < v_{\text{MC}}$ as well as stopping tracks (right). The red line denotes the true, i.e. simulated direction, the blue and green lines show the reconstructed track using the likelihood fit and the LineFit.
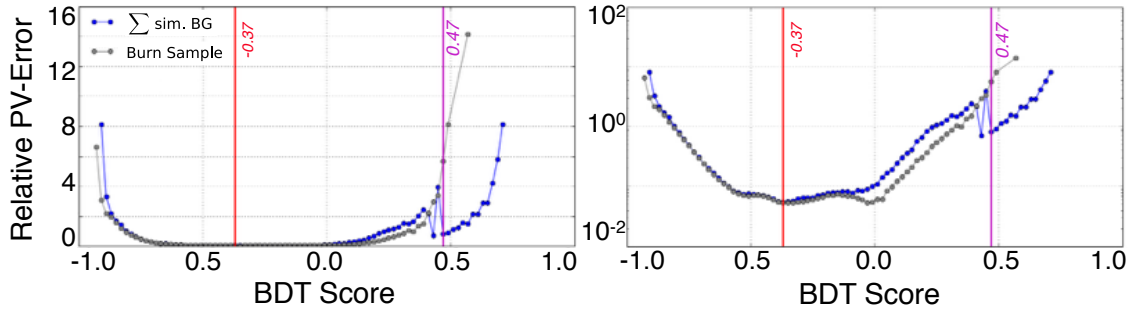
Figure 5.13: Relative PV-errors using mean and standard deviation for visualization. The calculation of two points in this distribution is shown in Figs. 5.14 and 5.15. The jump at ~ 0.5 in background simulation is from the end of air shower simulation statistics and transfer to μ-neutrino simulation. Lower relative errors in the burn-sample between 0 and ~ 0.4 are from the better statistics in the burn-sample compared to air shower background simulation. The opposite is the case for μ-neutrino simulation and burn-sample above 0.5.

events more often by reconstructing their true velocity $v_{\text{LLH}} \approx v_{\text{MC}} = 1\,c$. This type of event is explained in Fig. 5.12. A stochastical energy loss, i.e. a cascade, along a track-like event also changes the reconstructed velocity. Other background types are starting or stopping tracks, see Fig. 5.12, which have short event durations as shown in Fig. 5.10. A track, which comprises of a cascade, also gives smaller reconstructed velocities v_{proxy} compared to true velocities $v_{\text{MC}} = 1\,c$.

5.2.4   Checks

As explained at the beginning of this chapter pull-validation requires checks in order to be reliable when using it at its limits as done in this analysis. Therefore the final step of the pull-validation process, displayed in Fig. 5.1, is the fulfilling of check criteria. This
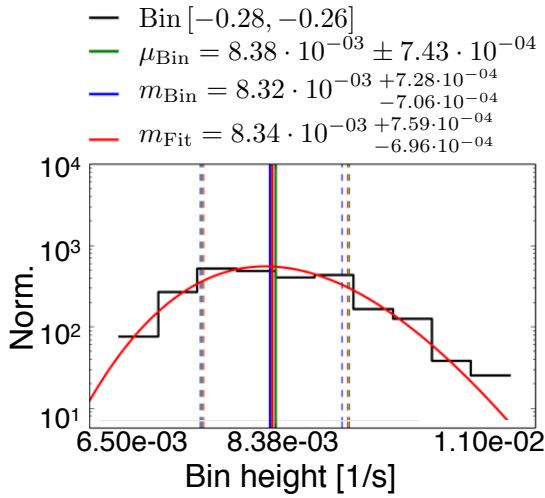
Figure 5.14: Bin height distribution (black) of a bin in the middle of the distribution between BDT scores of -0.28 and -0.26. Vertical lines show mean and standard deviation (green), median and quantile (blue). The fit (red) is a log normal distribution with the given parameters.
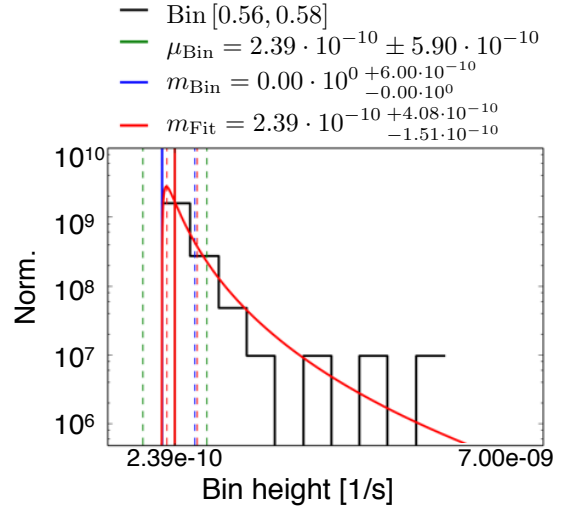
Figure 5.15: Bin height distribution of a bin in the tail of the distribution between BDT scores of 0.56 and 0.58. Standard software fails increasingly to calculate a median or a fit for larger BDT scores. On the x-axis the bin-height of the bin over $N_R = 200$ histograms is plotted. On the y-axis are the normalized counts.

also influences the choice of the optimal cut value which might be corrected in this step. If the checks fail, the whole process has to be repeated with adjusted parameters, see preparations in Ch. 5.2.2[45].

In this analysis the uncertainty arising from the re-sampling of pull-validation, or PV-error, is the fluctuation of the bin heights from histogram to histogram in the BDT score distributions, Fig. 5.7. The distributions can be fit with a log-normal distribution as shown in Fig. 5.14 and 5.15. To be most accurate in this analysis the actual distribution is used instead of the fit as re-sampling error for calculations. For visualizations the mean and standard deviations are used, for example in Fig. 5.7.

The relative PV-error is visualized also in Fig. 5.13. It exceeds 100% at the final cut value. This dominates over all other errors which will therefore be neglected at this stage.

The usual Poisson error which is used as statistical error per bin vanishes over the N_R re-samplings. However, the background statistics still depend on the simulation statistics. This is the amount of simulated events (without spectral weight described in Ch. 4 and App. D.3 as well as PV-weight) which contribute to the quantity of remaining events. In this analysis these are 370 events which give a Poisson of $< 5\%$.

On the other hand those events contribute with different spectral weights to the final background expectation, as shown in Fig. 5.16. However, adding the PV-weight only one

---

[45]To give the reader an impression: this had to be done about 50 times for this analysis. Therefore this step is implemented into the analysis code.
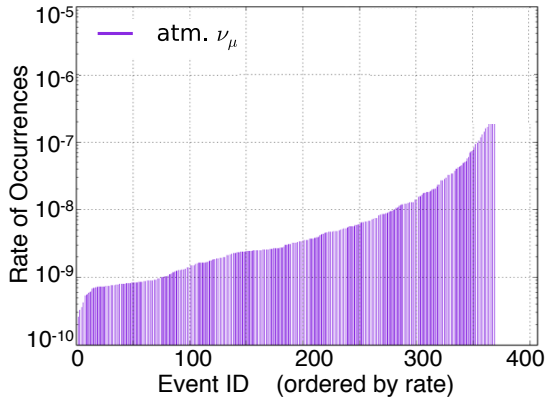
Figure 5.16: Simulated events contributing after final cut (using only spectral weights, no PV-weights). The slope is comparably flat meaning that the rate differs by the same order of magnitude as given by the number of events.
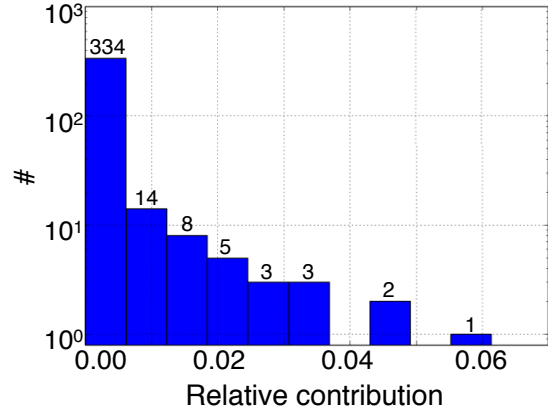
Figure 5.17: Contribution on the background expectation of simulated events after final cut (including PV-weights). One event contributes to the calculated background rate by 6.1 % and all other events have smaller contributions.

event contributes with $< 7\,\%$. This means, the final value would change by less than $7\,\%$ if this particular event had not been simulated[46], see Fig. 5.17.

Further checks for stability of pull-validation with the chosen parameters are[47]:

- the repetition of the analysis with same data and configuration should provide the same results, otherwise too few events describe too many different background types

- the value(s) of the final result, for example Fig. 5.7 or the expected background rate, should not change with increasing N_R except from the re-sampling errors which decrease further

- the choice of variables is checked by a so-called fake-unblinding: The whole pull-validation process is applied on a strongly reduced sample (in this analysis $S_1 = 1\,\% \cdot S$ and $S_2 = 9\,\% \cdot S$). The final cut value is chosen using the same rules and an estimated background rate as well as a confidence interval is calculated. Then, the following conditions must be fulfilled:

  - most attempts should provide the expected neutrino rate

  - some BDT vary a lot and exploit the whole confidence interval

  - no attempt gives an over-fluctuation outside the confidence interval which could be misinterpreted as a signal

- the value(s) of the final result should not change when applying different detector simulations or background fluxes to calculate the systematic uncertainties of the analysis

---

[46]The other way round is not possible to test.
[47]Not all of these tests succeeded for different tested configurations.

Type	ν_μ in %	Signal in %
Statistics	6.8	0.4
Pull-validation / re-sampling	See text	See text
DOM efficiency	8.10	1.32
Ice-model	3.87	1.19
Absorption and scattering	11.79	2.38
Flux	8.15	-
Total (without PV)	16.91	2.97
Rate uncertainty after last cut [events / livetime]	0.093	1.578

Table 5.5: Uncertainties in this analysis, averaged over the entire velocity range. See Fig. 5.20 for the velocity dependence.

The above issues were checked successfully for the described configuration of this PV-analysis.

5.3 Uncertainties

In addition to statistical errors and PV-fluctuation the detector response and neutrino flux models contribute to the uncertainties of the final background flux. To take the theoretical uncertainty of the neutrino flux into account different flux models are used as described in Ch. 4.1.2. Electron-neutrino rate, astrophysical neutrino rate, and air shower rate are reduced to zero by event selection and therefore not considered here.

The detector uncertainty is measured by comparing several simulations that have one parameter varied. These parameters are:

- the DOM efficiency, which is short for the quantum efficiency of the PMT, is varied by $\pm 10\,\%$

- the ice-model, of which the latest and next-to-latest are compared

- absorption and scattering of the ice, which are each varied by $\pm 10\,\%$

Asymmetric uncertainties are assumed to be Gaussian uncertainties, equal to the larger of the two values. Statistical fluctuations are added because they are partly of the same order of magnitude. Finally, all uncertainties are added in quadrature assuming independence. All values are listed in Tab. 5.5.

5.4 Background expectation

The final cut on the PV-distribution is optimized using the Feldman-Cousin approach. Since the uncertainties due to re-sampling are large they are included in the sensitivities.

For that the Feldman-Cousin approach has to be adjusted. In this context the calculation of the final limits is defined to fix the procedures which follow unblinding.

The aim of this section is to estimate the background rate after unblinding. If the value is overestimated, the values of the final limits would be inadequately scaled down, i.e. improved. If the value is underestimated, a larger number of remaining events after unblinding would have to be interpreted as detected signal. Therefore, a crucial input into the following calculations is the uncertainty of the background rate estimated by pull-validation.

5.4.1   Model rejection factor

In this analysis the Feldman-Cousin [Fel98] approach is used to calculate the sensitivity, which is defined as the efficiency of analysis suppressing background while gaining a high detection probability. The application of this approach for analyses is described in detail in [Hil03].

The model used in this analysis is a monopole flux assumption near the exclusion limits of prior analyses $\Phi_0 = 1.68 \cdot 10^{16} \, \mathrm{cm}^{-2}\mathrm{s}^{-1}\mathrm{sr}^{-1}$ for one characteristic velocity out of the range of simulated velocities. This flux limit lies between the MACRO and ANTARES limits illustrated in Fig. 2.5. This gives the number of expected signal events n_s per livetime $t \approx 311 \, \mathrm{d}$

$$n_s = w_M \cdot n_{\mathrm{cut}} \cdot t \quad \text{with} \quad w_M = \Phi_0 \cdot \frac{A \cdot \Omega}{n_{\mathrm{sim}}} \qquad (5.5)$$

where n_{sim} is the number of simulated events and n_{cut} is the number of events which remain after all cuts. The monopole weight w_M accounts for area of the disc of the monopole generator A, described in Ch. 4.2.1, and the space angle Ω.

The confidence interval $\mu_\alpha = [\mu_1, \mu_2]_\alpha$ is defined as the range which includes the true value of a observable n with a certain frequency or confidence level α if you repeat an experiment many times. In mathematical terms this means

$$P(n \in \mu_\alpha) = \alpha \qquad (5.6)$$

If this is satisfied, μ_α has the correct coverage. This analysis uses $\alpha = 90\,\%$ which is the same as for comparable analyses. The calculation of μ_α is shown in [Fel98].

The upper flux limit, using the model rejection potential (MRP) described by Feldman and Cousin, is

$$\Phi_{90} = \Phi_0 \frac{\mu_{90}(n_{\mathrm{obs}}, n_b)}{n_s} \qquad (5.7)$$

where the confidence interval μ_{90} depends on the number of background events n_b and the number of observed events n_{obs}. For calculation of the sensitivity, this has to be adjusted because n_{obs} is unknown prior to actually performing the experiment [Hil03]. Therefore
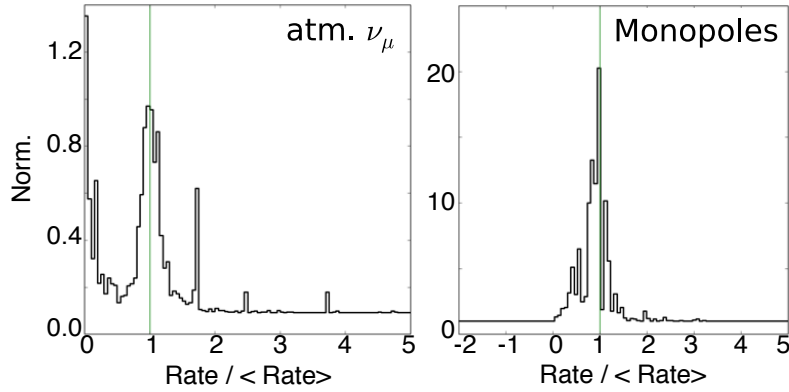
Figure 5.18: Background (left) and signal (right) uncertainty distribution of the rate after final cut. The x-axis is divided by the mean rate. The y-axis is normalized. For background many BDTs give a zero background rate for a cut at a BDT score of 0.47 due to missing statistics. Few outliers among the BDTs due to few events with high weights give significantly larger background rates after final cut and cause the peaks. In contrast, the signal uncertainty is almost symmetric because it has sufficient statistics.

μ_{90} is replaced by the weighted average limit $\bar{\mu}_\alpha$ with the weight given by the Poissonian probability $P_{n_b}(n_{\text{obs}})$ for observing n_{obs} events with mean n_b

$$\bar{\mu}_\alpha = \sum_{n_{obs}=0}^{\infty} \mu_{90}(n_{\text{obs}}, n_b) \, P_{n_b}(n_{\text{obs}}) \tag{5.8}$$

$$= \sum_{n_{obs}=0}^{\infty} \mu_{90}(n_{\text{obs}}, n_b) \, \frac{(n_b)^{n_{\text{obs}}}}{(n_{\text{obs}})!} \, \exp\left(-n_b\right) \tag{5.9}$$

To get the most stringent limits the event selection is chosen to minimize the model rejection factor (MRF) defined as $\bar{\mu}_\alpha/n_s$ for the final cut [Hil05a]. Combining Eqs. 5.7 and 5.8 gives the sensitivity

$$\bar{\Phi}_{90} = \Phi_0 \frac{\sum_{n_{obs}=0}^{\infty} \mu_{90}(n_{\text{obs}}, n_b) \, P_{n_b}(n_{\text{obs}})}{n_s} \tag{5.10}$$

which does not account for uncertainties. The sensitivity is not dependent on the choice of the initial flux Φ_0 since n_s is proportional to Φ_0.

5.4.2 Calculation of sensitivity

In this analysis the number of background events n_b has a large uncertainty. The values of n_b and n_s are dependent on the BDT score as they are calculated by integrating all events in the BDT score interval $[a, 1.0]$ with a decreasing for each pull. The resulting distributions of n_s and n_b are normalized as probability mass functions (PMF) $P_{\text{pull}}(n_{b/s})$, shown in Fig. 5.18. Thus the final sensitivity is given by

$$\bar{\Phi}_{90} = \Phi_0 \cdot \frac{\sum_{n_b=0}^{\infty} \sum_{n_{obs}=0}^{\infty} \mu_{90}(n_{obs}, n_b) \cdot P(n_{obs}, n_b) \cdot P_{\text{pull}}(n_b)}{\sum_{n_s=0}^{\infty} n_s \cdot P_{\text{pull}}(n_s)} \tag{5.11}$$
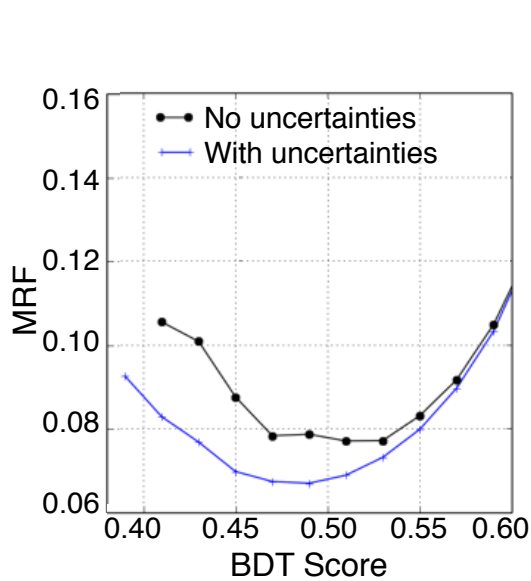
Figure 5.19: MRF as a function of the BDT score cut value. The minimum of the MRF including uncertainties is at 0.49. Due to the uneven uncertainties when the air shower simulation's statistics ends there is no single minimum for the MRF without uncertainties.
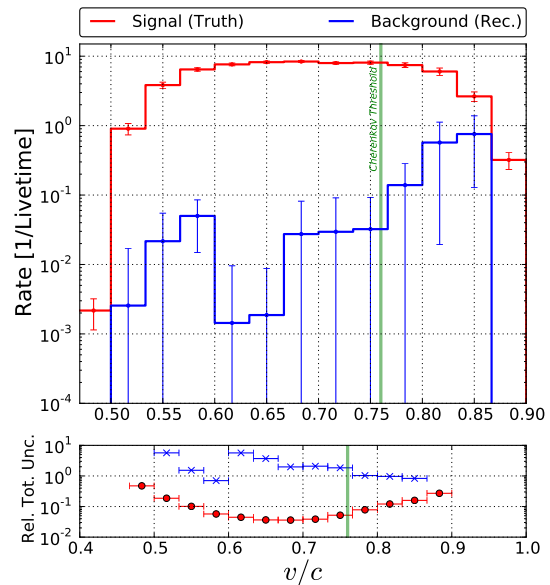
Figure 5.20: Velocity distribution showing the simulated velocity for signal and reconstructed velocity for background. The lower part shows the total relative uncertainties as a function of the velocity.

For calculation of the sensitivity only the dominating uncertainty, i.e. the re-sampling uncertainty, is used. This gives the MRF distribution shown in Fig. 5.19 where all velocities are averaged.

This result leads to the expectation of several signal events in the burn sample. An advantage of BDTs in contrast to other machine learning algorithms is that a small amount of signal contamination does not worsen the training results. However a signal contamination could lead to a cut at higher BDT scores. To avoid this the burn sample events near the cut value are looked at by eye. The decision was made to keep training on burn sample instead of simulation because of the much longer livetime for air shower events.

The final cut was chosen at a BDT score of 0.47. This is slightly softer than the minimal value of the MRF at 0.49. The decision was made based on the checks presented in Ch. 5.2.4. A softer cut increases the number of partially remaining background events. Therefore the estimated background rate, which is derived from them, is based on more information.

5.4.3 Calculation of limit

The uncertainties described in Ch. 5.3 are included in the final limit. However, the assumption of a Gaussian distribution for the uncertainties can lead to unphysical negative
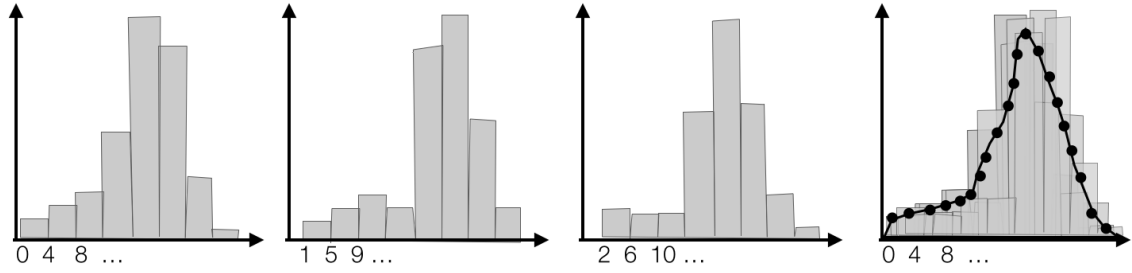
Figure 5.21: Illustration of the principle of averaging histograms with different starting points. The first three histograms are made of the same data, using the same bin width, but starting at different origins. The last plot shows the overlay of the first three histograms. The average of the bin heights (black dots) represent the true distribution of data better than one of the three histograms which indicate different distributions.

values of the event number n in the calculation. Therefore, a truncated normal distribution is used instead which ensures positive values for n_s and n_b [Aar14d, Pos13a]

$$P_{\text{unc}}(n|\lambda, \sigma) = \int_0^\infty \frac{(\lambda + x)^n\, e^{-\lambda - x}}{n!} \cdot w(x|\sigma)\, dx \qquad (5.12)$$

where λ is the central value of this weighted average of Poisson distributions. The variance σ^2 is calculated as the quadratic sum of all individual uncertainties in Ch. 5.3. The weighting function w is a normal distribution with mean 0 and variance σ^2. Convoluting the PMFs for pull-validation variation P_{pull} and the truncated normal distribution for all other uncertainties P_{others} , the final limit is

$$\Phi_{90}(n_{\text{obs}}) = \Phi_0 \cdot \frac{\sum_{n_b=0}^\infty \mu_{90}(n_{\text{obs}}, n_b) \cdot P_{\text{unc}}(n_b) P_{\text{pull}}(n_b)}{\sum_{n_s=0}^\infty n_s \cdot P_{\text{unc}}(n_s) P_{\text{pull}}(n_s)} \qquad (5.13)$$

This method of including uncertainties leads to a slight over-coverage resulting in a conservative limit.

5.4.4 Velocity dependence

The mass and kinetic energy of magnetic monopoles in space is unknown and so is their velocity distribution at the detector. In Fig. 5.22, each single point at velocity v_i in this plot is the upper limit of the monopole flux under the assumption that all monopoles would have this particular velocity v_i when reaching the detector. Although some analyses handle all points with the same event selection, e.g. IceCube 40, and others did not, e.g. ANTARES, all points have to be interpreted as the result of individual analyses considering only the velocity v_i.

In this analysis a uniform distribution of velocities was simulated, see Ch. 4.2.1. After event selection this results in a velocity distribution, shown in Fig. 5.20, which gives the rate per velocity bin and livetime for background and signal simulation, each re-sampled. For signal the simulated and for background the reconstructed velocity is used. The bin-width $\Delta v = 0.033\, c$ is chosen to comprise of at least $90\,\%$ of the reconstructed signal
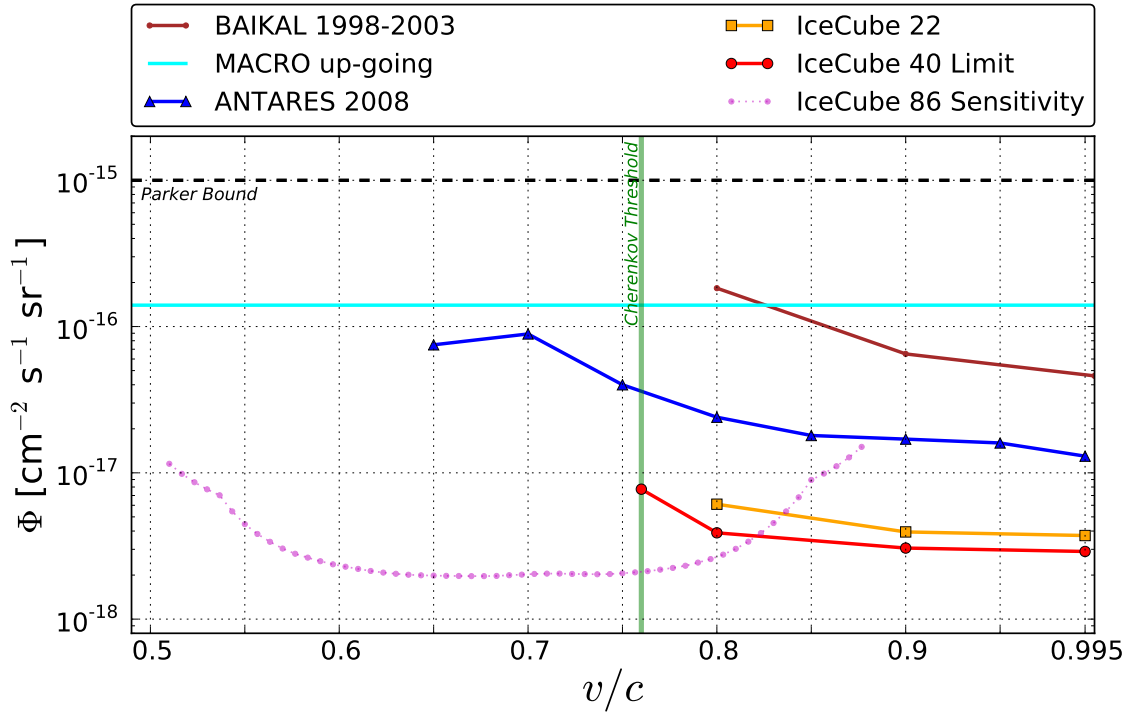
Figure 5.22: Analysis sensitivity compared to the analyses from MACRO [Amb02], BAIKAL [Ayn08], AMANDA [Abb10b], ANTARES [AM12], IceCube 22 [Abb13], and IceCube 40 [Pos13a, Pol16]. A line is drawn through all limits for characteristic velocities to guide the eyes. Near the Cherenkov threshold the expected sensitivities exceed the IceCube 40 monopole analysis by more than a factor of 2 which could be explained by the larger detector volume. Due to the different expected brightness of the signal (see 3.11), especially near the threshold, the optimization of an analysis to the velocity range is crucial. The IceCube 40 analysis is optimized for velocities between $0.76\,c$ and $0.995\,c$ depending heavily on the brightness. Therefore the IC40 limit is increasing for slower velocities.

velocities. The reconstruction resolution of background events is worse since a velocity of c is expected for all of them.

For each bin in Fig. 5.20 the sensitivity is calculated as described in Ch. 5.4.2 using the bin-heights. The result is then normalized by multiplying with the bin-width Δv and dividing with the integration range $[0.4, 0.99]$ of the model's flux Φ_0. Therefore the final sensitivity has the same meaning as for the other experiments.

The shape of histograms with the same configuration and data, starting at different values on the x-axis with equal bin widths, vary significantly however this does not reflect any physical meaning [Hae07]. To avoid this, and to bring out the physical meaning, the start of the velocity histogram v_s is shifted five times

$$v_s = 0.4 + \frac{h}{5} \cdot \Delta v \text{ with } h \in \{0, 1, 2, 3, 4\} \tag{5.14}$$

which gives five different velocity histograms with different sensitivity step functions. The step functions are averaged which results in a smoother behavior of the limits, see Fig. 5.21.

Eventually in Fig. 5.22 only the mid velocity of these averaged steps is shown as a point since the averaged steps are small and a step function would mis-represent the bin width. Due to these small steps and the normalization, the points can be compared to analyses from other experiments.

5.5 Discussion

For calculation of the sensitivity the restrictions on the velocity described in Ch. 5.2.2 are relaxed. Therefore it is also possible to calculate sensitivities for velocities above the Cherenkov threshold $v_c = 0.76\,c$ because the simulation ranges from $0.4\,c$ to $0.995\,c$. However the sensitivities are increasing above $0.8\,c$ because the event selection focused on slower velocities. Below $0.6\,c$ the sensitivities also get worse because the brightness of the monopole signal falls below the detection capacity of IceCube.

The analysis is most effective at velocities between $0.6\,c$ and $0.8\,c$. The sensitivities are competitive to the other experiments and analyses over the range $0.51\,c$ to $0.83\,c$. The best sensitivity is achieved at $v = 0.677\,c$ with a value of $1.97 \cdot 10^{-18}\ \mathrm{cm}^{-2}\mathrm{s}^{-1}\mathrm{sr}^{-1}$. This is an improvement of almost two orders of magnitude which reflects a huge detection potential.

The arithmetic mean rate and standard deviation of expected background events per lifetime is 0.546 ± 0.212 and of the signal events according to the assumed model 68.000 ± 3.517. The confidence upper limit of background events is 3.61 events which is more meaningful. These events are expected to be most probably of the shape described in Fig. 5.12.

6 Results

The event selection was finalized by ultimately choosing all cut values and training the pull-validation. Unblinding was then performed which is the application of this analysis on the data from season 2011 excluding the burn sample.

In this chapter the result of unblinding is presented. Based on the discussion of the outcome, limits are calculated and put into context by comparing with limits from other experiments.

6.1 Unblinding

The unblinding proposal comprises of the data selection through the Muon filter, LowUp filter, and EHE filter streams which will be further reduced with the described cuts using one of the trained BDTs, chosen at random [Pol15]. The efficiency all cuts in the analysis is shown in Fig. 6.6.

The procedure after unblinding is dependent on the outcome

- If no event remains after all cuts, an upper limit on the monopole flux is set as described in Chs. 5.4.3 and 5.4.4.

- If a small number of events is retained, they are assumed to be consistent with background. An upper limit on the monopole flux is set as described in Chs. 5.4.3 and 5.4.4. The events are investigated further because it cannot be excluded that a monopole signature is among the selected events.

- If a large number of events passes all cuts, they have to be investigated further. The over-fluctuation has to be verified by further systematic studies. If the over-fluctuation is significant, either a lower limit could be set or a discovery would be claimed.

When the unblinding was finally performed, 3 events fulfill all selection criteria. Event views of the unblinded events are in Figs. 6.1 to 6.3. The scaling for the DOM charge, illustrated by the hit DOM radius, is equal for all event views in this work. The red arrow denotes the reconstructed direction from ImprovedLinefit. Near the middle of the detector the dust layer causes higher absorption and scattering which prevents hits in this layer and causes noticeable gaps in the event signature.

6.2 Discussion

The number of three unblinded events is an over-fluctuation compared to the expected background rate with a mean of 0.55 events. However it is below the confidence upper
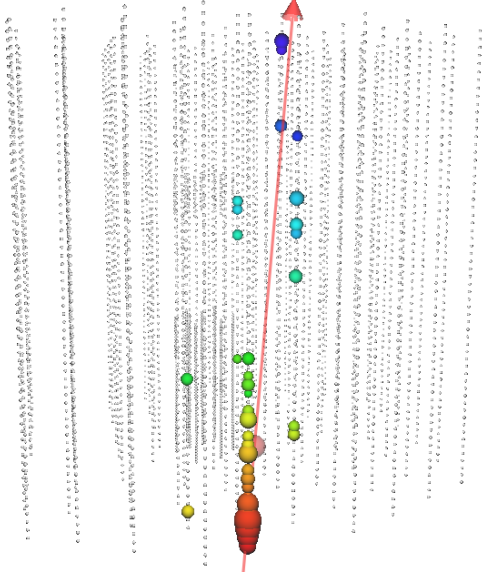
Figure 6.1: The first event which remained after unblinding is a through-going track with an upward direction and low brightness. This is likely to be the trace of the secondary from a low-energetic neutrino created in an air shower. Further reconstructed values are given in Tab. E.2.
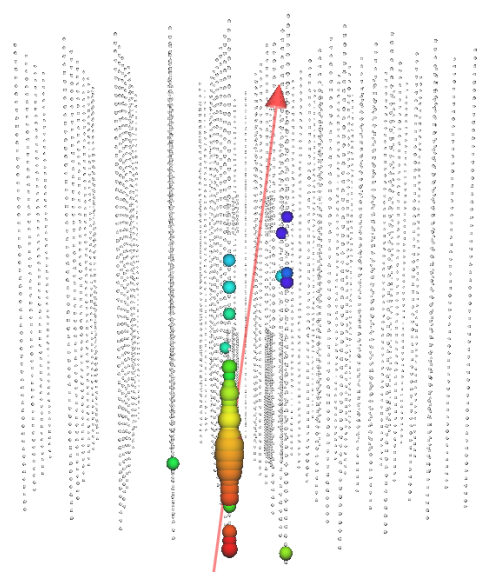
Figure 6.2: The second event which remained after unblinding is a stopping track with an upward direction and low brightness. This is likely to be the trace of the secondary of a low-energetic neutrino created in an air shower.
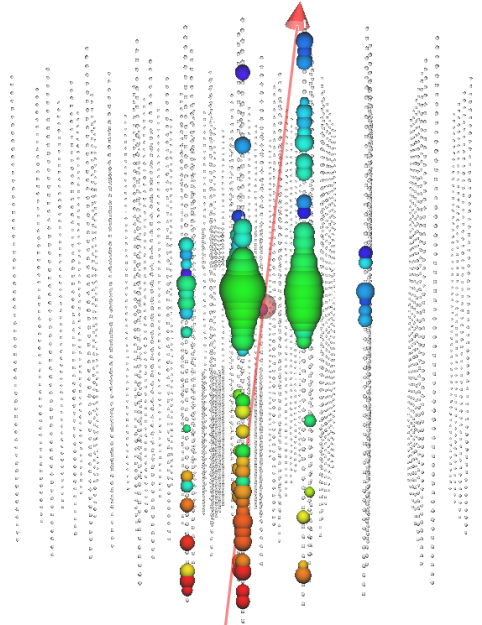
Figure 6.3: The third event which remained after unblinding due to its BDT score of 0.53, is a through-going track with an upward direction and mid brightness. There might be a low energetic cascade at mid height in the detector. 8 strings and 110 DOMs are hit with a brightness $n_{\mathrm{NPE}} = 595$ causing an after-pulse. Further reconstructed values are given in Tab. E.2. Taken from [Pol16].
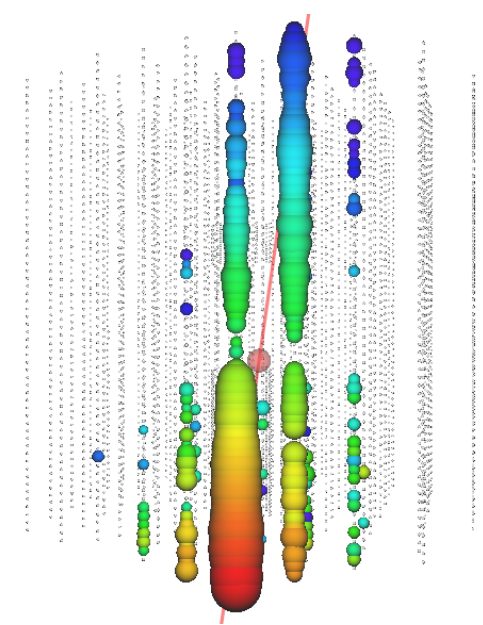
Figure 6.4: Simulated event with the same reconstructed variables as the third unblinded event. The reconstructed variables are a velocity of $v_{iLF} = v_{MC} = 0.83\,c$ and a zenith angle of about 170° in upward direction through the same part of the detector. In average of all simulated events, 196 DOMs on 11 strings are hit with a brightness of $\bar{n}_{\mathrm{NPE}} = 3600$. Taken from [Pol16].
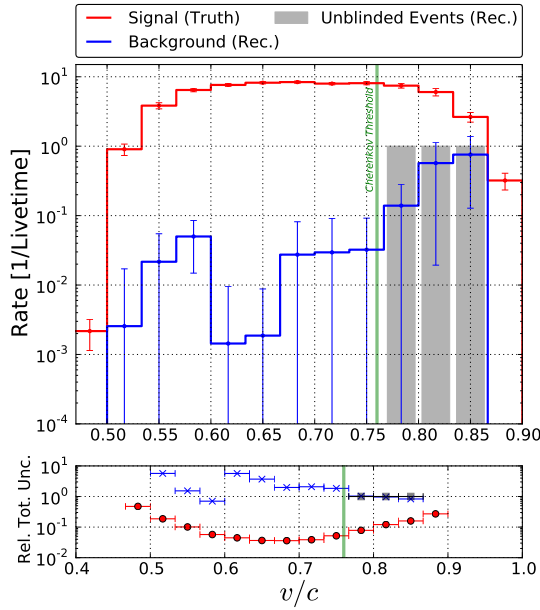
Figure 6.5: The velocity distribution for simulated background, simulated signal, and unblinded events. These are used for the calculation of the final limits. For simulated signal $v_{\text{MC}} < 0.9\,c$ is shown, for simulated background and unblinded events v_{proxy} is shown. Total uncertainties are dominated by the PV-error. Taken from [Pol16].
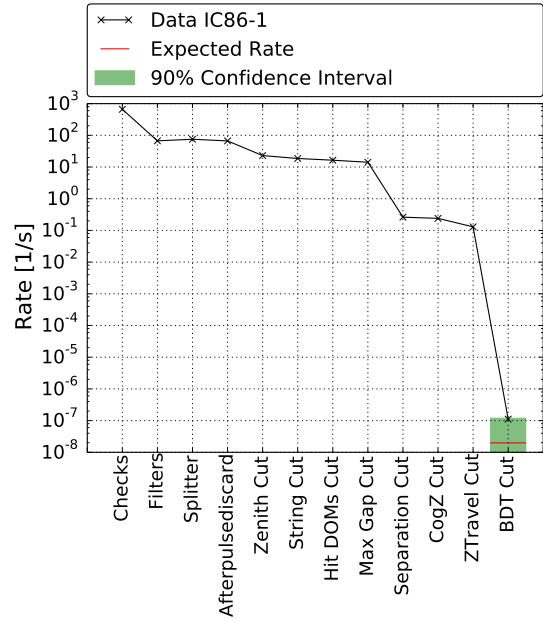
Figure 6.6: Efficiency of the cuts applied on Ice-Cube data. Many cuts improved data quality to prepare for reconstructions rather than reducing the event rate. The last cut is the most efficient one, followed by the cut on d_{Sep}. The only processing step that increased the number of events is the splitter. The average expected background rate is shown in red, the confidence interval in green.

limit of 3.61 events which takes the large uncertainties of the re-sampling method into account. Therefore, the events are considered to be background.

All events have reconstructed velocities above the Cherenkov threshold where the efficiency of the analysis is weaker. This might be a hint, that the trained pull-validation could be less reliable outside the training range. All events can be classified as vertical corridor events, as described in Ch. 5.2.3. These kind of events was estimated by pull-validation.

The second event could be a stopping track. The third event is through-going, however it might comprise of an additional cascade. The third track has the largest number of hit DOMs $n_{\text{DOM}} = 110$ and reconstructed photo-electrons $n_{\text{NPE}} = 595$. A magnetic monopole of arbitrary mass with the same position, direction of about 170°, and velocity of $0.83\,c$ would produce $n_{\text{DOM}} = 196 \pm 11$ hits by direct Cherenkov light in the detector according to executed simulations with parameters varying around the reconstructed values, see Fig. 6.4. Since the number of produced photons derived for direct Cherenkov light is not dependent on any unknown monopole parameter, but only on well-known electrodynamics, it is unlikely that this event is caused by a monopole with different parameters than assumed in simulation.
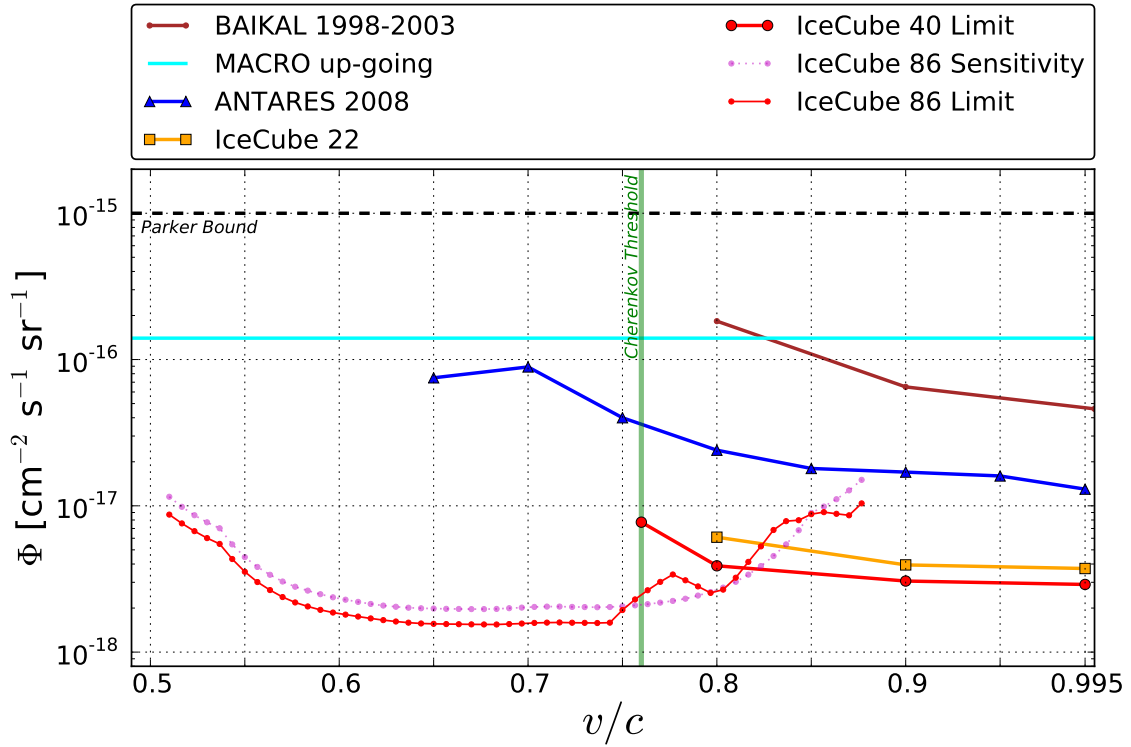
Figure 6.7: Sensitivities and limits compared to the analyses from MACRO [Amb02], BAIKAL [Ayn08], AMANDA [Abb10b], ANTARES [AM12], IceCube 22 [Abb13], and IceCube 40 [Pos13a, Pol16]. Taken from [Pol16].

6.3 Limits

The final limits are calculated as described in Ch. 5.4 using the distributions in Fig. 6.5. The results are shown in Fig. 6.7. The limits are compared with the limits of IceCube 40 [Pos13a, Pol16], MACRO [Amb02], and ANTARES [AM12] and exceed them up to a factor of 80. The values are given in Tab. E.1.

The limits are lower, i.e. better, than the sensitivities for many velocities since the expectation at these points was a floating point number between zero and one. The observed zero events at these velocities is therefore an under-fluctuation compared to the expectation.

Sensitivity studies performed with straight cuts, estimated a competitive sensitivity down to $\approx 0.6\,c$ [Obe12]. The usage of a multivariate method widened the velocity range down to almost $0.5\,c$ and up to $0.8\,c$.

These limits are calculated with the assumption of an isotropic monopole flux around the IceCube detector, so that it can be compared with other analyses. The consideration of the attenuation through Earth is explained in detail in [Pos13a] using Fig. 5.11.

7   Conclusion and outlook

In this work a search for magnetic monopoles with the IceCube neutrino telescope is described. Magnetic monopoles are predicted by various theories which go beyond the current standard model of particle physics. A large mass and charge compared to standard model particles are the characteristic properties for monopole detection. Due to that a monopole is highly ionizing and produces direct and indirect Cherenkov light when its velocity exceeds $0.76\,c$ or $0.45\,c$ respectively. Indirect Cherenkov light is produced by δ-electrons which are knocked off their atoms by the monopole.

The aim of this analysis was to focus on indirect Cherenkov light as detection principle to increase the parameter range of monopole searches with IceCube. To achieve that, theories about the monopole-electron cross section were studied. This led to the conclusion that a different cross section was used than in comparable analyses because it is more sophisticated using modern electrodynamics and therefore more likely to yield the correct values.

The assumptions about the monopole interaction with matter were implemented into an advanced simulation code using cutting-edge GPU technology. It was shown that exotic signatures can be isolated in IceCube data with existing and common tools which were extended further.

The challenge with insufficient simulation statistics of background events for the development of a significant analysis was dealt by developing the newly proposed pull-validation to an independent and tested method. For the first time this re-sampling method performed successfully in dealing with missing statistics in the order of more than one magnitude. Subsequently pull-validation is used in other analyses which face the same challenge.

Finally, this analysis produced the first IceCube limits for mildly relativistic monopoles which exceed limits from previous analyses by almost two orders of magnitude. Additionally the velocity range of IceCube was increased further than expected down to a velocity of $0.51\,c$. In spite of decades of unsuccessful searches for monopoles, "the existence of magnetic monopoles seems like one of the safest bets that one can make about physics not yet seen" [Pol04] since the theoretical predictions are built on very basic principles.

Future IceCube searches can take advantage of a more efficient event selection by using sufficient background simulation. Meanwhile the detector has taken data in full configuration for five years. Thus, future analyses can be based on five times the amount of data and enhance the chance of a detection. A newly proposed high energy extension of IceCube, called IceCube-Gen2 [Aar04], enables analyses to achieve better sensitivities, including searches for relativistic monopoles.
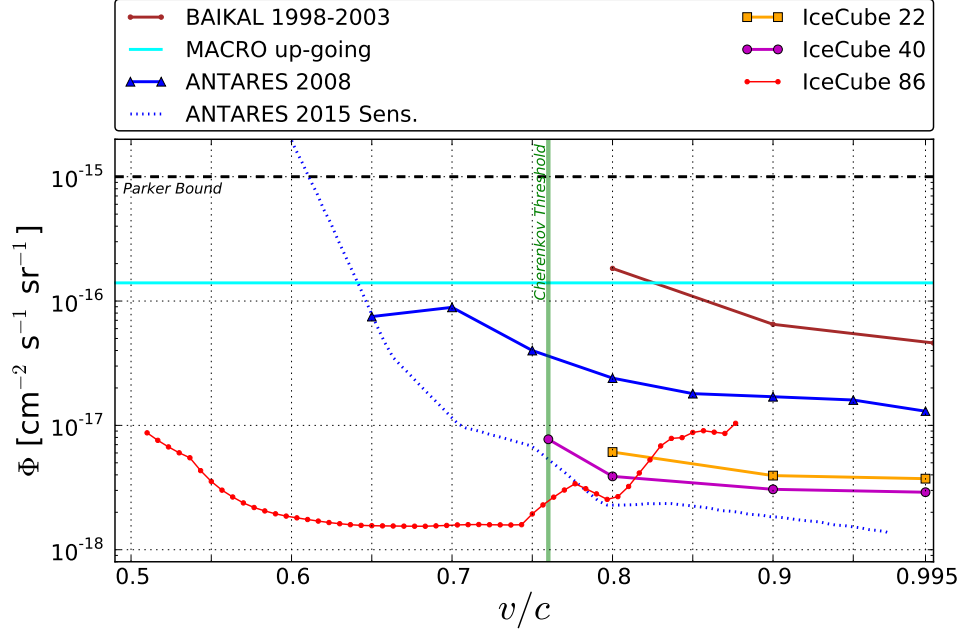
Figure 7.1: Sensitivity of an ANTARES analysis (dashed blue) [Boj15] covering a similar velocity range as done in this work (red) .

At other detectors there is currently a new search for magnetic monopoles using ANTARES data and producing sensitivities illustrated in Fig. 7.1 [Boj15].

In the context of this work luminescence, an unexplored detection principle for charged particles with ultra high kinetic energies, was disclosed, described in App. A.1. Further investigation of luminescence and the proposed construction of a low energy extension of IceCube, called PINGU [Aar14b], provides the feasibility of monopole searches at lower velocities. This could fill the gap between searches for relativistic and sub-relativistic monopoles in the velocity range of $0.1\,c$ to $0.5\,c$ with neutrino detectors.

Appendices

A   Further detection mechanisms

A.1   Luminescence light from Monopoles

Luminescence is the light emission from matter which occurs when excited electronic states are relaxed. It can be caused by chemical reactions, electrical energy, subatomic motions, or stress on a crystal. In ice there are three interesting mechanisms [Gro54]

- Thermoluminescence: Excited states in a crystal can last for an extended period of time. Heating enables the states to decay into lower-energy states while emitting a photon.

- Triboluminescence: It is supposed that during the fracturing of crystals, charges are separated. The discharging excites the surrounding matter leading to the emission of photons.

- Radioluminescence: Due to ionizing radiation (UV/X-ray, $\alpha/\beta/\gamma$-ray, heavy ions) passing through matter, electron transition and recombination processes within the outer electron shell of atoms lead to the emission of photons.

The terms *fluorescence* and *phosphorescence* are defined as the light emission due to spin-allowed and not-allowed electron transitions from the excited state. In the first case the excited state is instable and the decay time is very short. In the second case the excited state is meta-stable with a longer decay time.

The light yield of luminescence is weakened, i.e. *quenched*, when impurities in the substance absorb the emitted photons. This might also be the case when heating the substance [Che60]. However, impurities can also be used to increase the light yield. Luminescent substances for technical applications are usually crystals doped with other materials to enhance the glow time.

A.1.1   Luminescence of water-ice

For a long time it was assumed that the radioluminescence of water or water ice was either caused by impurities, to be thermoluminescence or triboluminescence, or to be Cherenkov light [Bel53]. The first detection of radioluminescence of pure water ice in the temperature range between $-170°$C and $-100°$C is described in [Gro52] and more detailed in [Gro54]. Early subsequent studies of this phenomena addressed different properties selectively, summarized in [Qui82].

The luminescent wavelength spectrum differs from the continuous Cherenkov spectrum by comprising of distinct peaks. These originate from electronic transitions in the atom or
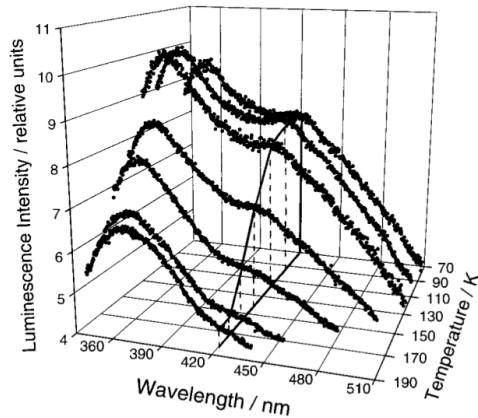
Figure A.1: Luminescent light yield dependent on wavelength and temperature. H_2O ice was irradiated with 260 nm UV-light. The peak at 420 nm becomes more prominent for lower temperatures. Taken from [Sel06].
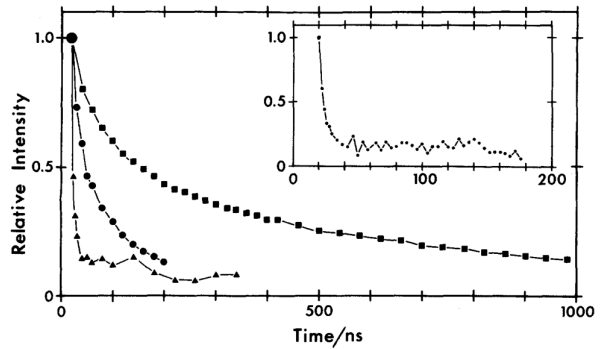
Figure A.2: Decay curves for three luminescence bands with wavelengths 280 nm (triangles), 380 nm (rectangles), and 550 nm (circles) which show an exponential shape. H_2O ice at 88 K was irradiated by electrons in saturating dose. Taken from [Tro86].

substance. Using ionizing radiation can excite electronic states which cannot be reached using light due to forbidden transitions or insufficient provided energy [Ste72]. For example, different wavelength were measured and illustrated in Figs. A.1 and A.2 for UV- and β-radiation. The measurable parameters per transition are

- wavelength proportional to the energy freed in the electronic transition (Fig. A.1)

- light yield dependent on the amount of excited states

- decay time dependent on the stability of the excited state (Fig. A.2)

Due to the different results from previous studies the transitions, and so the measurable parameters, vary with different

- type of ionizing radiation [Qui82]

- luminescent substances [Ste75]

- structures of the substance [Qui82]

- temperatures (Fig. A.1) [Qui82]

- history of the sample regarding warming/cooling and irradiation [Tro86]

Neither a comparison of these measurements is possible nor an extrapolation to different conditions. To use radioluminescence as a method for particle detection, measurements under the given conditions have to be performed. To give an example, the measured

IX
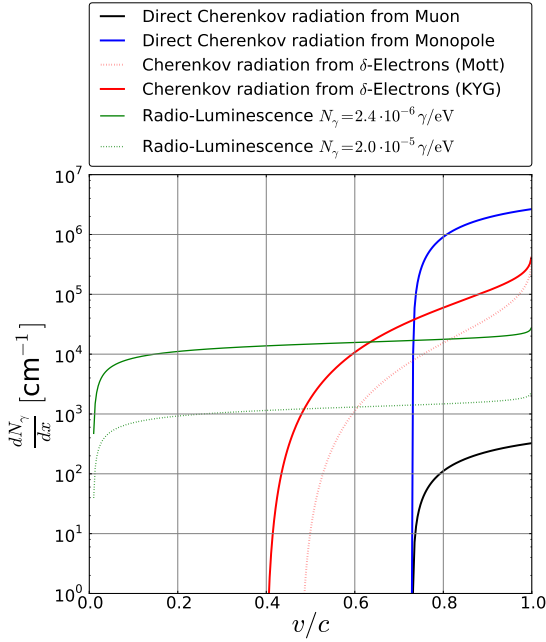
Figure A.3: Light yield of radioluminescence using two measurements from Refs. [Qui82] (solid green) and [Ayn08] (dashed green) in comparison to direct and indirect Cherenkov light. It is assumed that all light is emitted instantly. Decay times in the order of $\gtrsim 1\,\mu$s would reduce the light yield due to the time window of the IceCube triggers.
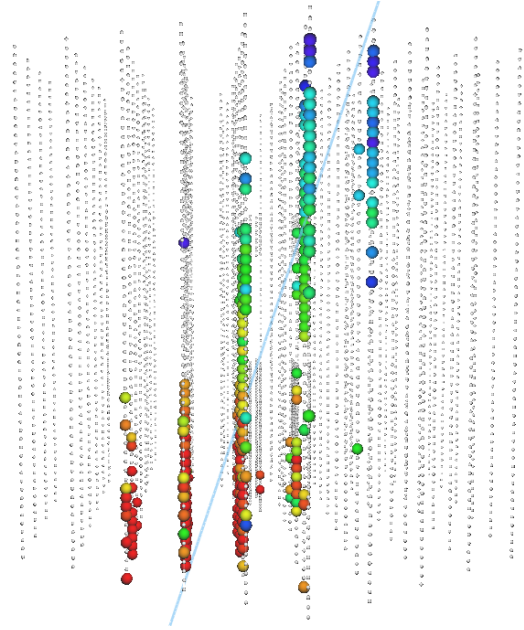
Figure A.4: Simulation of the signature of a monopole with $v = 0.5\,c$ producing luminescence light according to the light yield given in Ref. [Qui82]. The blue line denotes the simulated monopole track. Hit DOMs are colored but not scaled with recorded charge.

differential light yield dN_γ/dE in water and water-ice under different conditions ranges from $2 \cdot 10^{-5}\,\gamma/$eV [Ste72] over $(2.4 \pm 0.6) \cdot 10^{-6}\,\gamma/$eV [Qui82] to $2 \cdot 10^{-7}\,\gamma/$eV [Ayn08]. The light yield dN_γ/dx is given in terms of the energy loss of ionizing radiation in matter per unit path length dE/dx so that the measurable luminescence is

$$\frac{dN_\gamma}{dx} = \frac{dN_\gamma}{dE} \cdot \frac{dE}{dx} \tag{A.1}$$

This is illustrated in Fig. A.3 employing the energy loss of a magnetic monopole. These values can also be reached by $5\,$MeV α-particles.

A.1.2 Neutrino-detectors and luminescence of monopoles

The benefit of using luminescence light as a detection signature for magnetic monopoles is that it does not require any additional assumptions of the monopole properties besides its energy loss. In comparison the ability to catalyze proton decay is not given in every theory describing magnetic monopoles. It is illustrated in Fig. A.3 that the light yield from luminescence could be visible for the IceCube sensors as it exceeds the light yield of a muon. Therefore IceCube could be sensitive to luminescent monopole signatures down

to a velocity of $0.1\,c$ if sufficient trigger and filter are developed to account for the small velocity and long decay time. Since there are currently IceCube limits for velocities of $v < 0.1\,c$ and $v > 0.51\,c$ this would make a new range accessible for monopole searches.

It was first proposed by BAIKAL to use luminescence light in a search for magnetic monopoles with a neutrino detector [Ayn08][48]. In this reference an unpublished search of this type with the BAIKAL detector is referenced [Tro92]. According to private conversations, this search uses the light yield given in [Ayn08] which was measured by BAIKAL collaborators from Irkutsk university in 1989 with 5 MeV α-particles in water. The corresponding report is not available at Irkutsk.

Due to hints in the other two references, the measurement was performed at the depth of the Baikal lake to shield from cosmic rays. An α-source must have been positioned in the proximity of a photomultiplier tube. The range of α-particles in water is about 2.5 mm. If the particle deposits a typical value of 5 MeV in the medium and the light yield is given by $dN_\gamma/dE = 2 \cdot 10^{-7}\,\gamma/\text{eV}$ [Ayn08], one photon per particle would be emitted. The luminescent photons are emitted isotropic around the α-particle. If the photomultiplier tube covers 10 % of the space angle and if a typical value of 1000 α-particles are emitted per second, 100 photons per second would reach the photomultiplier tube. A common acceptance of photomultiplier tubes is 20 %, thus 20 photons per second could be measured according to this rough calculation.

To use luminescence light for monopole searches with IceCube, new measurements are needed which account for the particular ice temperature and structure in IceCube. A measurement as described in the last paragraph could only be performed when a drilling core of the Antarctic ice was available. Otherwise the effect of temperature and structure of the ice on the light yield has to be studied in laboratory. This would have the advantage that artificial sources of ionizing radiation with higher energies could be used to reduce experimental uncertainties.

Since 2013 IceCube measures astrophysical neutrino secondaries [Aar13a, Rae15] which are particles depositing energy of up to 2 PeV in ice. In these events luminescence light must be produced, however exceeded by Cherenkov light. Since the latter is emitted instantly, the contribution of luminescence light could be separable when analyzing the waveforms recorded by IceCube's photomultiplier tubes. The total light yield, from all electronic transitions summed up, and the total decay distribution could be the result. The distribution's shape could be fit with several exponential functions to find the decay times of different transitions.

The measurement of luminescent parameter of IceCube ice is not only interesting for monopole searches. The energy reconstruction of high energetic events caused by standard model particles is usually done by analyzing the brightness of an event signature assuming instant light emission. Depending on the light yield and decay time, the presence of luminescence light could effect the accuracy of this reconstruction. Additionally luminescence light could still be visible after the trigger window of ten microseconds. Therefore, it could

---

[48]Another proposal for monopole searches suggests the usage of luminescence in air by monopoles [Wic03]. This assumes the existence of monopoles which interact via the strong force. Then monopoles could be detected using air fluorescence detectors.
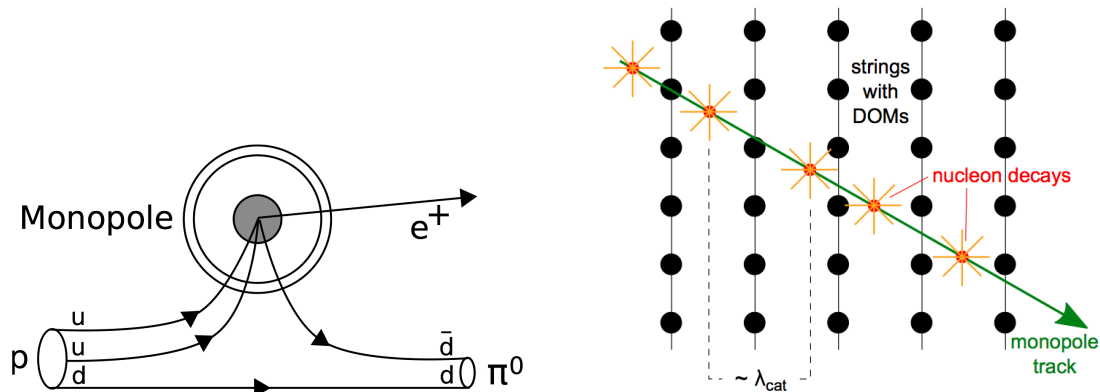
Figure A.5: Proton decay into a neutral pion and a positron, catalyzed by a GUT monopole (left). Construction of a monopole track-like signature out of cascades (right). Taken from [Aar14d].

be one of the unknown sources of noise in the detector (see Ch. 1.2.3). This is particularly the case for luminescence light caused by the UV-fraction in Cherenkov light which is supposed to have decay times in the order of seconds [Sel06]. This could be checked by investigating the recorded events which succeed the astrophysical neutrino events in time.

A.2 Nucleon Decay

In the standard model of particles the proton is a stable particle. However, in 1982 Rubakov proposed that monopoles catalyze nucleon decay depending on the GUT theory [Rub82]. One year later, Callan simplified his ansatz and suggested the usage for monopole searches [Cal83].

The monopole structure, illustrated in Fig. 2.3, comprises of a region with unbroken GUT symmetry which is a state of indefinite baryon and lepton number. Therefore, monopole interactions with standard model particles might violate conservation of baryon number and the rate and cross section are in the order of the strong interaction. The effect depends only on the confinement scale and fermion masses, not on other predicted values of GUTs. Only GUTs which additionally predict very high monopole masses of $M > 10^{13}$ GeV comply with these restrictions.

When a monopole and a proton are in close proximity a valence quark reacts with the monopole turning into two antiquarks and a positron. The positron gains kinetic energy of about 100 MeV instantly leaving the monopole core [Cal83]. The exotic quark state might decay into pions, illustrated in Fig. A.5 (left). Depending on the interaction cross section σ_0 and the speed of the monopole this happens on the scale of centimeters or meters along a monopole track through matter [Rub88]

$$\sigma_{\text{cat}} = \begin{cases} \frac{\sigma_0}{\beta} & \text{for } \beta \geq \beta_0 \\ \frac{\sigma_0}{\beta} \cdot F(\beta) & \text{for } \beta < \beta_0 \end{cases} \tag{A.2}$$

where F is a correction factor for low velocities and the threshold speed β_0 and F depend on the given nucleus. The positron and pion produce an electromagnetic and hadronic
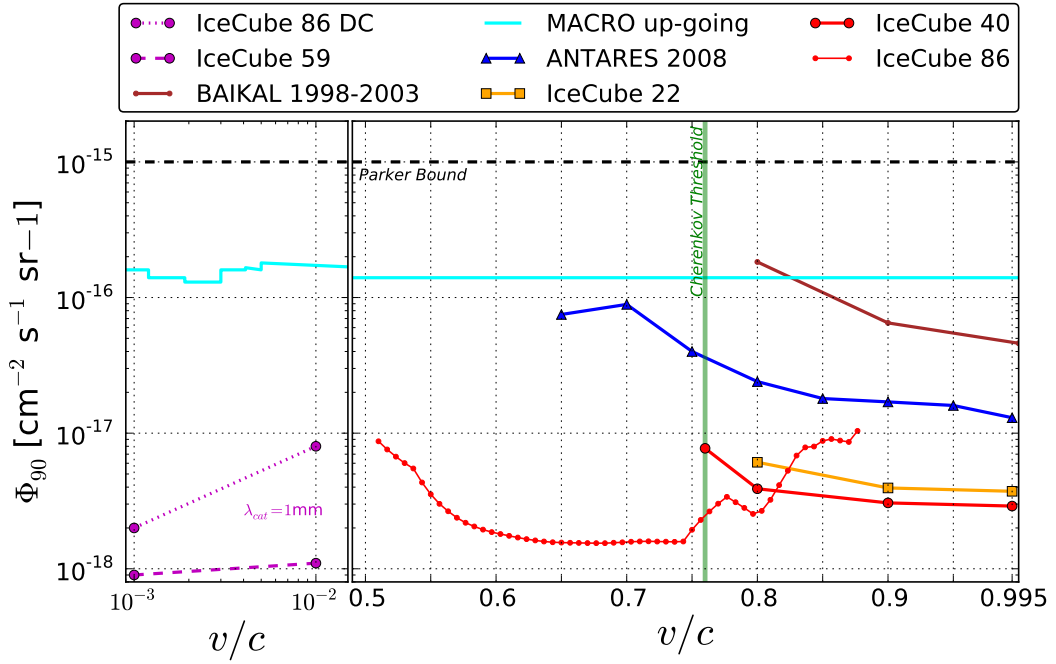
Figure A.6: IceCube's limit for non-relativistic magnetic monopoles (left) in comparison to limits for relativistic magnetic monopoles.

cascade, as described in Ch. 1.1.1, in which the subsequent particles are relativistic and produce Cherenkov light.

The signature of a monopole of velocity $< 0.1\,c$ catalyzing proton decay would be a track of $1\,\mathrm{GeV}$ cascades in the detector, illustrated in Fig. A.5 (right). The brightness of this track depends on the density of cascades, i.e. the cross section.

Two searches for these non-relativistic and heavy monopoles have been performed with IceCube [Aar14d]. For one of these analyses a special trigger was created which is capable of recording events up to a time length of $10\,\mathrm{ms}$. The background of these searches are thousands of muons which pass the detector in this time window. No monopole candidate was found, however the most stringent limits on the catalysis cross section have been set, see Fig. A.6.

B   Check of the detected PeV track

In the IceCube data of season 2014 an event was found which has an extremely bright signature with reconstructed photo-electrons $n_{\mathrm{NPE}} \approx 1.3 \cdot 10^5$, see Fig. 4.10 (right). The regarding analysis searched for a diffuse flux of astrophysical muon neutrinos [Rae15]. Certain parameters of this event were reconstructed by simulating comparable signatures. With that the directional resolution of the event was restrained below one degree. However, the energy reconstruction of tracks inherits larger uncertainties since only part of the energy loss is recorded (in opposite to cascades which can be completely contained in the detector volume). The lower limit of the reconstructed energy deposited inside the detector volume is $2.6 \pm 0.3 \, \mathrm{PeV}$.

During this work it was checked with the available tools if the event could be caused by a monopole. The monopole likelihood reconstructs a velocity consistent with the speed of light. The highest monopole velocity which can be simulated with current tools is $0.99 \, c$. This was used to simulate a monopole along the reconstructed track. Direct and indirect Cherenkov light production is taken into account but radiative energy losses were not implemented in simulation.
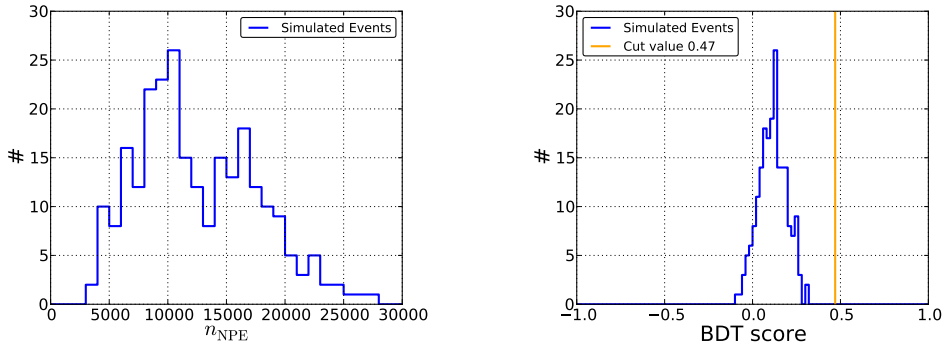
Figure B.1: Reconstruction results of simulated events. The simulated events are one order of magnitude dimmer than the considered event (left). The event selection of this work does not select these kind of monopole signatures (right).

The number of reconstructed photo-electrons for the simulated monopoles is more than one order of magnitude lower compared to the considered event, see Fig. B.1 (left). The event selection of this work was applied on the detected event and on the simulated events. As shown in Fig. B.1 (right) the event selection is not sensitive to this kind of signatures, therefore the detected event was not selected either.

The energy loss of the particle in dependence of the position on the track was also reconstructed, see Fig. B.2 and the visualization in Fig. B.3. The structure in the simulated monopole energy loss is related to the string distance of $125 \, \mathrm{m}$. Apart from that the energy loss is almost homogeneously distributed along the track. The energy loss distribution of the detected event comprises at least two major energy losses which can be identified as two cascades (see Fig. 4.10 right). They probably originate from stochastic energy losses due to radiative interaction with matter. They should dominate the light production for
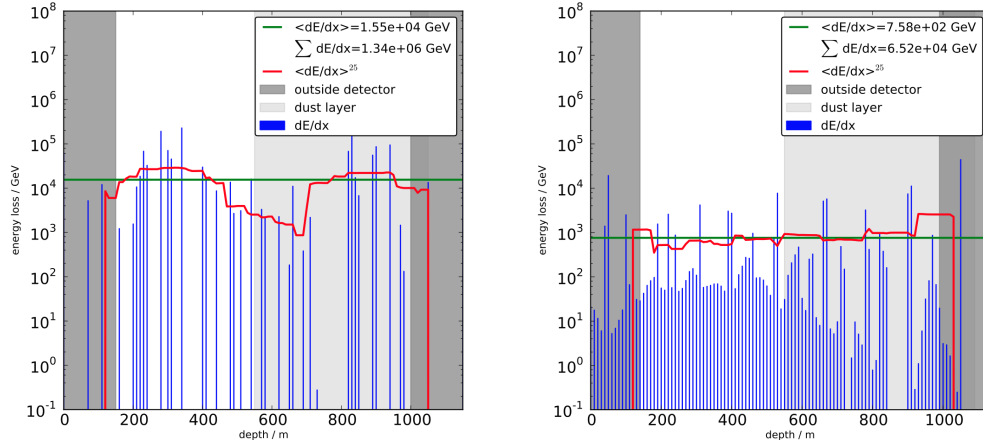
Figure B.2: Reconstructed energy losses (blue) along the track for the detected event (left) and one simulated event (right). The green line denotes the mean value. The red curve shows a sliding mean using 25 values each representing 10 m track length. The dark grey shades are the borders of the detector volume. The light grey shade denotes the dust layer.

monopole energies of $\gamma > 10^3$, compare Ch. 3.2.3 and Fig. 3.9. However, this kind of energy losses was not simulated for monopoles since they are not implemented to date.

In conclusion the signature of the detected event is inconsistent with monopoles of velocities $< 0.99\,c$. It cannot be excluded that the signature originates from a faster monopole producing stochastic energy losses. However, it is more likely that the signature originates from a muon since the energy loss distribution is consistent with simulations of muons.
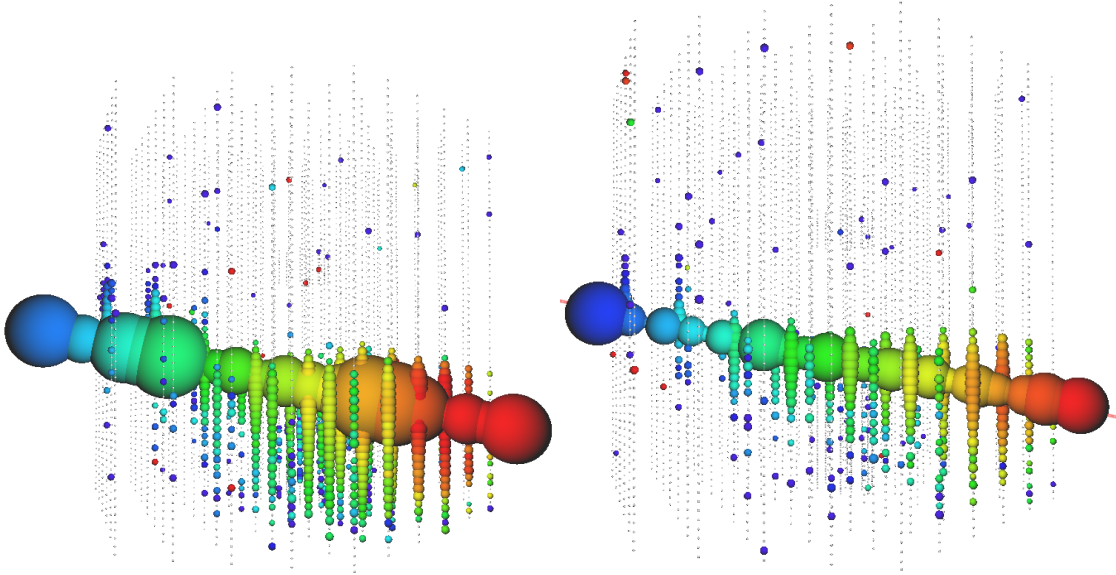
Figure B.3: Visualization of the energy losses. The detected event is shown on the left. The radius of the hit DOMs was scaled down in comparison to the rest of this work. The spheres along the track visualize the positions, times and amounts of energy losses denoted by position, color and radius. On the left a simulated event is shown using the same scales.

XV

C   Analysis methods

C.1   Event selection with cuts

Event selection is the process to separate signal from background with the help of recon-
structed variables. The simplest method to define selection criteria is to perform rect-
angular cuts (also called cut-and-count selection). Variables are identified in which the
distributions show different shape in background and signal. A cut is chosen due to a
particular selection criteria. This might be the optimization for a good model rejection
factor (Ch. 5.4.1) or a grade of pureness in the sample.

Every variable distribution and the corresponding cut have to be investigated thoroughly
to prevent unintentional effects. This time consuming step usually reduces the number of
cuts performed per event selection.

The chosen variables span a multidimensional space and the cut restrict this space to
certain ranges, i.e. a multidimensional rectangular space. A low number of cuts enables
simple interpretation of the final result of an event selection. However, the cuts are usually
investigated in one or two dimensions. Relations in more than two dimensions are not
investigated.

C.2   Boosted decision tree

A decision tree (or classification tree) is a
machine learning algorithm which can be
used for event selection. The goal of one
decision tree is to build a model which pre-
dicts the signal-ness of an event based on
the input variables. The model, illustrated
in Fig. C.1, is built by providing *labeled*
data, i.e. all events are labeled as back-
ground or signal and the algorithm can use
this information. The tree algorithm ap-
plies binary cuts on the data, choosing the
best discriminating variable per node. The
final leaf of a tree are labeled as signal
or background depending on the majority
type of events contained there. When in-
serting un-labeled data into a trained tree
the majority of signal events should end in
signal-leafs.
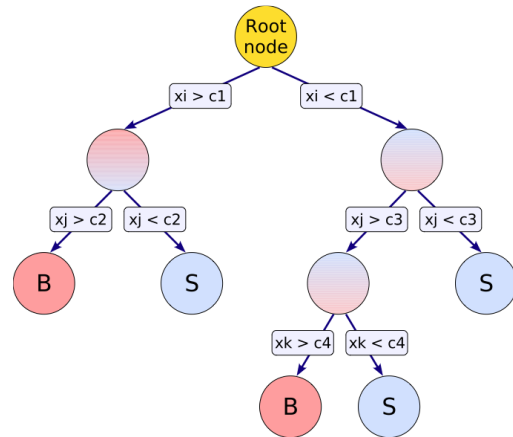
Figure C.1: Schematic view of one decision tree.
Taken from [Hoe13].

A decision tree can be overtrained when too many model parameters are trained on too
few data. This can be avoided by restricting the depth of a decision tree to a certain
number of nodes. To keep the discriminating power many decision trees are built and the
results are combined. A variation in the decision trees is gained by re-weighting the data,
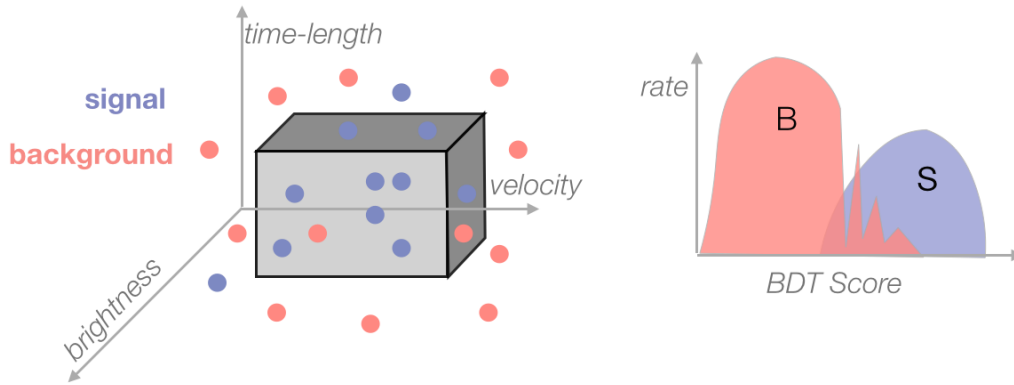
Figure C.2: Illustration of the principle of one branch of one tree of a BDT in three dimensions. On the left it is shown that within the branch a rectangular shape is cut into the 3-dimensional parameter space which is spanned by the BDT variables. The BDT algorithm converts the survival probability of an event regarding these cuts into a *score*. As shown on the right, background and signal distributions should be well separated.

otherwise every tree would make the same decisions. The trees are weighted according to their success in classifying the data which is called boosting.

When all trees are built, i.e. trained, on the first part of the labeled data, they are applied on the second part. In this way the model is tested. Every event gets a score between -1 and $+1$ which classifies it in regard of its signal-ness. The score is the weighted sum of the purities of the final nodes in the forest.

One decision tree is comparable to an event selection with rectangular cuts, as shown in Fig. C.2, although combination of a large number of trees complicates the interpretation. The BDT score is the mapping of the multidimensional space spanned by input variables into one dimension. This leads to a physically meaningful distribution if the input variables cover the real phase space of the signal.

The data, which is to be classified by a BDT, is usually prepared by some cuts. This is also done in this analysis and the reasons for that are given in Chs. 5.1.3 and 5.2.2. In this analysis one BDT consists of 300 BDTs with a depth of 3 nodes[49].

C.3 Resampling methods

Bootstrapping and cross-validation are resampling algorithms from which pull-validation was inspired. They can be used to estimate the precision of sample statistics by using subsets of the available data.

---

[49]For all other parameters of the IceTray module *pyBDT* the default values are chosen: If only a randomly selected number of variables can be chosen per node, one speaks of a decision forest. It is also possible to choose randomly a fraction of events to train each tree. Both options were not used in this work. The number of cuts, which should be tried at one node, was not set. No minimum number of events for the final leaf was set. The beta parameter of the used AdaBoost algorithm was set to 0.7. Pruning (cutting back of very deep trees) is only sensible for single trees without restriction of depths [Yan05].
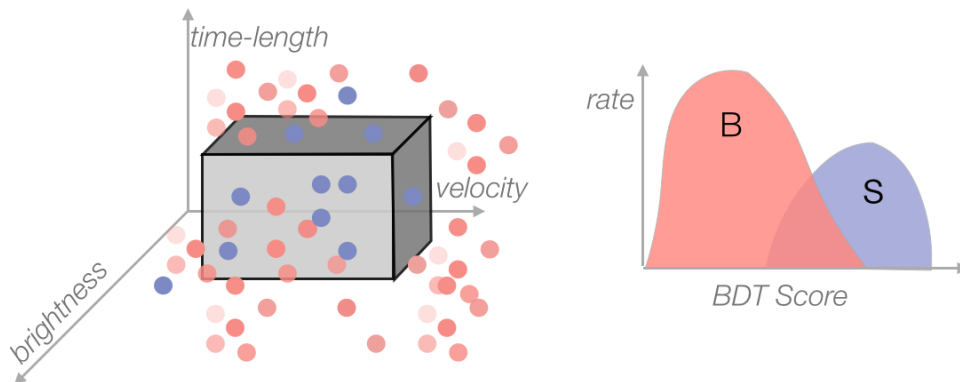
Figure C.3: Illustration of the principle of resampling the training set of a BDT. Different training sets give different background points (different shades of red dots) which fill up the parameter space more dense than one training set alone, shown in Fig. C.2. On the right plot, this leads to a smoother tail of the background distribution near the signal region.

Given is a sample with N data points. In a bootstrap data points are randomly chosen for a sub-sample [Efr79]. One point can be chosen several times for the same sub-sample as it is always laid back into the sample, so called sampling with replacement. Eventually the sub-sample also comprises $n = N$ data points. If N is sufficiently large the bootstrap is repeated N_R times (typically $N_R > 1000$) without producing identical sub-samples. The calculation which was supposed to be done on the original sample, is then done on every sub-sample, e.g. one BDT is trained on each sub-sample and applied on the events which were not chosen for this sub-sample. Therefore, N_R different results are calculated. The variation of these results based on the sub-samples is assumed to reflect the uncertainty of the original sample.

For k-cross-validation the sub-samples are prepared by dividing the original sample with N data points into k disjunct samples with N/k data points [Lac68]. A sub-sample is then built of $(k-1)$ small samples. Then it comprises $n = N \cdot (k-1)/k$ data points. A number of k different sub-samples can be built. These sub-samples with n data points are used for training. The remaining $N - n$ data points are used for testing.

Both bootstrapping and cross-validation are well tested resampling methods. The difference in pull-validation is that the number of data points in the sub-sample n is significantly smaller and that the points are not chosen with replacement. Therefore, pull-validation introduces a larger variation between the sub-samples which enables on to deal with a larger lack of statistics in the original sample. However, this also makes the method less reliable. This is why all the checks, described in Ch. 5.2 are necessary.

D   Computational methods

D.1   Statistics

In this work *statistics* refers to the statistical error of a counting experiment, i.e. the Poissonian error. The Poisson distribution is a discrete probability of a certain number of events n occurring in a fixed time interval. The probability mass function is given by

$$P(n) = \frac{\lambda^n e^{-\lambda}}{n!} \tag{D.1}$$

where λ is the expected number of events and also the variance. An experiment which counted N events has therefore a statistical error of

$$\sigma = \sqrt{N} \tag{D.2}$$

Higher statistics denotes a lower statistical error, i.e. a higher number of events N.

D.2   Generation of random numbers giving a power law

Given a distribution I, for example in Fig. 4.7, which depends on the velocity v' and follows a power law $k \cdot v'^{-\gamma}$ with the constant k and the spectral index $\gamma \in \mathbb{N}$ within the interval $[v_0, v_1]$

$$I(v') = k \cdot v'^{-\gamma} \tag{D.3}$$

With standard software libraries one can only sample from a uniform distribution. However, these values can be used to get random numbers of a power law. First the cumulative function is calculated

$$U(v) = k \cdot \int_{v_0}^{v} v'^{-\gamma} \, dv' = \begin{cases} k \cdot \ln \frac{v}{v_0} & \text{for } \gamma = 1 \\ \frac{k}{1-\gamma} \left(v^{1-\gamma} - v_0^{1-\gamma} \right) & \text{for } \gamma \neq 1 \end{cases} \tag{D.4}$$

and then its inverted function

$$v(U) = \begin{cases} v_0 \cdot e^{\frac{U}{k}} & \text{for } \gamma = 1 \\ \left(\frac{1-\gamma}{k} U + v_0^{1-\gamma} \right)^{\frac{1}{1-\gamma}} & \text{for } \gamma \neq 1 \end{cases} \tag{D.5}$$

The variable U can then be replaced by the uniform distribution with values between 0 and $U(v_1)$ to get the required velocity distribution v. To re-weight this power law to a uniform distribution the individual weight for an event w is

$$w'(v) = \frac{v^{\gamma}}{k} \tag{D.6}$$

These weights require normalization by division with the sum of all weights $W = \sum_v w'(v)$. In IceTray, the monopole-generator module sums up all weights while processing and gives the value W after finalizing the simulation. The normalization cannot be done on the fly with IceTray and has to be applied afterwards. W must account for all simulated monopoles, not only the events interacting in or near the detector volume and causing a trigger.

D.3 Weighting

In simulations the sum of generated events mirrors real data, particularly their spectra. The term *spectrum* is usually referring to a distribution of flux versus energy. However, weighting can also be used for other distributions, such as velocity (Ch. 4.2.1). The simulated rate, i.e. number of events per bin, is usually not reflecting any physics due to two reasons

- The required spectrum is steep or ranging over several orders of magnitude (compare Figs. 4.1 and 4.2). Given, for example, a distribution of a rate I depending on a variable x in the shape of a power law with spectral index $-\gamma$

$$I(x) = k \cdot x^{-\gamma} \tag{D.7}$$

  Then, $N = \sum_{x=x_1}^{x_2} I(x)$ events are simulated as described in App. D.2. Assume two different spectral indices $\gamma_1 = 2$ and $\gamma_2 = 3$. Then, the number of events at the end of the spectrum, simulated with $x_2 = 10^3$, is $10^{(\gamma_2 - \gamma_1) \log_{10} x_2} = 10^3$ larger for γ_1 than γ_2. A simulation with a lower spectral index would therefore lead to more statistics (App D.1) at higher values.

- The spectral index is often not a constant, e.g. for the cosmic ray energy spectrum. For the individual primaries, the measurement of the spectral index inherits large uncertainties. Thus, different models of this spectrum are generated. With weighting a simulation can be adjusted to several models without the need to re-processing.

Therefore usually a spectrum is simulated which is harder than what is eventually required. As explained in App. D.2 a spectral weight w consists of an individual weight w', dependent on the ratio of the shapes of the simulated I_{sim} and required I_{final} distributions

$$w'(x) = \frac{I_{\text{sim}}(x)}{I_{\text{final}}(x)} \tag{D.8}$$

as well as the *normalization weight* $W = \sum_x w(x)$

$$w = \frac{w'}{W} \tag{D.9}$$

The weighting is closely related to statistics. The statistics of a simulation with N events can be given as a livetime T. Without any weighting this is the time interval which would have been needed to record N events with the detector. Assume that N_{sim} events are simulated and weighted to N_{final} events. For example 9000 simulated events with spectral weight $w = 10^{-3}$ represent $N_{\text{final}} = 9$ events. The relative statistical error of the unweighted events is

$$\frac{\sqrt{N_{\text{final}}}}{N_{\text{final}}} = \frac{1}{3} \tag{D.10}$$

The value for simulated events is calculated using the weights

$$N_{\text{sim}} = \sum_i w \tag{D.11}$$

The error of this is given by Gaussian error propagation from the relative error

$$\frac{\sqrt{\sum_i w^2}}{\sum_i w} \approx 0.01 \tag{D.12}$$

Due to weighting the relative statistical error has been reduced. The number of unweighted events to achieve this would be

$$\frac{1}{\sqrt{N_{\text{final}}}} = \frac{\sqrt{\sum_i w^2}}{\sum_i w} \quad \Rightarrow \quad N_{\text{eff}} = \left(\frac{\sum_i w}{\sqrt{\sum_i w^2}}\right)^2 \quad \Rightarrow \quad N_{\text{eff}} \approx 10000 \tag{D.13}$$

Then the effective livetime T_{eff} is the time needed to observe at natural rate to get the same relative error as in simulation

$$T_{\text{eff}} = N_{\text{eff}} \left(\frac{T}{N_{\text{final}}}\right) \approx 10^6 \, s \text{ with } T = 900 \, \text{s} \tag{D.14}$$

As $w = N_{\text{final}}/T$ the final equation is

$$T_{\text{eff}} = \frac{\sum_i w}{\sum_i w^2} \tag{D.15}$$

Obviously, this number cannot be calculated when no simulated event is retained after a cut. Due to weighting the effective livetime is dependent on the variable x.

The distribution of weighted events is illustrated as a histogram of the data with the rate on the y-axis. The rate per bin R_b is then the sum of all weights w_b of the events which fall into this bin $b =]x_1, x_2]$

$$R_b = \sum_{x > x_1}^{x_2} w_b(x) \tag{D.16}$$

The error of this rate is due to the Gaussian error propagation

$$\sigma_{R_b} = \sqrt{\sum_{x > x_1}^{x_2} w_b^2(x)} \tag{D.17}$$

The best way to apply this is to first calculate the distribution's histogram with weights w_b and a second time with weights w_b^2. The square-root of the values of the second histogram can then be used for the error-bars. If the histogram is normalized, i.e. all bin rates are divided by the ratio of the number of all events and the bin-widths $\sum w/(x_2 - x_1)$, the bin error is $\sigma_{R_b}/\sum w/(x_2 - x_1)$.

D.4   Plotting angular distributions

In this analysis isotropic distributions of monopoles are simulated. To check the success the zenith and azimuth angles are plotted in Fig. 4.7. In spherical coordinates, the radius and the second angle are fixed. The angle is sliced into equal bins. Implicitly the space angle of the bin is drawn. The differential space angle $d\Omega$ is given by

$$d\Omega = \sin\theta \, d\theta \, d\phi \tag{D.18}$$

Bins of the horizontal angle (azimuth) ϕ are slices in a sphere. The differential space angle is integrated

$$\Omega \propto \cos\theta \cdot \phi \tag{D.19}$$

which shows that the space angle is proportional to the azimuth angle. Bins of the vertical angle (zenith) θ have a more complicated form, smaller at the poles (near 0 or 180°) and larger at the equator, illustrated in Fig. D.1. Despite an isotropic distribution in zenith the final distribution would not be uniform. To achieve that the cosinus of zenith has to be drawn as this is proportional to the space angle.
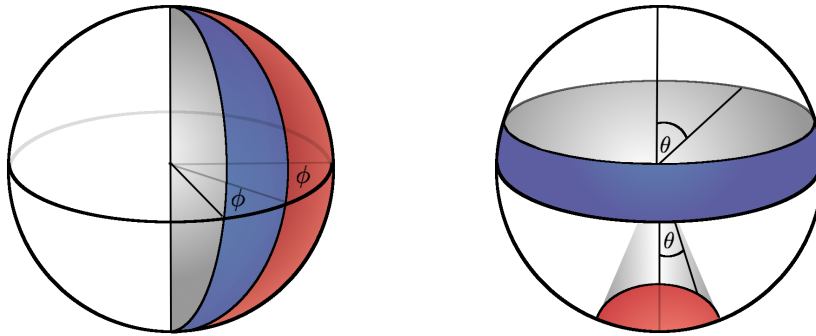
Figure D.1: Angular bins in spherical coordinates or equal size. The surfaces (blue and red) of the azimuthal slices (left), i.e. the space angles, are equal. The more complicated forms of zenith bins are shown on the right. These are a cone with red surface and an inverted cone with blue surface. For illustration purposes the angles are used slightly different than defined in Fig. 1.2.

E   Further plots and tables

E.1   Values of the final limit

Velocity v/c	$\Phi_{90\%}/10^{-18}$ cm^{-2}s^{-1}sr^{-1}	Velocity v/c	$\Phi_{90\%}/10^{-18}$ cm^{-2}s^{-1}sr^{-1}	Velocity v/c	$\Phi_{90\%}/10^{-18}$ cm^{-2}s^{-1}sr^{-1}
0.510	8.71	0.590	1.94	0.737	1.58
0.517	7.58	0.597	1.86	0.743	1.59
0.523	6.71	0.603	1.80	0.750	1.94
0.530	6.02	0.610	1.75	**0.757**	**2.29**
0.537	5.49	0.617	1.70	0.763	2.65
0.543	4.33	0.623	1.65	0.770	3.02
0.550	3.54	0.630	1.62	0.777	3.39
0.557	3.01	0.637	1.59	0.783	3.10
0.563	2.66	0.643	1.57	0.790	2.81
0.570	2.38	0.650	1.56	0.797	2.54
0.577	2.18	0.657	1.56	0.803	2.67
0.583	2.05	0.663	1.55	0.810	3.23
0.590	1.94	0.670	1.55	0.817	4.14
0.597	1.86	0.677	1.55	0.823	5.28
0.603	1.80	**0.683**	**1.54**	0.830	6.84
0.610	1.75	0.690	1.56	0.837	7.85
0.617	1.70	0.697	1.57	0.843	7.97
0.623	1.65	0.703	1.58	0.850	8.77
0.630	1.62	0.710	1.59	0.857	9.05
0.637	1.59	0.717	1.59	0.863	8.82
0.577	2.18	0.723	1.59	0.870	8.61
0.583	2.05	0.730	1.58	0.877	10.39

Table E.1: Values of the final limits. Bold numbers show the minimal flux limit and the flux limit at the Cherenkov threshold.

E.2   Unblinded events

	Event 1	Event 2	Event 3
Run	118191	118704	119352
Event	41572632	70730573	32762119
Filter	(SDST) Muon	(SDST) Muon SDST LowUp	(SDST) Muon
Split	1	1	2 (after-pulse)
BDT score	0.507	0.491	0.536
$n_{\mathrm{DOM}_{100}}$	33	28	77
$\bar{s}$ [m]	47.5	37.5	85.3
t_{Gap} [ns]	418	468	290
$d_{\mathrm{Gap}_{100}}$ [m]	163.9	101.2	67.5
d_{Sep}[m]	746.8	447.4	623.6
$\bar{s}_{\mathrm{NPE}}$[m]	19.9	9,5	63.8
$n^{*}_{\mathrm{DOM}_{50}}$	16	26	18
z_{travel}[m]	289.8	201.5	327.2
z_{pattern}	16	14	11
$n_{\mathrm{DOM}_{50}}$	21	23	32
$n_{\mathrm{DOM}_{100}}$	33	28	77
v_{proxy}/c	0.84	0.78	0.83
k_{100}	0.29	0.16	0.14
t_{w} [ns]	106.4	44.2	24.2
t [ns]	3921	3086	3953
$\bar{z}_{\mathrm{DOM}}$ [m]	-157.8	-219.9	-39.8
z_{COG} [m]	-324.1	-291.3	30.8
v^{M}_{LLH}/c	1.01	1.00	0.94
r^{M}_{LLH}	7.37	7.17	7.35
r^{μ}_{LLH}	6.97	6.92	7.33
θ_{iLF} [rad/degrees]	2.94 / 168.4	3.01 / 172.4	3.01 / 172.5
θ_{LLH}	2.95 / 168.9	2.99 / 171.1	2.99 / 171.2
n_{String}	5	5	8
n_{DOM}	35	31	110
n_{NPE}	84.4	132.9	594.9

Table E.2: Parameters of the unblinded events

E.3 Pre-cuts for pull-validation

The cuts, which prepare the data for pull-validation, are described in Tab. 5.4. The according variable distributions are shown in Figs. 5.4, 5.5 as well as in Figs. E.1 to E.3.
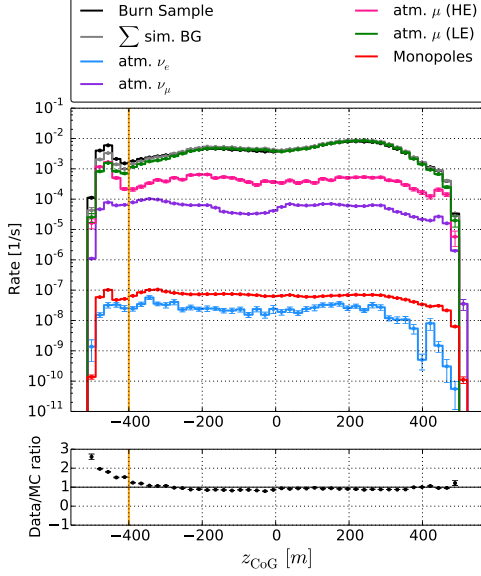
Figure E.1: Cut on $z_{\mathrm{CoG}} \geq -400\,\mathrm{m}$ intended to reduce the discrepancy between data and background simulation. These are bright horizontal tracks which pass slightly below the bottom of the detector.
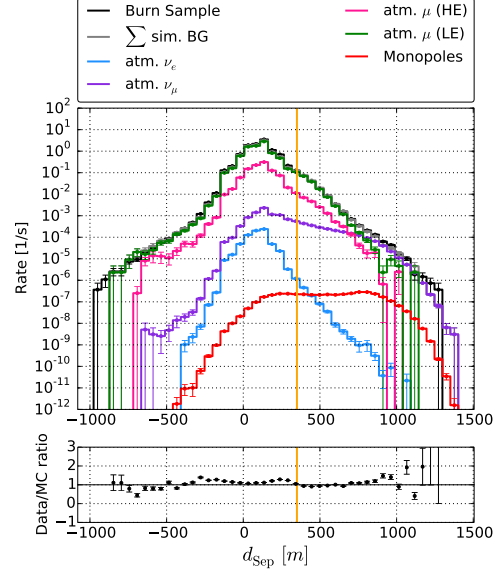
Figure E.2: Cut on the $d_{\mathrm{Separation}} \geq 350\,\mathrm{m}$. This is the most efficient pre-cut. Negative values of this variable refer to down-going events. Small values refer to cascades or short tracks.
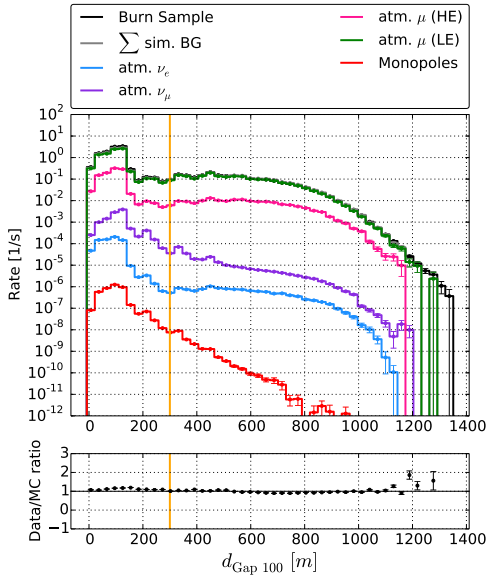
Figure E.3: Cut on $d_{\mathrm{Gap100}} \leq 300\,\mathrm{m}$ to enhance the quality of the events in all data and simulation sets.

E.4   Features for pull-validation
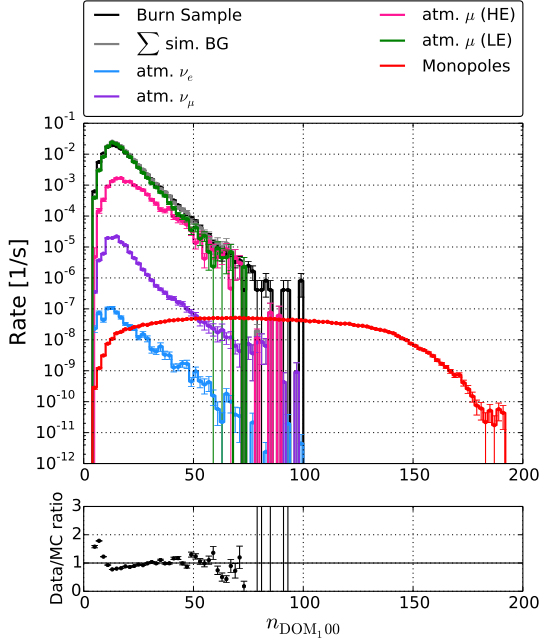
Figure E.4: BDT feature of mRMR order 1.
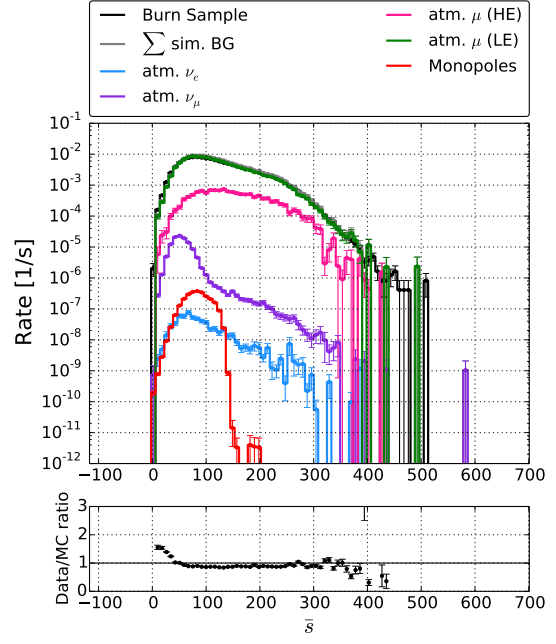
Figure E.5: BDT feature of mRMR order 2.
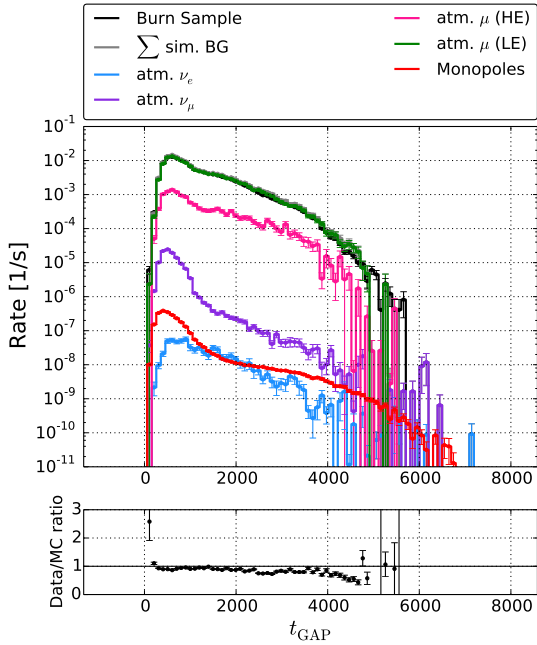
Figure E.6: BDT feature of mRMR order 3.
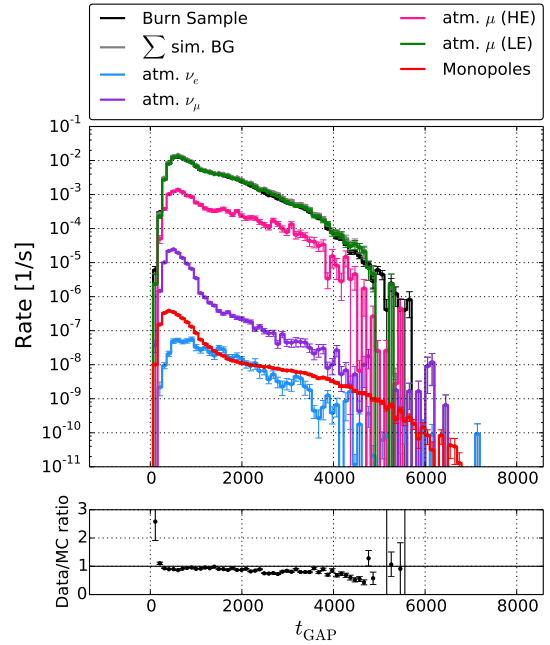
Figure E.7: BDT feature of mRMR order 4.
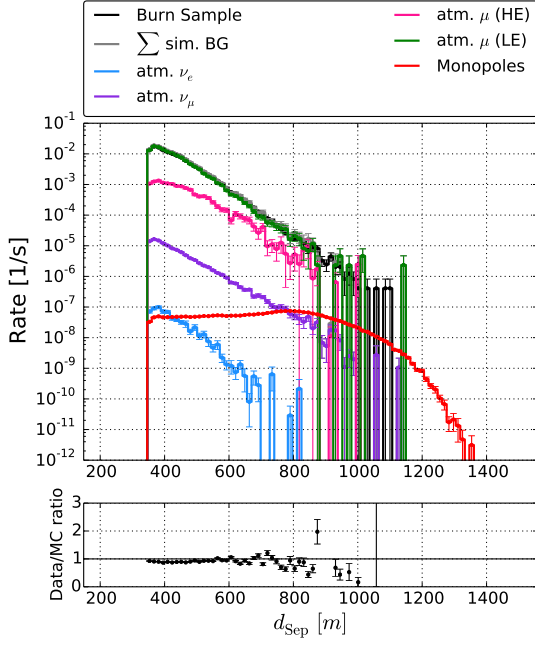
Figure E.8: BDT feature of mRMR order 5.
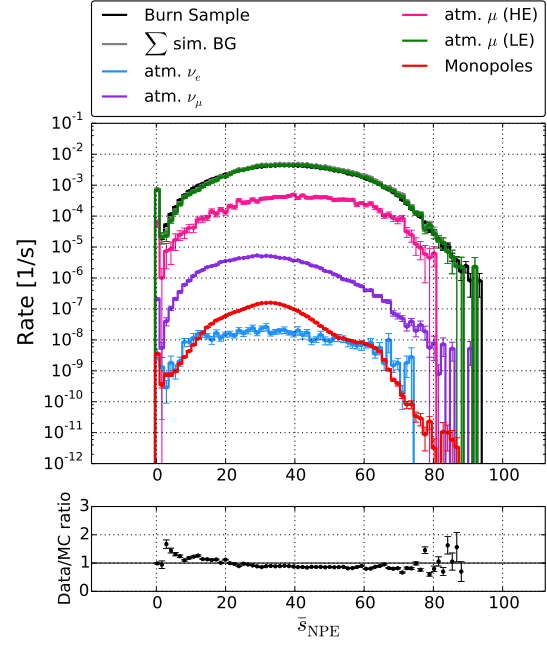
Figure E.9: BDT feature of mRMR order 6.
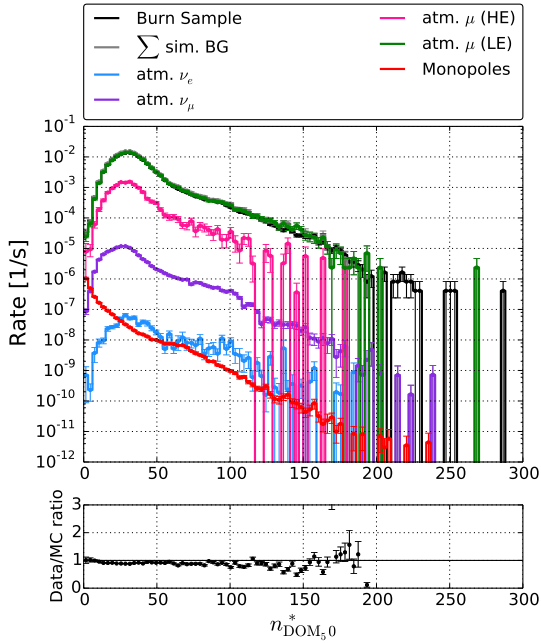
Figure E.10: BDT feature of mRMR order 7.
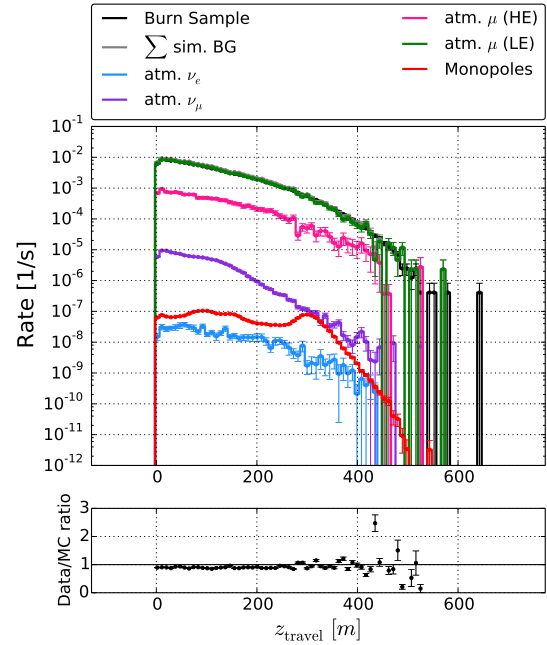
Figure E.11: BDT feature of mRMR order 8.
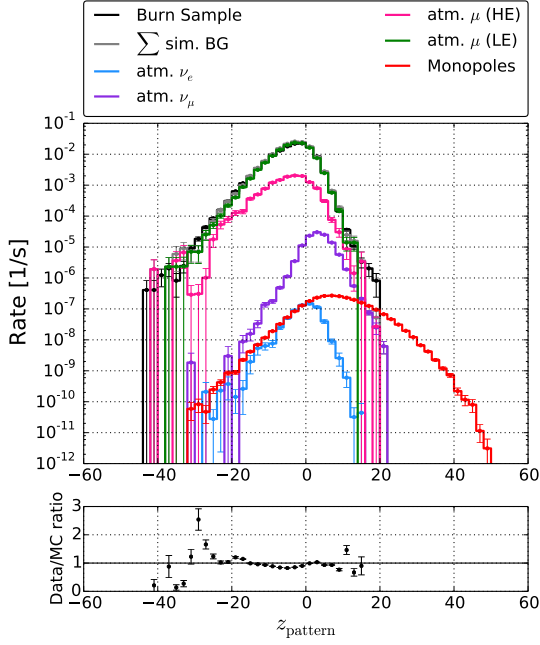
Figure E.12: BDT feature of mRMR order 9.
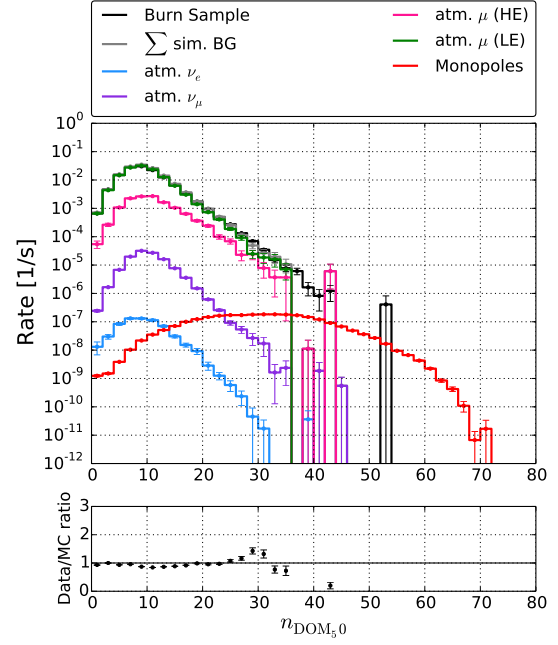
Figure E.13: BDT feature of mRMR order 10.
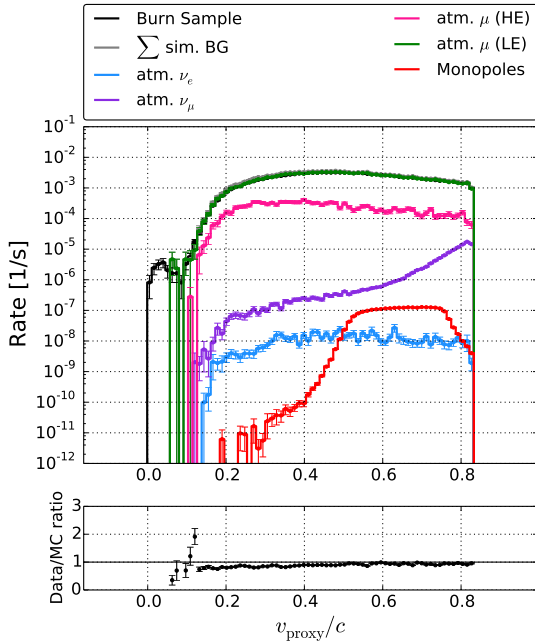
Figure E.14: BDT feature of mRMR order 11.
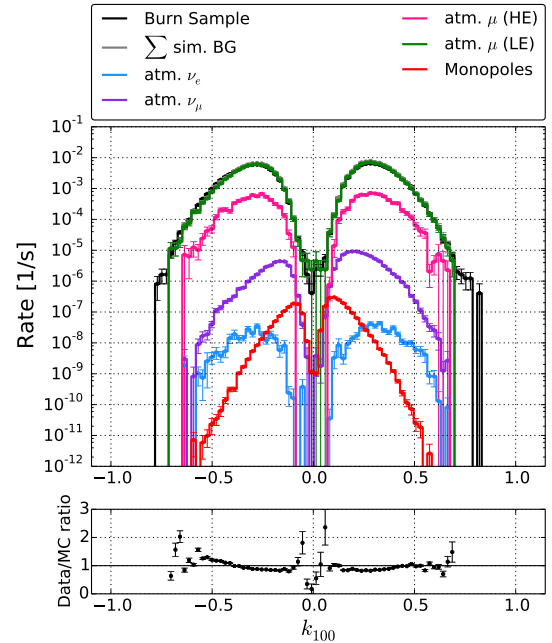
Figure E.15: BDT feature of mRMR order 12.
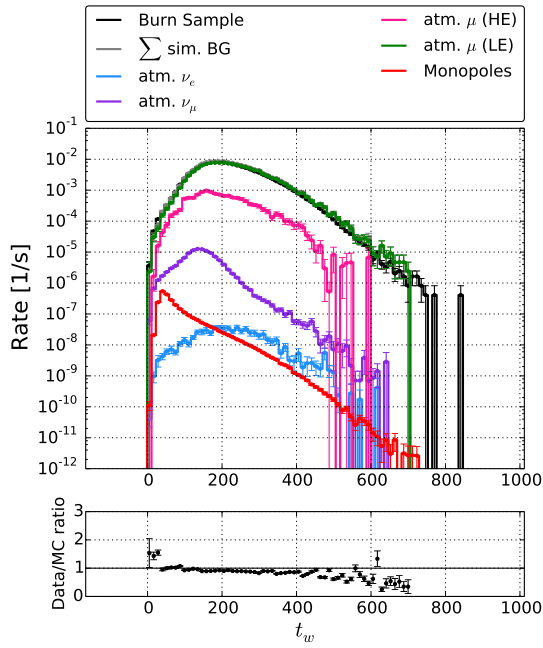
Figure E.16: BDT feature of mRMR order 13.
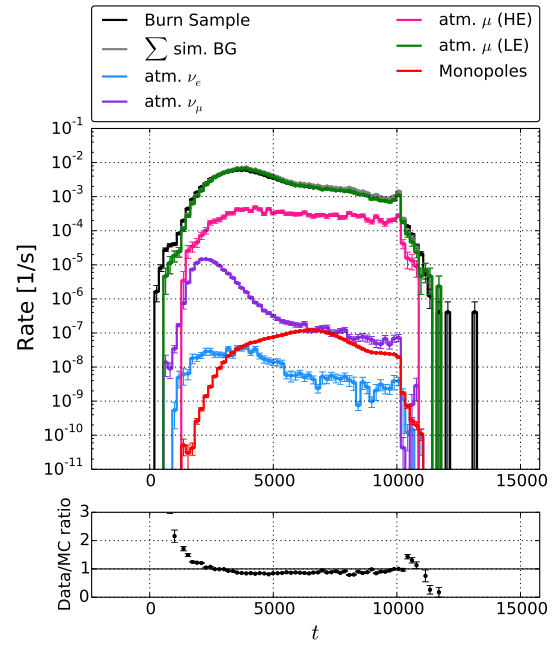
Figure E.17: BDT feature of mRMR order 14.
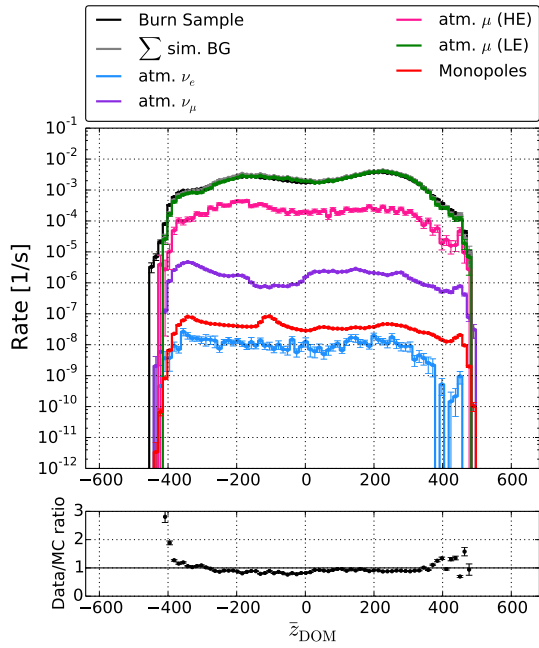
Figure E.18: BDT feature of mRMR order 15.

References

[Aad12] G. Aad et al. (ATLAS Collaboration), Observation of a new particle in the search for the Standard Model Higgs boson with the ATLAS detector at the LHC. *Phys. Lett. B*, 716(1):1–29 (2012), doi:10.1016/j.physletb.2012.08.020 (cit. on p. 13)

[Aar04] M. G. Aartsen et al. (IceCube Collaboration), IceCube-Gen2: A Vision for the Future of Neutrino Astronomy in Antarctica (2004), `http://arxiv.org/abs/1412.5106` (cit. on p. 85)

[Aar13a] M. G. Aartsen et al. (IceCube Collaboration), Evidence for High-Energy Extraterrestrial Neutrinos at the IceCube Detector. *Science*, 342(6161) (2013), doi:10.1126/science.1242856, `http://arxiv.org/abs/1311.5238` (cit. on pp. 5 and XI)

[Aar13b] M. G. Aartsen et al. (IceCube Collaboration), Measurement of South Pole ice transparency with the IceCube LED calibration system. *Nucl. Instrum. Meth. A*, 711:73–89 (2013), `http://arxiv.org/abs/1301.5361` (cit. on pp. 8, 46, 47, and 48)

[Aar14a] M. G. Aartsen et al. (IceCube Collaboration), Improvement in Fast Particle Track Reconstruction with Robust Statistics. *Nucl. Instrum. Meth. A*, 736:143–149 (2014), `http://arxiv.org/abs/1308.5501` (cit. on p. 60)

[Aar14b] M. G. Aartsen et al. (IceCube-PINGU Collaboration), Letter of Intent: The Precision IceCube Next Generation Upgrade (PINGU) (2014), `http://arxiv.org/abs/1401.2046` (cit. on p. 86)

[Aar14c] M. G. Aartsen et al. (IceCube Collaboration), Observation of High-Energy Astrophysical Neutrinos in Three Years of IceCube Data. *Phys. Rev. Lett.*, 113(10):101101 (2014) (cit. on p. 45)

[Aar14d] M. G. Aartsen et al. (IceCube Collaboration), Search for non-relativistic magnetic monopoles with IceCube. *Eur. Phys. J. C*, 74:2938 (2014) (cit. on pp. 10, 18, 78, XII, and XIII)

[Aar15] M. G. Aartsen et al. (IceCube Collaboration), Multipole analysis of IceCube data to search for dark matter accumulated in the Galactic halo. *Eur. Phys. J. C*, 75(1):20 (2015), `http://dx.doi.org/10.1140/epjc/s10052-014-3224-5` (cit. on p. 10)

[Abb09] R. Abbasi et al. (IceCube Collaboration), The IceCube data acquisition system: Signal capture, digitization and timestamping. *Nucl. Instrum. Meth. A*, 601(3):2994–316 (2009) (cit. on p. 9)

[Abb10a] R. Abbasi et al. (IceCube Collaboration), Calibration and characterization of the IceCube photomultiplier tube. *Nucl. Instrum. Meth. A*, 618(1-3):139–152 (2010) (cit. on pp. 8 and 9)

REFERENCES

[Abb10b] R. Abbasi et al. (IceCube Collaboration), Search for relativistic magnetic monopoles with the Amanda-II neutrino telescope. *Eur. Phys. J. C*, 69:361–378 (2010) (cit. on pp. 79 and 84)

[Abb13] R. Abbasi et al. (IceCube Collaboration), Search for relativistic magnetic monopoles with IceCube. *Phys. Rev. D*, 87:022001 1–11 (2013) (cit. on pp. 10, 18, 79, and 84)

[Ach06] A. Achterberg et al. (IceCube Collaboration), First year performance of the IceCube neutrino telescope. *Astropart. Phys.*, 26:155–173 (2006), doi:10.1016/j.astropartphys.2006.06.007, http://arxiv.org/abs/astro-ph/0604450 (cit. on pp. 3, 6, 7, and 9)

[Ack06] M. Ackermann et al. (IceCube Collaboration), Optical properties of deep glacial ice at the South Pole. *J. Geophys. Res.*, 111(D13) (2006) (cit. on pp. 7 and 34)

[Ahl75] S. P. Ahlen, Monopole-track characteristics in plastic detectors. *Phys. Rev. D*, 14:2935–2940 (1975) (cit. on pp. 24, 25, 28, 30, and 38)

[Ahl78] S. P. Ahlen, Stopping-power formula for magnetic monopoles. *Phys. Rev. D*, 17(1):229–233 (1978) (cit. on pp. 28, 30, 31, and 32)

[Ahl80] S. P. Ahlen, Theoretical and experimental aspects of the energy loss of relativistic heavily ionizing particles. *Rev. Mod. Phys.*, 52(1):121–173 (1980) (cit. on p. 24)

[All06] J. Allision et al., Geant4 developments and applications. *IEEE T. Nucl. Sci.*, 53(1):270–278 (2006) (cit. on p. 46)

[AM12] S. Adrián-Martínez et al. (ANTARES Collaboration), Search for relativistic magnetic monopoles with the ANTARES neutrino telescope. *Astropart. Phys.*, 35:634–640 (2012), doi:10.1016/j.astropartphys.2012.02.007, http://arxiv.org/abs/1110.2656 (cit. on pp. 18, 25, 28, 49, 79, and 84)

[Amb02] M. Ambrosio et al. (MACRO Collaboration), Final results of magnetic monopole searches with the MACRO experiment. *Eur. Phys. J. C*, 25:511–522 (2002) (cit. on pp. 17, 79, and 84)

[And33] C. D. Anderson, The Positive Electron. *Phys. Rev.*, 43(6):491–494 (1933), doi:10.1103/PhysRev.43.491 (cit. on p. 11)

[Arn83] G. Arnison et al. (UA 1 Collaboration), Experimental observation of isolated large transverse energy electrons with associeated missing energy at s=540GeV. *Phys. Lett. B*, 122(1):103–116 (1983), doi:10.1016/0370-2693(83)91177-2 (cit. on p. 13)

[Ayn08] V. Aynutdinov et al. (BAIKAL Collaboration), Search for relativistic magnetic monopoles with the Baikal neutrino telescope. *Astrophys. J.*, 29:366–372 (2008) (cit. on pp. 18, 28, 79, 84, X, and XI)

[Ban83]   M. Banner et al. (UA2 Collaboration), Observation of single isolated electrons of high transverse momentum in events with missing transverse energ at the CERN pp collider. *Phys. Lett. B*, 122(5-6):476–485 (1983), doi:10.1016/0370-2693(83) 91605-2 (cit. on p. 13)

[Bar04]   G. D. Barr, T. K. Gaisser, P. Lipari, S. Robbins, and T. Stanev, A three-dimensional calculation of atmospheric neutrinos. *Phys. Rev. D*, 70:023006 (2004), `http://arxiv.org/abs/astro-ph/0403630` (cit. on p. 45)

[Bau51]   E. Bauer, The energy loss of free magnetic poles in passing through matter. *Mathematical Proceedings of the Cambridge Philosophical Society*, 47(04):777–789 (1951), doi:10.1017/S0305004100027225 (cit. on pp. 23, 24, 28, and 30)

[Bel53]   E. H. Belcher, The Luminescence of Irradiated Transparent Media and the Cerenkov Effekt. I. The Luminescence of Aqueous Solutions of Radioactive Isotopes. *Proc. R. Soc. Lond. A*, 216:90–102 (1953) (cit. on pp. 36, 37, and VIII)

[Bel98]   I. A. Belolaptikov et al., The Experimental limits on Q ball flux with the Baikal deep underwater array 'Gyrlyanda' (1998), `astro-ph/9802223` (cit. on p. 10)

[Ber12]   J. Beringer et al. (Particle Data Group), The Review of Particle Physics. *Phys. Rev. D*, 86:323 (2012), chapter 30: Passage of particles through matter, `http://pdg.lbl.gov` (cit. on p. 26)

[Bet30]   H. Bethe, Zur Theorie des Durchgangs schneller Korpuskularstrahlen durch Materie. *Ann. Phys.*, 397(3):325–400 (1930), doi:10.1002/andp.19303970303 (cit. on p. 29)

[Boe04]   G. Boerner, The early universe. Springer (2004) (cit. on pp. 13 and 14)

[Boh13]   N. Bohr, On the Theory of the Decrease of Velocity of Moving Electrified Particles on passing through Matter. *Phil. Mag*, 6(25):10–31 (1913) (cit. on p. 25)

[Boj15]   I. E. Bojaddaini and G. E. Pavalas (ANTARES Collaboration), Search for magnetic monopoles with the ANTARES neutrino telescope. In International Cosmic Ray Conference, POS1097 (2015) (cit. on p. 86)

[Bor26]   M. Born, Quantenmechanik der Stoßvorgänge. *Z. Physik*, 38(11-12):803–827 (1926) (cit. on p. 29)

[Bri11]   R. J. Britto et al., Data analysis method for the search of point sources of gamma rays with the HAGAR telescope array. In 32nd international Cosmic Ray Conference (2011), doi:10.7529/ICRC2011/V09/0943 (cit. on p. 61)

[Cab82]   B. Cabrera, First results from a superconductive detector for moving magnetic monopoles. *Phys. Rev. Lett.*, 48:1378–1381 (1982) (cit. on p. 17)

[Cal83]   C. G. Callan, Monopole catalysis of baryon decay. *Nucl. Phys. B*, 212:391–400 (1983) (cit. on p. XII)

[Cha12]   S. Chatrchyan et al. (CMS Collaboration), Observation of a new boson at a mass of 125 GeV with the CMS experiment at the LHC. *Phys. Lett. B*, 716(1):30–61 (2012), doi:10.1016/j.physletb.2012.08.021 (cit. on p. 13)

[Che34]   P. A. Cherenkov, Vidimoe svechenie chistykh zhidkostei pod deistviem γ-radiatsii (Visible glow from clear liquids under the action of gamma radiation). *Acad. Sci URSS (Akad. of Science of the USSR)*, 2(8):451–454 (1934) (cit. on p. 34)

[Che37]   P. Cherenkov, Visible radiation produced by electrons moving in a medium with velocities exceeding that of light. *Phys. Rev. Lett.*, 52 (1937) (cit. on p. 34)

[Che60]   P. A. Cherenkov, Radiation from high-speed particles. *Science*, 131:136–142 (1960) (cit. on pp. 34 and VIII)

[Chi04]   D. Chirkin and W. Rhode, Propagating leptons through matter with Muon Monte Carlo (MMC) (2004), `http://arxiv.org/abs/hep-ph/0407075` (cit. on p. 45)

[Chi13]   D. Chirkin (IceCube collaboration), Evidence of optical anisotropy of the South Pole ice. In proceedings of the International Cosmic Ray Conference, 580 (2013) (cit. on pp. 7 and 8)

[Chr11]   B. J. Christy, A Search for Relativistic Magnetic Monopoles with the IceCube 22-String Detector. Ph.D. thesis, University of Maryland (2011) (cit. on pp. 49 and 50)

[Col51]   H. J. D. Cole, The theoretical behaviour of a magnetic monopole in a wilson cloud chamber. *Mathematical Proceedings of the Cambridge Philosophical Society*, 47(01):196–206 (1951) (cit. on pp. 23, 25, 28, 30, and 32)

[Dan80]   M. Daniel, G. Lazarides, and Q. Shafi, SU(5) monopoles, magnetic symmetry and confinement. *Nucl. Phys. B*, 170(1):156–164 (1980), doi:10.1016/0550-3213(80)90483-6 (cit. on p. 14)

[Det11]   M. Detrixhe et al. (ANITA Collaboration), Ultrarelativistic magnetic monopole search with the ANITA-II balloon-borne radio interferometer. *Phys. Rev. D*, 83:023513 (2011) (cit. on p. 18)

[DeY04]   T. DeYoung, Icetray: A software framework for icecube. In In- ternational Conference on Computing in High-Energy Physics and Nuclear Physics (2004), available from `http://www.chep2004.org/` (cit. on p. 42)

[Dir28]   P. A. M. Dirac, The Quantum Theory of the Electron. *Proc. Roy. Soc.*, 117(778):610–624 (1928) (cit. on p. 11)

[Dir31]   P. Dirac, Quantized Singularities in the Electromagnetic Field. *Proc. Roy. Soc.*, A 133:60–73 (1931) (cit. on pp. 11 and 15)

[Dir58]   P. A. M. Dirac, Principles of Quantum Mechanics. International Series of Monographs on Physics, Oxford University Press, fourth ed. (1958) (cit. on p. 26)

[Dom70a]   G. V. Domogatski and I. M. Zheleznykh, The hot-universe model and the problem of the dirac monopole. *Soviet Journal of Nuclear Physics (english translation)*, 10(6):702–704 (1970) (cit. on p. 25)

[Dom70b]   G. V. Domogatski and I. M. Zheleznykh, The hot-universe model and the problem of the dirac monopole. *Soviet Journal of Nuclear Physics (english translation)*, 10(6):702–704 (1970) (cit. on p. 28)

[Dpm00]   The Monte Carlo event generator DPMJET-III, Springer Berlin (2000), `http://xxx.lanl.gov/abs/hep-ph/0012252` (cit. on p. 44)

[dS15]   R. P. dos Santos, Magnetic monopoles and dyons revisited: A useful contribution to the study of classical mechanics. *Eur. Phys. J. C*, 36(3):035022 (2015), doi:10.1088/0143-0807/36/3/035022, `http://arxiv.org/pdf/1503.00499v1.pdf` (cit. on p. 26)

[Dut01]   S. I. Dutta, M. H. Reno, I. Sarcevic, and D. Seckel, Propagation of Muons and Taus at High Energies. *Phys. Rev. D*, 63:094020 (2001), `http://arxiv.org/abs/hep-ph/0012350` (cit. on p. 33)

[Efr79]   B. Efron, Bootstrap Methods: Another look at the Jackknife. *Ann. Stat.*, 7(1):1–26 (1979) (cit. on pp. 61 and XVIII)

[Enb08]   R. Enberg, M. H. Reno, and I. Sarcevic, Prompt neutrino fluxes from atmospheric charm. *Phys. Rev. D*, 78(4):043005 (2008), `http://arxiv.org/abs/0806.0418` (cit. on p. 45)

[Eng64]   F. Englert and R. Brout, Broken Symmetry and the Mass of Gauge Vector Mesons. *Phys. Rev. Lett.*, 13:321 (1964), doi:10.1103/PhysRevLett.13.321 (cit. on p. 13)

[Esp04]   G. Esposito, G. Marmo, and E. C. G. Sudarshan, From Classical to Quantum Mechanics. Cambridge University Press (2004) (cit. on p. 28)

[Faw06]   T. Fawcett, An introduction to ROC analysis. *Pattern Recognition Letters*, 27:861–874 (2006) (cit. on p. 66)

[Fel98]   G. J. Feldman and R. D. Cousins, Unified approach to the classical statistical analysis of small signals. *Phys. Rev. D*, 57(7):3873–3889 (1998) (cit. on p. 75)

[Fer50]   E. Fermi, Nuclear Physics. University of Chicago Press (1950), ISBN 9780226243658 (cit. on p. 22)

[Fio01]   G. Fiorentini, V. A. Naumov, and F. L. Villante, Atmospheric neutrino flux supported by recent muon experiments. *Phys. Lett. B*, 510(1-4):173–188 (2001), `http://arxiv.org/abs/hep-ph/0103322` (cit. on p. 45)

[Fle94]   R. S. Fletcher, T. K. Gaisser, P. Lipari, and T. Stanev, Sibyll: An event generator for simulation of high energy cosmic ray cascades. *Phys. Rev. D*, 50:5710–5731 (1994) (cit. on p. 43)

[Fre95]   Y. Freund, Boosting a weak lerning algorithm by majority. *Inform. Comput.*, 121(2):256–285 (1995), doi:10.1006/inco.1995.1136, `http://www.curtismeyer.com/articles/bkgrnd/phystat05-proc.pdf` (cit. on p. 62)

[Fri01]   J. H. Friedman, Greedy Function Approximation: A Gradient Boosting Machine. *Ann. Stat.*, 29(5):1189–1232 (2001) (cit. on p. 66)

[Fuj15]   T. Fujii (Pierre Auger Collaboration), Search for Ultra-relativistic Magnetic Monopoles with the Pierre Auger Observatory. In proceedings of the International Cosmic Ray Conference, PoS(ICRC2015)319 (2015) (cit. on p. 18)

[Gai92]   T. K. Gaisser, Particle astrophysics with high energy neturinos. Cambridge University Press (1992) (cit. on p. 3)

[Gai12]   T. K. Gaisser, Spectrum of cosmic-ray nucleons, kaon production, and the atmospheric muon charge ratio. *Astropart. Phys.*, 35(12):801–806 (2012), `http://arxiv.org/abs/1111.6675` (cit. on pp. 43 and 44)

[Gan98]   R. Gandhi, C. Quigg, M. H. Reno, and I. Sarcevic, Neutrino interactions at ultrahigh energies. *Phys. Rev. D*, 58(093009) (1998) (cit. on p. 4)

[Geo74]   H. Georgi, H. R. Quinn, and S. Weinberg, Hierarchy of Interactions in Unified Gauge Theories. *Phys. Rev. Lett.*, 33(7):451–454 (1974), doi:10.1103/PhysRevLett.33.451 (cit. on p. 14)

[Glu10]   T. Gluesenkamp, On the Detection of Subrelativistic Magnetic Monopoles with the IceCube Neutrino Observatory. Master's thesis, RWTH Aachen University (2010) (cit. on pp. 15 and 49)

[Gro52]   L. I. Grossweiner and M. S. Matheson, Luminescence of Ice and Tritiated Ice. *J. Chem. Phys.*, 20(10):1654 (1952), doi:10.1063/1.1700246 (cit. on p. VIII)

[Gro54]   L. I. Grossweiner and M. S. Matheson, Fluorescence and Thermoluminescence of Ice. *J. Chem. Phys.*, 22(9):1514–1526 (1954), doi:10.1063/1.1740451 (cit. on p. VIII)

[Gur64]   G. S. Guralnik, C. R. Hagen, and T. W. B. Kibble, Global Conservation Laws and Massless Particles. *Phys. Rev. Lett.*, 13:585 (1964), doi:10.1103/PhysRevLett.13.585 (cit. on p. 13)

[Hae07]   W. Haerdle and Z. Hlavka, Multivariate Statistics. Springer New York (2007), ISBN 978-0-387-73508-5, doi:10.1007/978-0-387-73508-5 (cit. on p. 79)

[Hag75]   R. Hagstrom, Practicable Discrimination of Rapidly Moving Electric and Magnetic Charges. *Phys. Rev. Lett.*, 35(25):1677–1678 (1975) (cit. on p. 37)

[Hec98]   D. Heck, J. Knapp, J. N. Capdevielle, G. Schatz, and T. Thouw, CORSIKA: A Monte Carlo Code to Simulate Extensive Air Showers. Forschungszentrum Karlsruhe GmbH, Karlsruhe (1998) (cit. on p. 43)

[Hes12]   V. F. Hess, Über Beobachtungen der durchdringenden Strahlung bei sieben Freiballonfahrten. *Physikalische Zeitschrift*, 13:1084–1091 (1912) (cit. on p. 3)

[Hig64a]   P. W. Higgs, Broken symmetries and the masses of gauge bosons. *Phys. Rev. Lett.*, 13:508 (1964), doi:10.1103/PhysRevLett.13.508 (cit. on p. 13)

[Hig64b]   P. W. Higgs, Broken symmetries, massless particles and gauge fields. *Phys. Lett.*, 12(2):132–133 (1964), doi:10.1016/0031-9163(64)91136-9 (cit. on p. 13)

[Hil03]   G. C. Hill and K. Rawlins, Unbiased cut selection for optimal upper limits in neutrino detectors: the model rejection potential technique. *Astropart. Phys.*, 19:393–402 (2003) (cit. on p. 75)

[Hil05a]   G. C. Hill, J. Hodges, B. Hughey, A. Karle, and M. Stamatikos, Examining the balance between optimising an analysis for best limit setting and best discovery potential. *Proceedings of PHYSTAT05* (2005), `http://www.physics.ox. ac.uk/phystat05/proceedings/files/mdp.ps` (cit. on p. 76)

[Hil05b]   A. M. Hillas, Can diffusive shock acceleration in supernova remnants account for high-energy galactic cosmic rays? *J. Phys. G*, 31(5):R95 (2005) (cit. on p. 43)

[Hoe13]   A. Hoecker et al., TMVA - Toolkit for Multivariate Data Analysis (2013), `physics/0703039` (cit. on p. XVI)

[Hog08]   D. P. Hogan, D. Z. Besson, J. P. Ralston, I. Kravchenko, and D. Seckel, Relativistic magnetic monopole flux constraints from Rice. *Phys. Rev. D*, 78:075031 (2008), doi:10.1103/PhysRevD.78.075031 (cit. on p. 18)

[Hon07]   M. Honda, T. Kajita, K. Kasahara, S. Midorikawa, and T. Sanuki, Calculation of atmospheric neutrino flux using the interaction model calibrated with atmospheric muon data. *Phys. Rev. D*, 75(4):043006 (2007) (cit. on p. 44)

[Hug00]   E. Huguet and P. Peter, Bound states in monopoles: sources for UHECR? *Astropart. Phys.*, 12(4):277–289 (2000), doi:10.1016/S0927-6505(99)00105-X (cit. on p. 16)

[Ice15]   IceCube collaboration (2015), `http://internal.icecube.wisc.edu`. Accessed 31.8.2015 (cit. on p. 6)

[Jac99]   J. D. Jackson, Classical Electrodynamics. John Wiley and Sons, third ed. (1999) (cit. on pp. 25 and 33)

[Kal07]   A. Kalousis, J. Prados, and M. Hilario, Stability of feature selection algorithms: a study on high-dimensional spaces. *Knowledge and Information Systems*, 12(1):95–116 (2007), doi:10.1007/s10115-006-0040-8 (cit. on p. 66)

[Kaz77]   Y. Kazama, C. N. Yang, and A. S. Goldhaber, Scattering of a Dirac particle with charge Ze by a fixed Magnetic Monopole. *Phys. Rev. D*, 15:2287–2299 (1977) (cit. on pp. 26, 27, and 28)

[Kel67]   S. R. Kel'ner, Pair production in collisions between a fast particle and a nucleus. *Sov. Jour. Nucl. Phys.*, 5:778 (1967) (cit. on p. 32)

[Kel68]   S. R. Kel'ner and Y. D. Kotov, Muon energy loss to pair production. *Sov. Jour. Nucl. Phys.*, 7(2):237 (1968) (cit. on p. 32)

REFERENCES

[Kep96]   T. W. Kephart and T. J. Weiler, Magnetic monopoles as the highest energy cosmic ray. *Astropart. Phys.*, 4(3):271–279 (1996), doi:10.1016/0927-6505(95)00043-7 (cit. on pp. 13 and 17)

[Kep07]   T. W. Kephart, C.-A. Lee, and Q. Shafi, Family unification, exotic states and light magnetic monopoles. *J. High Energy Phys.*, 2007(01):088 (2007), doi:10.1088/1126-6708/2007/01/088 (cit. on p. 14)

[Kib76]   T. W. B. Kibble, Topology of cosmic domains and strings. *J. Phys. A: Math. Gen.*, 9:1387 (1976), doi:10.1088/0305-4470/9/8/029 (cit. on p. 15)

[Kin98]   S. King and Q. Shafi, Minimal supersymmetric SU(4)×SU(2)L×SU(2)R. *Phys. Lett. B*, 422(1-4):135–140 (1998), doi:10.1016/S0370-2693(98)00058-6 (cit. on p. 14)

[Koe13]   J.-H. Koehne, K. Frantzen, M. Schmitz, T. Fuchs, W. Rhode, D. Chirkin, and J. Becker Tjus, PROPOSAL: A tool for propagation of charged leptons. *Comput. Phys. Commun.*, 184:2070–2090 (2013), doi:10.1016/j.cpc.2013.04.001 (cit. on p. 45)

[Kop15]   S. Kopper (IceCube collaboration), Search for Neutrino Induced Double Tracks as an Exotic Physics Signature in IceCube. In proceedings of the International Cosmic Ray Conference, 1104 (2015), `http://pos.sissa.it/archive/conferences/236/1061/ICRC2015_1061.pdf` (cit. on p. 10)

[Kun15a]   J. Kunnen, J. Luenemann, A. Obertacke Pollmann, and F. Scheriau for the IceCube Collaboration, Pull-Validation: A resampling method to improve the usage of low-statistics datasets. In proceedings of the International Cosmic Ray Conference, 361 (2015), arXiv:1510.05226 (cit. on pp. 62 and 69)

[Kun15b]   J. Kunnen and J. Luenemann for the IceCube Collaboration, A search for Dark Matter in the centre of the Earth with the IceCube neutrino detector. In proceedings of the International Cosmic Ray Conference, 125 (2015) (cit. on p. 64)

[Lac68]   P. A. Lachenbruch and M. R. Mickey, Estimation of Error Rates in Discriminant Analysis. *Technometrics*, 10(1):1–11 (1968), doi:10.1080/00401706.1968.10490530 (cit. on pp. 61 and XVIII)

[Lan60]   L. D. Landau and E. M. Lifshitz, Electrodynamics of Continuous Media. Addison-Wesley (1960), chap. 12 (cit. on p. 31)

[Lun07]   J. Lundberg et al., Light tracking for glaciers and oceans: Scattering and absorption in heterogeneous media with photonics. *Nucl. Instrum. Meth. A*, 581:619–631 (2007) (cit. on p. 46)

[Ma11]   K. Ma, W. Kang, J. Ahn, S. Choi, Y. Choi, M. Hwang, J. Jang, E. Jeon, K. Joo, H. Kim, J. Kim, S. Kim, S. Kim, W. Kim, Y. Kim, J. Lee, I. Lim, Y. Oh, M. Pac, C. Park, I. Park, K. Park, S. Stepanyan, and I. Yu, Time and amplitude of afterpulse measured with a large size photomultiplier tube. *Nucl. Instrum. Meth. A*, 629(1):93–100 (2011), doi:http://dx.doi.org/10.1016/j.nima.2010.11.095 (cit. on p. 9)

XXXVII

[Max65]   J. C. Maxwell, A Dynamical Theory of the Electromagnetic Field. *Phil. Trans. R. Soc. Lond.*, 155:459–512 (1865) (cit. on pp. 11, 12, and 16)

[Mil06]   K. A. Milton, Theoretical and experimental status of magnetic monopoles. *Proc. Prog. Phys.*, 69(6):1637 (2006) (cit. on p. 28)

[Mou01]   F. Moulin, Magnetic monopoles and lorentz force. *Il Nuovo Cimento B*, 116:869–877 (2001) (cit. on p. 16)

[Nie01]   P. Nießen, Search for relativistic magnetic monopoles with the AMANDA detector. Ph.D. thesis, Humboldt-Universität zu Berlin (2001) (cit. on pp. 20, 28, and 65)

[Obe12]   A. Obertacke, Search for Relativistic Magnetic Monopoles below the Cherenkov Threshold with IceCube-86. Diploma thesis, University of Wuppertal (2012) (cit. on pp. 1, 5, 21, 28, and 84)

[Oli14]   K. A. Olive et al. (Particle Data Group). *Chinese Physics C*, 38(9):090001 (2014), doi:10.1088/1674-1137/38/9/090001 (cit. on pp. 3, 17, 25, 29, 30, 38, and 40)

[Par70]   E. N. Parker, The Origin of Magnetic Fields. *Astrophys. J.*, 160:383 (1970) (cit. on p. 17)

[Par71]   E. Parker, The generation of magnetic fields in astrophysical bodies. II. The galactic field. *Astrophys. J.*, 163:255–278 (1971) (cit. on p. 17)

[PC10]   N. Picot-Clémente, Recherche de monopôles magnétiques avec le télescope à neutrinos ANTARES. Ph.D. thesis, Université de la Méditerranée (2010) (cit. on p. 25)

[Pen05]   H. Peng, Feature Selection Based on Mutual Information: Criteria of Max-Dependency, Max-Relevance, and Min-Redundancy. *IEEE Trans. Pattern Anal. Mach. Intell.*, 27(8):1226–1238 (2005), doi:10.1109/TPAMI.2005.159 (cit. on p. 67)

[Pes94]   M. E. Peskin, Spin, Mass, and Symmetry. In Spin structure in high-energy processes: Proceedings, 21st SLAC Summer Institute on Particle Physics, 26 Jul - 6 Aug 1993, Stanford, CA (1994), `hep-ph/9405255` (cit. on p. 24)

[Pol04]   J. Polchinski, Monopoles, Duality, and String Theory. *Int. J. Mod. Phys. A*, 19:145 (2004), doi:10.1142/S0217751X0401866X, `http://arxiv.org/abs/hep-th/0304042` (cit. on pp. 11 and 85)

[Pol15]   A. Pollmann (2015), `https://wiki.icecube.wisc.edu/index.php/IC86-1_Mildly_Relativistic_Monopoles`; Last accessed 28.9.15 (cit. on p. 81)

[Pol16]   A. Pollmann and J. Posselt, Search for relativistic magnetic monopoles with v > 0.5c in IceCube. *EPJ-C*, 76(133):1 – 16 (2016), doi:10.1140/epjc/s10052-016-3953-8, `http://arxiv.org/abs/1511.01350` (cit. on pp. 36, 45, 68, 69, 79, 82, 83, and 84)

[Pos13a]   J. Posselt, Search for Relativistic Magnetic Monopoles with the IceCube 40-String Detector. Ph.D. thesis, University of Wuppertal (2013) (cit. on pp. 18, 31, 45, 49, 78, 79, and 84)

[Pos13b]   J. Posselt and A. Obertacke, Search for Relativistic Magnetic Monopoles with the IceCube Neutrino Telescope. In Exotic Physics with Neutrino Telescopes (2013), `https://indico.in2p3.fr/event/7381/material/slides/0?contribId=22` (cit. on p. 28)

[Pov09]   B. Povh, K. Rith, C. Scholz, and F. Zetsche, Teilchen und Kerne. Springer Berlin Heidelberg, 8th ed. (2009) (cit. on p. 22)

[Pre84]   J. P. Preskill, Magnetic Monopoles. *Ann. Rev. Nucl. Part. Sci.*, 34:461–530 (1984) (cit. on pp. 13 and 14)

[Qui82]   T. I. Quickenden, S. M. Trotman, and D. F. Sangster, Pulse radiolytic studies of the ultraviolet and visible emission from purified H2O ice. *J. Chem. Phys.*, 77:3790 (1982), doi:10.1063/1.444352 (cit. on pp. VIII, IX, and X)

[Qui86]   J. R. Quinlan, Induction of Decision Trees. *Mach. Learn.*, 1:81–106 (1986) (cit. on p. 62)

[Rae12a]   L. Raedel, Simulation Studies of the Cherenkov Light Yield from Relativistic Particles in High-Energy Neutrino Telescopes with Geant4. Master's thesis, Rheinisch-Westfälische Technische Hochschule Aachen (2012) (cit. on pp. 46 and XXXIX)

[Rae12b]   L. Raedel and C. Wiebusch, Calculation of the Cherenkov light yield from low energetic secondary particles accompanying high-energy muons in ice and water with Geant4 simulations. *Astropart. Phys.*, 38:53–67 (2012), see also thesis: [Rae12a] (cit. on pp. 47 and 48)

[Rae15]   L. Raedel and S. Schoenen, A measurement of the diffuse astrophysical muon neutrino flux using multiple years of IceCube data. In International Cosmic Ray Conference, PoS(ICRC2015)1079 (2015) (cit. on pp. 57, XI, and XIV)

[Raj12]   A. Rajantie, Introduction to magnetic monopoles. *Contemp. Phys.*, 53(3):195–211 (2012) (cit. on pp. 11, 13, 14, 15, and 37)

[Rat09]   C. Ratti and E. Shuryak, The role of monopoles in a Gluon Plasma. *Phys. Rev. D*, 80:034004 (2009) (cit. on p. 28)

[Ric02]   J. Ricol, Etude de la détection de monopôles magnétiques au sein du futur télescope à neutrinos Antares et caractérisation des performances du traitement des impulsions des photomultiplicateurs. Ph.D. thesis, Université de la Méditerranée (2002) (cit. on p. 25)

[Rom03]   A. Romeyer, Etude de la sensibilité du détecteur ANTARES à un flux diffus de neutrinos cosmiques de haute énergie. Ph.D. thesis, Université Paris (2003) (cit. on p. 45)

[Roo03] A. Roodman, Blind analysis in particle physics. In Proceedings of the conference on Statistical Problems in Particle Physics, Astrophysics, and Cosmology, 166 (2003), doi:10.1.1.298.6629 (cit. on p. 10)

[Rub82] V. A. Rubakov, Adler-Bell-Jackiw anomaly and fermion-number reaking in the presence of a magnetic monopole. *Nucl. Phys. B*, 203:311–348 (1982) (cit. on p. XII)

[Rub88] V. A. Rubakov, Monopole catalysis of proton decay. *Rep. Prog. Phys.*, 51(2):189 (1988) (cit. on p. XII)

[Rut11] E. Rutherford, The scattering of alpha and beta particles by matter and the structure of the atom. *Phil. Mag.*, 21:669–688 (1911), doi:10.1080/14786440508637080 (cit. on p. 23)

[Sch14] F. Scheriau, Data-Mining in der Astroteilchenphysik. Ph.D. thesis, University of Dortmund (2014) (cit. on pp. 62 and 64)

[Sel06] B. J. Selby, T. I. Quickenden, and C. G. Freeman, Isotopic Effects on the Time-Dependence of 420 nm Ice Luminescence Excited by UV light. *Kinet. Catal.*, 47(5):686–698 (2006) (cit. on pp. IX and XII)

[Ste56] R. M. Sternheimer, Density Effect for the Ionization Loss in Various Materials. *Phys. Rev.*, 103(3):511–515 (1956) (cit. on p. 31)

[Ste72] H. B. Steen, O. I. Sorensen, and J. A. Holteng, Observation of X-Ray and U.V.-induced luminescence and absorption during and after the radiation. *Int. J. Radiat. Phys. Chem.*, 4:75–86 (1972) (cit. on pp. IX and X)

[Ste75] H. B. Steen and J. A. Holteng, Radioluminescence of H2O and D2O ice. *J. Chem. Phys.*, 63(6):2690–2697 (1975) (cit. on p. IX)

[Ste84] R. M. Sternheimer. *At. Data Nucl. Data Tables*, 30(2):261 (1984) (cit. on pp. 29 and 32)

[Sul13] G. W. Sullivan, Results from the IceCube Experiment. In Neutrino 2012, 346–351 (2013), updated figures taken from `https://wiki.icecube.wisc.edu/index.php/Atmospheric_neutrino_fluxes` at 27/3/15, `http://arxiv.org/abs/1210.4195` (cit. on p. 44)

[Tam37] E. Tamm and M. Frank, Kogerentnoe izluchenie bystrogo elektrona v srede (The coherent radiation of a fast electron in a medium). *Dokl. Akad. Nauk SSSR (Akad. of Science of the USSR)*, 14:107 (1937) (cit. on pp. 34 and 35)

[Tho15] M. Thomson, Modern particle physics. Cambridge University Press, third ed. (2015) (cit. on p. 3)

[Tom64] D. R. Tompkins, Total Energy Loss and Čerenkov Emission from Monopoles. *Phys. Rev.*, 138(1B) (1964) (cit. on p. 37)

[Tro86] S. M. Trotman, T. I. Quickenden, and D. F. Sangster, Decay kinetics of the ultraviolet and visible luminescence emitted by electronirradiated H2O ice. *J. Chem. Phys.*, 85:2555–2568 (1986) (cit. on p. IX)

[Tro92]   I. I. Trofimenko (1992), preprint INR Russ. Ac. Sci. 765/92 (cit. on pp. 19 and XI)

[Vav34]   S. I. Vavilov, O vozmozhnykh prichinakh sinego γ-svecheniya zhidkostei (On the possible causes of the lue γ-glow of liquids). *Dokl. Akad. Nauk SSSR (Akad. of Science of the USSR)*, 2(8):457 (1934) (cit. on p. 34)

[vR06a]   B. A. P. van Rens, Detection of Magnetic Monopoles below the Cherenkov Limit. Ph.D. thesis, Universiteit van Amsterdam (2006) (cit. on pp. 25 and 40)

[vR06b]   B. A. P. van Rens, Detection of magnetic monopoles with the ANTARES detector. *Phys. Atom. Nucl.*, 69(11):1908–1913 (2006), doi: 10.1134/S1063778806110159 (cit. on p. 25)

[Wal10]   M. Wallraff, Design, Implementation and Test of a New Feature Extractor for the IceCube Neutrino Observatory. Master's thesis, RWTH Aachen University (2010) (cit. on p. 5)

[War84]   S. G. Warren, Optical constants of ice from the ultraviolet to the microwave. *Applied Optics*, 23(8):1206–1225 (1984) (cit. on p. 34)

[Wax00]   E. Waxman and J. N. Bahcall, Neutrino Afterglow from Gamma-Ray Bursts: 10^{18} eV. *Astrophys. J.*, 541:707–711 (2000) (cit. on p. 45)

[Wei84]   E. J. Weinberg, Monopoles and Grand Unification. In J. L. Stone (Editor) Monopole '83, vol. 111 of *NATO ASI Series*, 1–16, Springer US (1984), doi: 10.1007/978-1-4757-0375-7_1 (cit. on p. 14)

[Wey29]   H. Weyl, Elektron und Gravitation. I. *Z. Physik*, 56:330–352 (1929), doi:10. 1007/BF01339504 (cit. on p. 12)

[Wic03]   S. D. Wick, T. W. Kephart, T. J. Weiler, and P. L. Biermann, Signatures for a cosmic flux of magnetic monopoles. *Astropart. Phys.*, 18(6):663–687 (2003) (cit. on pp. 16, 17, 32, 33, 34, 37, and XI)

[Wie98]   C. H. Wiebusch, GEN 3.0 Generators for events in Neutrino telescopes (1998), as cited in [Wis09] (cit. on p. 49)

[Wis09]   H. Wissing, Search for relativistic magnetic monopoles with the AMANDA-II detector. Ph.D. thesis, RWTH Aachen University (2009) (cit. on p. XLI)

[Wu76]   T. T. Wu and C. N. Yang, Dirac monopole without strings: monopole harmonics. *Nucl. Phys. B*, 107(3):365–380 (1976), doi:10.1016/0550-3213(76)90143-7 (cit. on p. 26)

[Yan05]   H.-J. Yang, B. P. Roe, and J. Zhu, Studies of boosted decision trees for Mini-BooNE particle identification. *Nucl. Instrum. Meth. in Phys. Res. A*, 555(1-2):370–385 (2005) (cit. on p. XVII)

List of Figures

List of Tables

Index

A

$\vec{A}$ (magnetic vector potential), 11, 26

A (area), 75

A (atomic weight), 30

$a_{i,j}$ (normalization constant), 43

Acceleration, 15

after-pulse, 9, 59

air shower, 3, 61

    electromagnetic component, 3

    hadronic component, 3

    muonic component, 3

α (confidence level), 75

α (fine structure constant), 11

α (see phase), 12

α-particle, 29

α_M (magnetic coupling constant), 13, 29

amplitude, 12

angular distribution, 52

ANITA, 18

ankle of the cosmic ray energy spectrum, 44

Antarctic ice, 7

ANTARES, 18, 21

astrophysical neutrino, 45

avogadro constant, 30

azimuth, 5, 60, XXII

B

$\vec{B}$ (magnetic field), 11

Baikal, 18

Bartol, 45

BDT (boosted decision tree), 62

β (see phase), 12

β (the speed in terms of c), 25

Bethe's sum rule, 29

blind, II

blind analysis, 10

Bloch correction, 32

boosted decision tree, 62, XVI

boosting, XVII

bootstrapping, 62, XVIII

Born approximation, 29, 31

bremsstrahlung, 3

burn sample, 10, 52

C

c (speed of light in vacuum), 11

c_p (phase velocity of light), 34

cascade, 3, 56

catalysis of nucleon decay, 21

characteristic velocity, 50

charge, 9

    density, 16

    Dirac, 13

    electric, 11

    GUT, 13

    magnetic, 11, 13

charged current interaction, 4

Cherenkov

    angle, 35

    cone, 35

    light, 34, 51

      direct, 21

      direct, electrically, 34

      indirect, 21

    threshold, 1, 19, 34, 49

close collision, 29

CLSim, 46

cluster trigger, 53

CMC, 45

coherence length, 16

collision

    close, 29

    distant, 29

collisional losses, 50

confidence

    interval, 75

    level, 75

conventional neutrinos, 45

coordinate system, 5

corridor events, 71

CORSIKA (COsmic Ray Simulations for KASKADE), 43

cosmic rays, 3

Coulomb

    potential, 23

    scattering, 22

coverage, 75

CPU (Central Processing Unit), 46